FULLY AUTONOMOUS PIEZOELECTRIC ENERGY HARVESTING INTERFACE CIRCUIT UTILIZING LOW PROFILE NONLINEAR SWITCHING TECHNIQUE

A THESIS SUBMITTED TO
THE GRADUATE SCHOOL OF NATURAL AND APPLIED SCIENCES
OF
MIDDLE EAST TECHNICAL UNIVERSITY

BY

BERKAY ÇİFTCİ

IN PARTIAL FULFILLMENT OF THE REQUIREMENTS
FOR
THE DEGREE OF MASTER OF SCIENCE
IN
ELECTRICAL AND ELECTRONICS ENGINEERING

JUNE 2020

Approval of the thesis:

FULLY AUTONOMOUS PIEZOELECTRIC ENERGY HARVESTING INTERFACE CIRCUIT UTILIZING LOW PROFILE NONLINEAR SWITCHING TECHNIQUE

submitted by **BERKAY ÇİFTCİ** in partial fulfillment of the requirements for the degree of **Master of Science in Electrical and Electronics Engineering Department, Middle East Technical University** by,

Prof. Dr. Halil Kalıpçılar
Dean, Graduate School of **Natural and Applied Sciences** _____

Prof. Dr. İlkay Ulusoy
Head of Department, **Electrical and Electronics Eng.** _____

Prof. Dr. Haluk Külah
Supervisor, **Electrical and Electronics Eng., METU** _____

Examining Committee Members:

Prof. Dr. Tayfun Akın
Electrical and Electronics Eng., METU _____

Prof. Dr. Haluk Külah
Electrical and Electronics Eng., METU _____

Prof. Dr. Nevzat Güneri Gençer
Electrical and Electronics Eng., METU _____

Assoc. Prof. Dr. Serdar Kocaman
Electrical and Electronics Eng., METU _____

Assist. Prof. Dr. Dinçer Gökcen
Electrical and Electronics Eng., Hacettepe University _____

Date: 18.06.2020

I hereby declare that all information in this document has been obtained and presented in accordance with academic rules and ethical conduct. I also declare that, as required by these rules and conduct, I have fully cited and referenced all material and results that are not original to this work.

Name, Surname: Berkay Çiftci

Signature:

ABSTRACT

FULLY AUTONOMOUS PIEZOELECTRIC ENERGY HARVESTING INTERFACE CIRCUIT UTILIZING LOW PROFILE NONLINEAR SWITCHING TECHNIQUE

Çiftci, Berkay
Master of Science, Electrical and Electronics Engineering
Supervisor: Prof. Dr. Haluk Külah

June 2020, 88 pages

Energy scavenging from ambient vibration sources via piezoelectric transducers offers a promising solution to power microelectronic devices. Energy extraction from harvesters is conducted with full-bridge rectifiers (FBRs) whose performances are affected harshly due to intrinsic capacitance of harvester requiring continuous charging. Conventional nonlinear switching techniques proposed in literature overcome problems associated with standard AC/DC converters. Nonetheless, they require large external components to achieve decent conversion efficiencies and output powers. This obstructs miniaturization trend in micro-fabricated wireless sensor networks and limits their application area. The aim of this work is to implement a low-profile autonomous interface circuit that can harvest energy from MEMS piezoelectric transducers and deliver power to electronic loads.

In the first design, a unique low-cost fully autonomous interface circuit using novel SSHCI technique is proposed to reduce overall system volume. New two-step voltage flipping with optimal flipping time detection enables Synchronized Switch Harvesting on Capacitor-Inductor (SSHCI) circuit to use inductors in the range of tens of μH's for voltage flipping. This shrinks system volume significantly. Fabricated IC is able to attain 6.14x output power improvement over ideal FBRs and 90.1% power

conversion efficiency. Secondly, maximum power point tracking (MPPT) circuit integrated with SSHCI is implemented to eliminate load dependency. Inductor sharing between SSHCI and MPPT allows them to employ the same low-prolife inductor for operation which decreases system cost. Occasional refreshment of optimum battery voltage sensing makes system invulnerable to input excitation changes of PEH. SSHCI-MPPT achieves 5.44x power extraction improvement and 83% efficiency while providing load independency.

Keywords: Piezoelectric Energy Harvesters, Interface Circuit, Low-profile, Self-powered IC, MPPT.

ÖZ

DÜŞÜK PROFİLLİ DOĞRUSAL OLMAYAN ANAHTARLAMA TEKNİĞİ KULLANAN TAM OTONOM PİEZOELEKTRİK ENERJİ ÜRETECİ ARAYÜZ DEVRESİ

Çiftci, Berkay
Yüksek Lisans, Elektrik ve Elektronik Mühendisliği
Tez Danışmanı: Prof. Dr. Haluk Külah

Haziran 2020, 88 sayfa

Piezoelektrik enerji üreteçleri kullanılarak ortam titreşimlerinden enerji üretmek, mikro-elektronik cihazların kendi kendilerine çalışmalarını sağlamak için umut verici bir çözüm sunar. Enerji üreteçlerinden güç elde etme işlemi genellikle sürekli şarj gerektiren piezoelektrik kapasitansa bağlı olarak performansları kötü bir şekilde etkilenen tam-köprü doğrultucularla gerçekleştirilir. Literatürdeki doğrusal olmayan anahtarlama teknikleri, standart AC/DC dönüştürücülerde karşılaşılan problemlerin üstesinden gelir. Bununla birlikte bu devreler, iyi bir güç dönüşüm verimliliği ve çıkış gücü elde etmek için büyük harici bileşenlere ihtiyaç duyarlar. Bu, mikro fabrikasyon üretimi olan kablosuz sensör ağlarındaki minyatürleştirme eğilimini engeller ve uygulama alanlarını sınırlar. Bu çalışmanın amacı, MEMS piezoelektrik dönüştürücülerden enerji toplayabilen ve elektronik yüklere güç sağlayabilen düşük profilli otonom bir arayüz devresi tasarlamak ve uygulamaktır.

İlk tasarımda, sistem hacmini azaltmak için yeni SSHCI tekniğini kullanan bir düşük hacimli tamamen otonom arayüz devresi önerildi. Optimal dönüşüm süresini algılayabilen yeni iki-aşamalı voltaj dönüştürme işlemi, SSHCI devresinde voltaj dönüştürme amacıyla kullanılan bobinin boyutunun μH aralığına düşürülmesini sağlar. Bu yöntem, sistem hacmini önemli ölçüde azaltır. Üretilen devre (IC), ideal

tam-köprü doğrultuculara göre 6.14x çıkış gücü iyileştirmesi sağlar ve %90.1 güç dönüşüm verimliliği elde edebilir. İkinci tasarımda, çıkış gücünün yüke bağımlılığını ortadan kaldırmak için SSHCI ile çalışabilen bir MPPT devresi tasarlanmıştır. SSHCI ve MPPT arasındaki bobin paylaşımı, çalışmaları için aynı düşük profilli bobini kullanmalarına izin verir ve sistemin daha az yer kaplamasını sağlar. Optimum pil voltajının otomatik algılamasının ara sıra yenilenmesi, sistemi enerji üretecinin giriş uyarma değişikliklerine karşı dayanıklı hale getirir. SSHCI-MPPT, yükten bağımsız bir yapı sunarken 5.44x çıkış gücü iyileştirmesi ve %83 güç dönüşüm verimliliğine ulaşır.

Anahtar Kelimeler: Piezoelektrik Enerji Üreteçleri, Arayüz Elektroniği, Düşük Profilli, Kendi Kendine Çalışan IC, MPPT.

To my grandmother

ACKNOWLEDGEMENTS

Firstly, I would like to express my deepest gratitude to my advisor Prof. Dr. Haluk Külah for his continuous support, guidance, and for giving this once in a lifetime opportunity to be a part of an amazing project where we can touch lives of many people. I would also like to thank Prof. Dr. Ali Muhtaroğlu for his unique and constructive comments during IC design phase which boosted reliability of my designs.

I want to thank Dr. Salar Chamanian for his invaluable help and supervision. He has been both a mentor and a close friend who accompanied me with his instructive feedbacks.

I am exceptionally thankful to my friend Berat Yüksel who has never hesitated to aid me whenever possible during my undergraduate and graduate studies. It has been an honor to be a part of BioMEMS research group which consists of remarkable individuals that I see as my family. I want to articulate my deepest gratitude to my excellent colleagues Andaç Yiğit, Hasan Uluşan, Aziz Koyuncuoğlu, Akın Mert Yılmaz, Mert Koç, Yasemin Engür, Alper Kaan Soydan, and Mert Doğan.

I would like to express my sincere gratitude to my parents Tülay and Ahmet Çiftci who always made me feel their unconditional love and support. I am very grateful to my grandmother Zeynep Gürer for raising me as her own son and making me who I am today. I feel very lucky to have them in my life.

The author has been financially supported by TUBITAK BIDEB 2210-A 2017/2 graduate scholarship programme.

TABLE OF CONTENTS

LIST OF TABLES

TABLES

LIST OF FIGURES

FIGURES

CHAPTER 1

INTRODUCTION

1.1. Motivation

Downsizing trend in electronic systems has made portable electronics such as wireless and implantable sensors connected to a common network become popular in everyday life applications. Moreover, power demands of some currently designed wireless sensor networks (WSNs) have been decreased down to μW power range [1]–[7]. Nevertheless, they still need batteries employed as power supplies for proper sensor operation. Power consumptions of WSNs presented in [1]–[7] are depicted in Figure 1.1. Although storage densities of batteries have been elevated with technology, they require recharging once in a while [8]. Reduction ratio of battery volumes is less than that of sensor electronics over the years [9]. Therefore, batteries are accounted for most of the space that today's WSNs occupy and they obstruct attaining low profile systems. Besides, battery replacement and its sustainability might be costly and physically infeasible in some applications [10]. Scavenging energy from environmental sources offers plausible and cost effective solution to power up WSNs while reducing overall system volume.

Various ambient sources such as ambient light, vibration (or motion), thermal energy, and RF sources can be employed for energy harvesting purposes depending on their availability. Application areas for harvesters converting ambient energy range from medical devices (such as health monitoring sensors [11] and fully implantable cochlear implants [12]) to RFID sensors, and smart buildings [9]. Researchers have been looking for ways to apply concept of energy harvesting especially on biomedical WSNs to make them truly wireless.

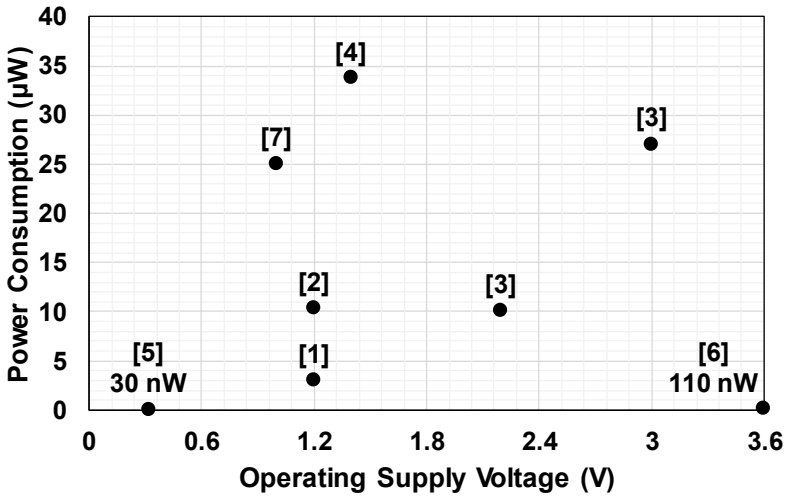

Figure 1.1. Power consumptions and operating supply voltages of WSNs presented in [1]-[7].

Today's cochlear implants (CIs) are powered by bulky external batteries which create a major barrier in front of miniaturization [13]. However, power requirements of neural stimulation circuits that are designed to stimulate auditory neurons in new generation fully implantable CIs have dropped below 600 µW [14], [15]. Considering output energy potentials of energy harvesting approaches [16], it is possible to provide some fraction of or the entire required energy for CI system operation through energy harvesting.

Design and implementation of energy harvesting architectures (or energy scavengers - transducers) has been a hot topic for the last decade [12], [17], [18]. These studies were focused on efficient mechanical structure design of energy harvesting transducers and their optimization in terms of output power. However, a dedicated interface circuit is required to extract most of the harvested energy, especially for a low output power harvester. This is because inherent impedances of energy harvesters must be matched to output loads so as to transfer maximum energy. It is possible only if a matching network or interface exists.

This thesis aims to design a low power, fully autonomous piezoelectric energy harvesting interface circuit that utilizes low profile nonlinear switching technique to shrink overall system volume. The interface circuit is able to rectify AC voltage

generated from piezoelectric energy harvesters and supply usable DC levels which might be used to power up WSNs. In this chapter, an introduction to energy harvesting sources (with focus on vibration based energy harvesting), electrical and mechanical modelling of piezoelectric energy harvesters with possible applications are provided.

1.2. Energy Harvesting Sources

There are four energy sources (vibration, light, RF, and heat) existing in the environment that intrigue researchers working on energy harvesting. Energy scavenging architectures utilizing theses sources will be summarized in this section.

1.2.1. Thermal Energy Harvesters

Thermal energy harvesters (i.e. thermoelectric generators) are able to generate energy from temperature difference occurring between their two dissimilar terminals which are thermal conductors. Seebeck effect is adopted to convert temperature gradient into electrical voltage [9]. Thermoelectric energy harvesters are especially useful when a large temperature difference is present in environment. A novel thermoelectric energy harvester that is able to retain 2°C temperature difference inside its physical construction has been proposed recently [18]. It can accomplish 10.23 J/g energy output density which can power up most of WSNs used for ambient monitoring [18]. In another application, thermal energy scavengers have been integrated on wristbands and headbands to see how much power can be generated with human body heat [19]. A power production density of 25 $\mu W/cm^2$ at 22°C was measured while an office worker puts this device on his/her wrist for several hours of ordinary work day [19].

According to [16], together with photovoltaic harvesters, energy harvesting from temperature gradient yields the highest power output as it is shown in Figure 1.2. However, generated output voltage levels are low compared to other harvesting methods and they require dedicated interface circuits to boost output voltage to levels which electronic circuits in WSNs can utilize [20]. In addition, it is quite difficult to attain a large temperature difference between terminals while adopting small thickness for the sake of miniaturization [21].

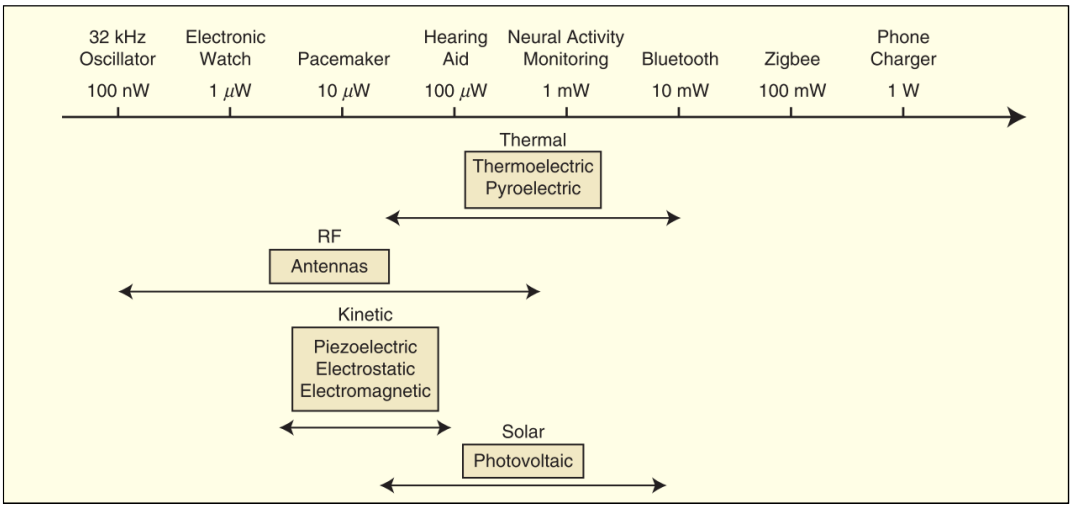

Figure 1.2. Power outputs of energy harvesting approaches and required power levels of some WSN applications according to [16].

1.2.2. Photovoltaic Energy Harvesters

Ambient light (indoor or outdoor) is converted to electrical energy through photovoltaic energy scavengers. Sun is an undeniable energy source with a potential to provide energy for various applications ranging from household electricity to powering up sensor in Body Area Network (BAN). Photovoltaic harvesters have power conversion efficiencies around 5-30% which are contingent upon materials used in device fabrication [9]. Performances of III-V solar cells are evaluated as indoor energy harvesters in [22] and it is observed that solar cells made up of GaAs and GaInP have two times larger output power densities compared to conventional amorphous-silicon cells [22]. In another indoor application, designed photovoltaic harvester is able to generate more than 90 μW with 415 lux light illumination at 25°C [23]. Even though energy harvesting from indoor light has been improved recently, energy harvesting from outdoor light is more appealing due to its higher output power potential as it can be seen from Figure 1.2.

Light sources are not always available in the environment and this might be accounted as a disadvantage of photovoltaic harvesters. Besides, they can be inconsistent throughout the day. This is a critical factor limiting the maximum harvested output

power and making output of solar cells unreliable due to fluctuation in generated power levels.

1.2.3. RF Energy Harvesters

Massive area availability of public telecommunication services such as Global System for Mobile Communications (GSM) and Wireless Local Area Network (WLAN) makes us to be exposed to radio frequency (RF) waves [21]. In fact, this offers an alternative energy harvesting methodology through RF waves. In [24], a RF harvesting system which can produce more than 200 μW output power when the source is 2 m away was reported. Integrated RF energy harvesting system which combines low power interface circuit fabricated with 130 nm CMOS and a differential PCB custom antenna was published in [25]. System achieves 60% peak power conversion efficiency in wide frequency band between 840 MHz to 975 MHz [25].

RF harvesters suffer from low power density levels due large distances existing between harvester and GSM base station [9]. Of course, it is possible to boost available energy density via RF harvesters having larger area (antenna area); however, it will increase overall space occupied by harvester and this limit application areas especially in low profile WSNs.

1.2.4. Energy Harvesting from Vibration

Harvesting energy from ambient vibrations have always been a popular topic since the beginning of energy scavenging phenomenon came out [16]. This is due to the fact that environmental vibrations are abundant in nature. Vibration (or motion) can be present in human body movements, acoustic noise vibrations, vehicle motion (from relocation of vehicle or motor vibration), and seismic vibrations that exist in moving structures like bridges. These sources have distinct vibration frequencies and amplitudes requiring various mechanical structures to convert kinetic energy into usable electrical energy. Three conversion mechanisms namely electrostatic, electromagnetic, and piezoelectric appear as energy harvesting methods from motion in the literature.

In capacitive conversion which is realized via electrostatic energy harvesters, harvesting process takes place when the distance (or gap) between two plates of polarized capacitor alters with ambient motion [9]. A voltage difference is created between capacitor terminals thanks to this motion and some current starts to flow through the external load [21]. A micro-electrostatic energy harvester fabricated with MEMS technology was presented in [26] along with its characterization and equivalent electrical modelling. This micro-generator was able to produce 3.5 μW with an input excitation of 13 g [26]. Frequency range of the MEMS harvester has been increased with design given in [27]. Dual resonant structure benefiting from crab supporting legs has successfully increased frequency range from 141.6 Hz to 191.1 Hz while producing output power up to 3.24 μW [27]. Despite being realized very easily with conventional fabrication techniques, electrostatic harvesters demand initial polarization with high voltage levels around 30 V. Moreover, they deliver low output current because of their high output impedance while providing large output voltages that make it challenging to design efficient interface circuits with standard CMOS process [21].

Electromagnetic energy harvesters benefit from Faraday's Law of Induction to generate AC voltage between its terminals with the relative movement of a magnet with respect to a coil. This relative motion of magnetic material creates a change in magnetic flux that transforms kinetic energy into electrical one. The micro power generator given in [28] is a good example of a vibration harvester employing electromagnetic (or inductive) conversion principle. Like other electromagnetic energy harvesters, this generator can deliver high output current to loads while acquiring low output voltages (<1 V) which complicate harvesting interface circuit design [21]. Maximum achievable output power greatly depends on properties of magnetic material and number of turns that coil has. Additionally, it is hard to fabricate electromagnetic harvesters using MEMS technology due to required bulky magnets which hamper miniaturization.

Ambient vibrations constitute strain on piezoelectric layers triggering charge separation among piezo material terminals. Direct piezoelectric effect converts strain into AC voltage that can be used to drive an external load [21]. Unlike inductive conversion mechanism, piezoelectric conversion relatively high output voltages with small current sourcing capability. There exist two crucial properties making piezoelectric energy harvesters the most preferred vibrational harvesting method. Firstly, they have high compatibility with standard MEMS fabrication process [16]. This pave the way for miniature harvesting systems with integrated on-chip harvesters. Secondly, among other kinetic harvesters, piezoelectric conversion offers the highest energy storage density according to [29]. However, some kind of interface is mandatory to extract this energy stored. Rest of this chapter will be about piezoelectric energy harvester structures, their electrical modelling, and some specific applications.

1.3. Piezoelectric Energy Harvesters

Lead zirconate titanate (PZT) is a frequently used piezoelectric substance in making vibrational energy harvesters. Swinging of piezoelectric energy harvester (PEH) originating from environmental vibrations establishes strain on PZT. This strain on PZT causes relocation of charges between top and bottom plates of PZT layer (direct piezoelectric effect) and an AC voltage is generated. Piezoelectric effect is depicted in Figure 1.3 with polarization direction of dipoles in PZT crystal [21], [30]. Naturally, for PZT crystals to perform piezoelectric effect under Curie temperature ($T<T_C$), they need to be polarized by application of a strong electric field.

Piezoelectric materials are generally quite stiff (inflexible). This leads to impractically high resonant frequencies when they are fixed directly to the frame and used as PEHs. Therefore, PZT is coated on cantilever beam to achieve straightforward energy harvesting mechanical structure as shown in Figure 1.4 [21]. In this figure, a mass is placed at the tip of the cantilever beam to reduce resonance frequency that enables IC designers to come up with efficient interface circuit architectures.

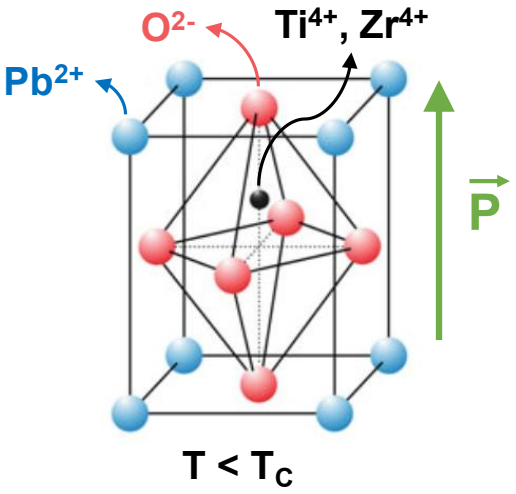

Figure 1.3. Piezoelectric effect in PZT crystal [21].

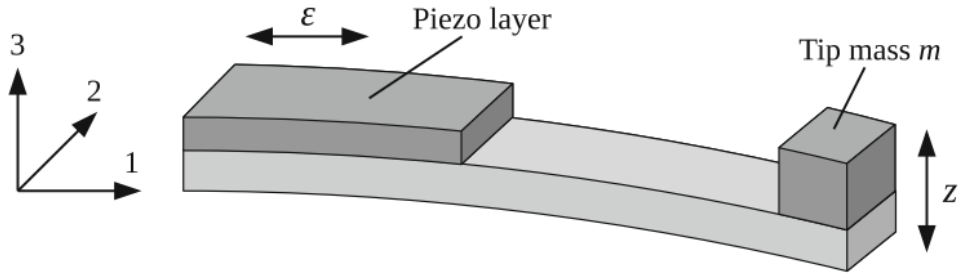

Figure 1.4. Conventional piezo material coated on flexible cantilever beam to be used as PEH [21].

Compressive and tensile stresses formed by movement of cantilever beam concentrate around the fixed end of the beam opposite side to the tip mass. Thus, piezo layer is adhered near the fixed end to convert most of these stresses into electrical energy.

According to [9] and [31], generated power of a vibrational harvester (including PEH) can be calculated as follows:

$$P_{OUT} = 4\pi^3 m f_{RES}^3 Y z_{MAX} \tag{1.1}$$

where m is the seismic mass, f_{RES} is the natural resonance frequency of the harvester, Y is the external vibration amplitude, and z_{MAX} is the maximum possible displacement of the cantilever beam. Nonetheless, equation (1.1) does not include a very important parameter which is coupling coefficient of the harvesting system [32]. This parameter

gives us valuable information about how much of mechanical energy can be converted into electrical energy. Details of this parameter will be illuminated in the following subsections. More specifically, for a piezoelectric energy harvester vibrating at its resonance frequency, maximum output power that can be extracted is calculated analytically as follows [32]:

$$P_{OUT} = \frac{k^2 m (QA)^2}{4w} \tag{1.2}$$

where k is system coupling coefficient, Q is the quality factor depending on damping ratio, A is acceleration magnitude, and w is angular excitation frequency. It is clear from equation (1.2) that coupling coefficient and quality factor (or damping) should be optimized to boost output power extracted from PEHs.

Minimization in WSNs forces researchers to come up with new mechanical harvesting structures compatible with micro fabrication process. The aim here is to generate maximum output power while achieving low profile harvesters. In [33] and [12], piezo ceramics with high coupling coefficient are used in MEMS fabrication process to obtain PEH. Schematic of MEMS based micro power generator placed on a vibrating membrane proposed in [12] is exhibited in Figure 1.5. This specific PEH is designed for scavenging energy from acoustic (sound) vibrations. Membrane mimics motion of eardrum. It was planned to be put on eardrum to provide required energy of new generation cochlear implants. Nevertheless, it should be noted that it is not an easy task to fabricate a MEMS device employing bulk PZT material as in Figure 1.5. Output power of PEHs strongly depends on fabrication quality and environmental excitation conditions. Wafer bonding process, quality of PZT material, PZT aging, and polarization of electrical charges in crystal structure necessitate special attention during MEMS fabrication. Table 1.1 gives an exhaustive performance comparison of recently fabricated low profile (small scale) PEHs [34]. It can be deducted that MEMS based PEH presented in [33] supplies maximum of 205 μW at 1.5 g excitation level while occupying 27 mm^3 active area. This power level is more than enough to maintain autonomous WSN operation in some applications [3], [7].

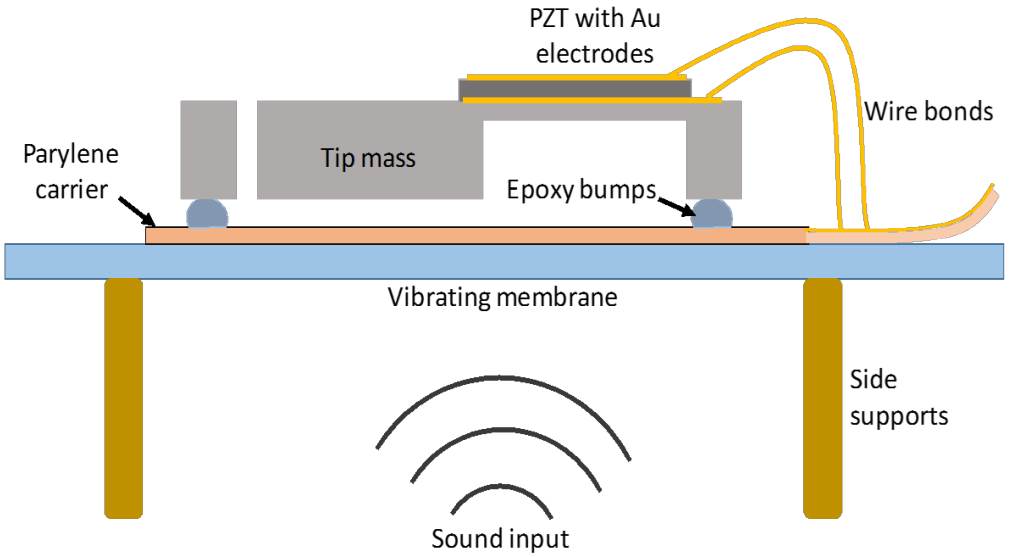

Figure 1.5. Schematic view of MEMS based PEH on vibrating membrane [12].

Table 1.1 also demonstrates that although [35] recorded less output power compared to [33], its normalized volumetric power density is larger. Moreover, if input acceleration of the harvester is increased, PEH in [35] it will generate more power among any other small-scaled piezoelectric energy harvester. For miniaturized harvesters, air resistance occurred during swing of piezoelectric beam is an important factor diminishing output power and vacuum-packaged structures offer a solution to that problem in general.

Table 1.1. *Performance comparison of recently fabricated PEHs [34].*

Ref.	Active Volume (mm^3)	Acceleration (g)	Frequency (Hz)	Power (μW)	Normalized Volumetric Power Density ($\mu W/(mm^3.Hz.g^2)$)
[35]	4.05	0.5	126	5.3	$4.15x10^{-2}$
[36]	0.02	4	1300	22	$5.29x10^{-2}$
[37]	464	0.2	76	13.9	$9.85x10^{-3}$
[38]	15	0.2	599	6.65	$1.85x10^{-2}$
[39]	18.6	1	235	14	$3.20x10^{-3}$
[33]	27	1.5	154	205	$2.19x10^{-2}$

1.3.1. Equivalent Electrical Model of Piezoelectric Energy Harvesters

Maximum energy transfer from PEHs to electronic loads is strongly contingent upon interface circuit design. One should properly model electrical characteristics of PEHs before starting design process. Here, an electrical equivalent circuit of PEHs will be developed for simulation purposes.

Figure 1.6 illustrates mechanical model of PEH along with an interface circuit and storage capacitor [40]. This is actually a second order spring-mass-damper system. The frame depicts whole PEHs while m is seismic mass, k_S is stiffness of the spring, d is the mechanical damping caused by friction, air resistance etc., and F_e is the restoring force that transducer applies on m if an interface circuit is connected to the harvester. It should be noted that there exists a phase difference between motions of the frame (y(t)) and seismic mass (z(t)). In addition, the work done by m against F_e is converted to into electrical energy [21]. Therefore, if restoring force F_e induced by interface circuit is large; more mechanical energy is converted into electrical one.

Before mechanical model of piezoelectric harvester is driven, following assumptions should be made: (a) vibration source mass is larger than seismic mass m, (b) excitation frequency of ambient vibration matches (or close) to the natural resonant frequency of PEH, and (c) fundamental resonant frequency is not disturbed other harmonic components [41]. Transfer function of the second order system (Figure 1.6) can be given as in equation (1.3).

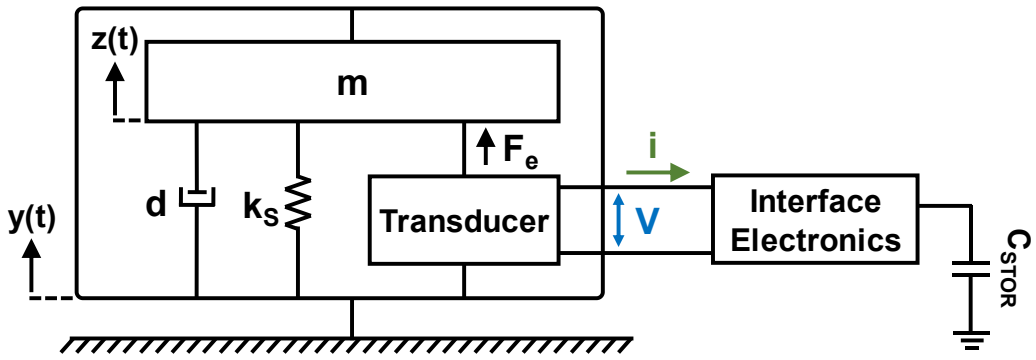

Figure 1.6. Mechanical model of PEH comprised of lumped elements. In the figure, interface electronics and storage capacitor are also included to show complete harvesting system.

$$m\ddot{y} = ma = m\ddot{z} + d\dot{z} + k_S z + F_e = m\ddot{z} + (d + d_e)\dot{z} + k_S z \tag{1.3}$$

where the restoring force can be represented as $F_e = d_e\dot{z}$ [21]. Since we need electrical model of PEH, we will represent equation (1.3) with electrical parameters. According to [40], mechanical force $F=ma$ can be described as electrical voltage whereas the first derivative of displacement $\dot{z}$ can be described as electrical current:

$$I \triangleq \dot{z} \quad \& \quad V \triangleq F \tag{1.4}$$

With the help of the correlation equation provided by equation (1.4), Figure 1.7 below depicts equivalent electrical circuit of equation (1.3). In this circuit, electrical output power that harvester generates represented by the power dissipated on resistor d_e where d_e represents electrical damping. For large output powers, d_e parameter that is contingent upon electrical interface should be large. Derivations up to here can be used for modelling of any kinetic energy harvester (electrostatic, piezoelectric, and electromagnetic). Constitutive piezoelectric equations for PEH given in Figure 1.4 operating in 31 mode (3 expresses that AC voltage is generated along z axis and 1 is the direction of applied stress) [21], [42] can be written as follows:

$$\begin{cases} F_e = k_P z + \Gamma V_{PZ} \\ I = \Gamma\dot{z} - C_{PZ}\dot{V}_{PZ} \end{cases} \tag{1.5}$$

where k_P is the piezoelectric stiffness, Γ is the electromechanical coupling coefficient, V_{PZ} is the generated AC voltage between piezoelectric terminals, I_{PZ} is the generated piezo current, and C_{PZ} is the inherent piezoelectric capacitance.

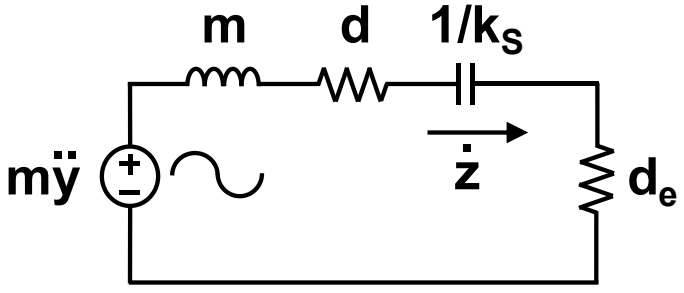

Figure 1.7. Equivalent circuit of kinetic energy harvester with electrical damping caused by connected interface circuit.

If we put F_e from equation (1.5) into (1.3), we will get:

$$\begin{cases} ma = m\ddot{z} + d\dot{z} + kz + \Gamma V_{PZ} \\ I = \Gamma\dot{z} - C_{PZ}\dot{V}_{PZ} \end{cases} \tag{1.6}$$

In these equations, k represents sum of mechanical and piezoelectric stiffness [21]. Considering equations in (1.6), a simple electrical model of PEH can be developed as depicted in Figure 1.8. This circuit was used while designing interface circuits for PEHs. Electromechanical coupling coefficient Γ and vibration velocity $\dot{z}$ govern how much mechanical vibration is converted into electrical energy. Dielectric losses on imperfect piezoelectric capacitance C_{PZ} are indicated with R_{PAR} but it is around 10 MΩ which does not affect circuit operation much.

1.3.2. Possible Applications

According to [16], PEH are able to generate power in the range of 1-100 μW. This is highly depend on physical volume of the harvester, excitation amplitude governing displacement of harvester, and resonant frequency. Furthermore, proper interface circuit can improve extracted power from mechanical vibrations. With output power level of piezoelectric energy harvesting system, most of WSNs can be operated.

We have started to encounter WSNs (system level representation of a WSN can be seen in Figure 1.9) everywhere in daily life. By definition, WSNs comprise of wireless communication units capable of monitoring (or sensing) different physical conditions (temperature, humidity, pressure, sound level, gas pollution level etc.) of the environment. Then, recorded data sets are sent to a central location. WSNs have variety of applications areas such as health monitoring, smart building (includes environmental monitoring), and active RFID tags [9].

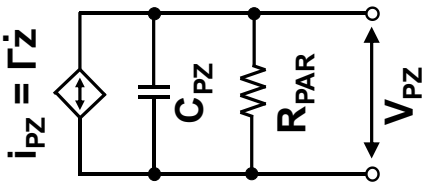

Figure 1.8. Simple equivalent electrical model of PEHs.

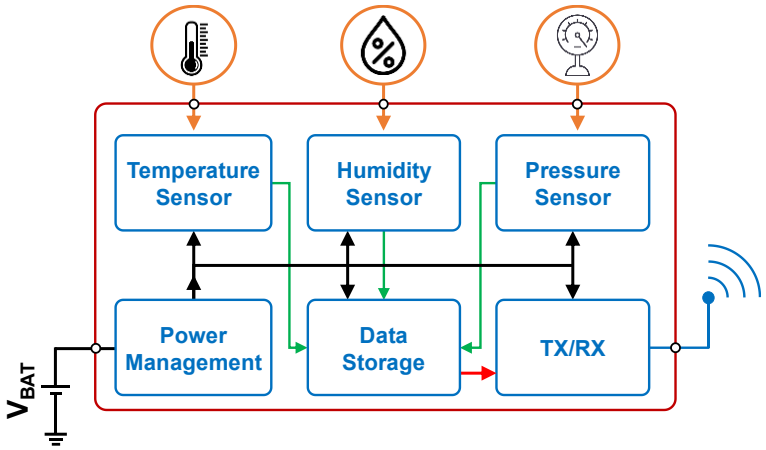

Figure 1.9. System level schematic of a WSN.

WSNs highly depend on bulky batteries to carry out their intended operations. As a result, these batteries occupy most of the space WSNs are accounted for. It is possible to use vibration based energy harvesters like PEHs as power supply sources instead of external batteries. By this way, both overall system volume and maintenance cost of WSNs will be shrunk.

Low-power and high efficiency PEH interface circuits make piezoelectric energy scavenging system an attractive solution for powering today's cochlear implants. Besides, new generation low power auditory stimulations circuits [15], [43] have relatively small power consumptions compared to conventional ones. Recently proposed MEMS based PEH in [12] is able to generate around 17 µW output power from 120 dB sound input. This is a promising result and it is believed that output power of this acoustic transducer can be augmented with new fabrications methods. Besides, interface circuits in [44], [45] which are devoted to improve energy extraction from PEHs will make it possible to fulfill power requirements of new generation cochlear implants in the near future.

1.4. Motivation and Organization of Thesis

The goal of this thesis is to design and implement low profile interface circuits to enhance energy extraction from piezoelectric energy harvesters for biomedical

applications and WSNs. Proposed interface circuits should possess the following properties:

1. Power Extraction Improvement: It is important for designed interface circuits to obtain as much power as it can while utilizing nonlinear switching techniques and surpass performance of standard converters. To compete with state-of-the-art interface circuits, proposed interface circuits should be able to extract at least 4 times output power of ideal full bridge rectifiers.
2. Low Profile: Most of today's power management circuits incorporate bulky external components to attain high power conversion efficiencies. Interface circuits proposed in this study should diminish volume of external components or try to eliminate them for the sake of minimization. It is desired to have external component sizes comparable to or smaller than that of fabricated IC package.
3. Autonomy: Designed circuits should be self-powered. In other words, they need to use harvested energy from PEH as their only input source and they should be able to begin charging output load with no initial charge (start-up operation should be present).
4. Low Power Consumption: Since energy output of PEH may be as low as few μW's, interface circuit should minimize its power dissipation by optimizing power consumptions of sub-blocks and switching losses. Power conversion efficiencies larger than 80% are targeted for self-powered operations.
5. Adaptability: Harvester outputs highly depend on ambient conditions which might alter. Proposed circuits should react to these changes in vibration frequency and amplitude and preserve its accurate operation.

Rest of the thesis covers four chapters. Chapter 2 is a literature review on piezoelectric energy harvesting interface circuits. Advantages and disadvantages of using each circuit are presented with a general performance comparison table at the end. A novel nonlinear switching technique called Synchronized Switch Harvesting on Capacitor-Inductor (SSHCI) is investigated in chapter 3. This chapter also covers evolution of

the new SSHCI method, design and specifications of sub-circuits, measured results of fabricated SSHCI chips, and performance comparison with state-of-the-art interface circuits.

Chapter 4 is about second-generation SSHCI circuit with integrated maximum power point tracking (MPPT) system. Theoretical calculation of optimal battery voltage for piezoelectric energy harvesting, modifications and improvements conducted on second-generation sub-blocks, and experimental results of MPPT-SSHCI chips fabricated with 180 nm standard CMOS process will be introduced in this chapter. Two different piezoelectric energy harvesters are utilized to evaluate performance of SSHCI-MPPT chips.

Finally, on chapter 5, accomplishments obtained throughout this thesis will be summarized and future works on piezoelectric energy harvesting interface circuit design will be discussed.

CHAPTER 2

INTERFACE ELECTRONICS OVERVIEW FOR PIEZOELECTRIC ENERGY HARVESTERS

2.1. Motivation

Kinetic energy harvesters benefit from environmental motions present nearly everywhere. This is why they have attracted more attention as alternative power supplies to maintain appropriate WSN operation in contrast to other harvesting sources which are relatively less common [16]. Like other motion based energy harvesters, PEH generates AC voltage from ambient vibrations. However, it is not possible to utilize this AC voltage directly to power up WSNs that require stable DC voltages. For AC-DC conversion purposes, different interface circuits has been proposed to both yield reliable DC voltages and enhance output power from PEHs by altering the charge on piezoelectric material [46]. Various energy extraction circuits have been proposed in the literature [47] to draw out maximum available energy from PEHs. Each technique has different target to conquer.

This chapter intends to present PEH interface circuit designs which take advantage of various nonlinear switching techniques existing in the literature. Section 2 is about standard AC-DC conversion circuits and reasons why they are not suitable for most of low power PEHs. Then, Synchronous Electric Charge Extraction (SECE) method that offers load independent energy extraction will be discussed in Section 3. Energy-investing synchronous energy extraction explained in Section 4 is an improved version of SECE where some amount of battery charge is invested on piezoelectric capacitance so as to generate more power from PEHs. Sections 5 and 6 describe Synchronized Switch Harvesting on Inductor (SSHI) and inductor-less design

techniques, respectively. Finally, Section 7 discusses weak and strong points of all extant energy extraction methods by making a general comparison between them.

2.2. Standard Interface Circuits

In the beginning of piezoelectric energy scavenging development, researchers focused on mechanical transducer design rather than its interface circuit. They tried to find adequate material to convert mechanical energy into electrical one and this material should also be compatible with standard fabrication processes. Therefore, simple rectifier circuits such as full bridge rectifiers and voltage doublers were used to achieve AC-DC conversion.

2.2.1. Full Bridge Rectifiers

Figure 2.1 below illustrates standard full bridge rectifier (FBR) consisting of four diodes and an output capacitor along with generated output voltage [48]. Energy transfer from piezoelectric capacitance C_{PZ} to storage capacitor C_S parallel with resistive load R starts when voltage difference between C_{PZ} reaches $V_{RECT} + 2V_D$ where V_D represents diode opening voltage. Performance of FBR was investigated in [48], [49] and for low coupled PEHs, it was observed that efficiency in terms of power extraction from PEH was poor. This is because piezoelectric capacitance C_{PZ} needs to be charged up to some voltage level, which is $V_{RECT} + 2V_D$, before charge relocation to C_S begins. It creates significant energy losses as given in Figure 2.1 with shaded regions. Moreover, voltage drops on the diodes should be eliminated for obtaining a reasonable power conversion efficiency. According to [46], [48], maximum power that could be observed at the output of a FBR is given by:

$$P_{OUT,FBR} = C_{PZ}(V_{OC,P} - 2V_D)^2 f_{EX} \tag{2.1}$$

where C_{PZ} is inherent piezoelectric capacitance, $V_{OC,P}$ is the amplitude (peak-to-zero) piezoelectric open circuit voltage, and f_{EX} is the excitation frequency of PEH. If we somehow manage to reduce diode opening voltage V_D, maximum achievable output power using FBR will go up.

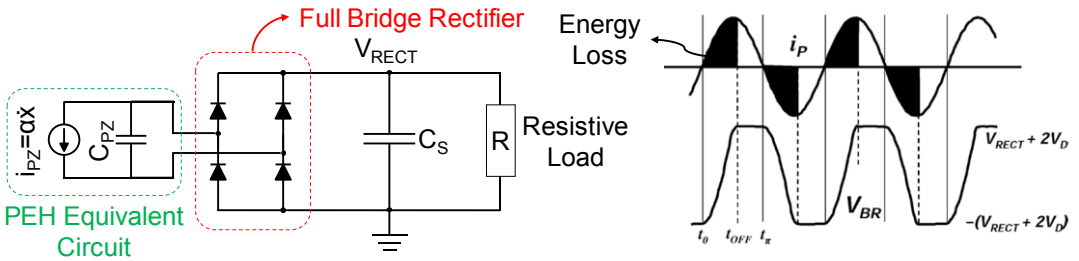

Figure 2.1. Standard full bridge rectifier which is the simplest AC-DC rectification circuit and generated output voltage [48].

2.2.2. Voltage Doublers

Unlike FBRs, voltage doubler circuit employs two diodes as shown in Figure 2.2 that reduces required voltage level to $V_{RECT} + 2V_D$ that piezoelectric open circuit voltage V_{PZ} should overcome [48], [50]. Maximum output power that can be extracted from PEH using a voltage doubler is expressed as [48]:

$$P_{OUT,VD} = C_{PZ}(V_{OC,P} - V_D)^2 f_{EX} \tag{2.2}$$

Still, voltage doubler suffers from the same problems standard FBR faces. Voltage drops on diodes limit minimum operation voltage of PEHs. Active diodes composed of a MOSFET switch and comparator can be used to get rid of voltage drops but residual voltage on C_{PZ} after charging makes it difficult to attain V_{RECT} voltage again in the negative cycle [51].

2.3. Synchronous Electric Charge Extraction (SECE)

Nonlinear switching methods in energy harvesting literature have been developed to match the internal impedance of PEHs to output load [47] and transfer all the available energy harvested from ambient environment. For that purpose, they are using external inductor to compensate the impact of large inherent piezoelectric capacitance C_{PZ}. SECE technique uses external inductor to store and deliver energy from C_{PZ} into storage capacitor. Figure 2.3 depicts conventional SECE converter circuit and waveforms of PEH terminals during SECE operation. Three switches S_1, S_2, and S_3 turn ON and OFF in a synchronous manner to carry out SECE.

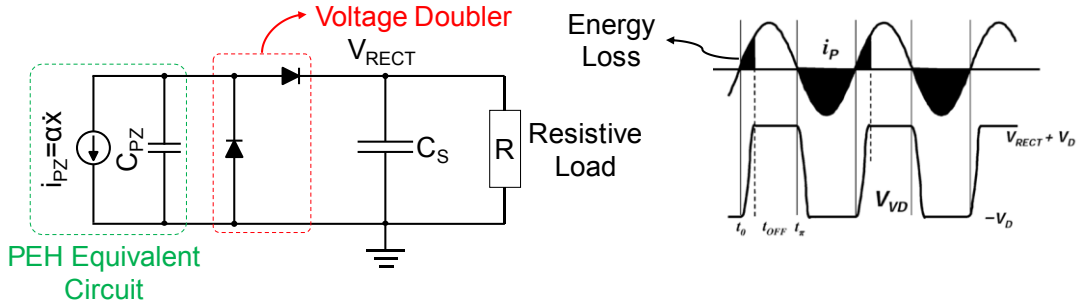

Figure 2.2. Voltage doubler circuit with generated output voltage waveforms when it is connected to PEHs [48].

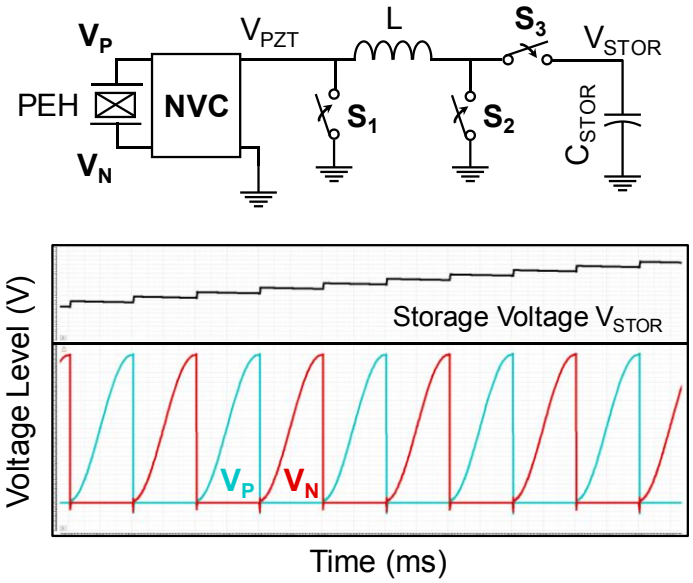

Figure 2.3. Schematic of conventional SECE circuit and observed waveforms during its operation.

Conventional SECE operation has three phases [52]. In the first phase, charge generation takes place on piezoelectric capacitance C_{PZ} with PEH movement. AC voltage occurs between terminals of PEH and this voltage is rectified through negative voltage converter (NVC). When deflection on piezoelectric beam reaches its maximum point, rectified piezoelectric voltage V_{PZT} attains its maximum level. At that point, SECE circuit goes into second phase by turning switch S_2 ON and energy accumulated on C_{PZ} transfers into the external inductor L. At the end of the second phase, S_2 turns OFF to avoid any reverse current from L to C_{PZ}. During phase 3,

energy transferred to L is now delivered to storage capacitor with helps of switches S_1 and S_3 which corresponds to the load charging phase. After phase 3, circuit returns back to phase 1 by turning all switches OFF. Similar to FBRs and voltage doublers, theoretically calculated maximum output power acquired using SECE technique is expressed as follows [53]:

$$P_{OUT,SECE} = C_{PZ} {V_{OC,PP}}^2 f_{EX} \tag{2.3}$$

where $V_{OC,PP}$ is peak-to-peak piezoelectric open circuit voltage and clearly, SECE outperforms standard rectification circuits (FBRs and voltage doublers) in terms of maximum attainable output power. SECE design has been implemented many times in the literature [52], [54]–[57]. The circuit proposed in [52] was one of the first complete SECE circuit which achieved 85% maximum power conversion efficiency while utilizing 10 mH external inductor with input power around 500 μW. [55] introduced a new and improved SECE method where energy is extracted from PEH in multiple energy packages. Although SECE provides load independent energy extraction via decoupling output load from PEH, output power improvement is inferior compared to other nonlinear switching techniques. It also employs a bulky external inductor that enlarges overall harvesting system volume.

2.4. Energy Investment

In [58], a modified SECE method called pre-biasing SECE was presented for the first time. This method which had exact same operation phases as described in SECE method increased output power of conventional SECE by investing some charge from battery to piezoelectric capacitance C_{PZ} at the beginning of each half cycle. Nonetheless, it needs multiple off-chip inductors and operates with high biasing voltages. Single-inductor energy investment circuits have been developed by different research groups [45], [59]. Figure 2.4 illustrates self-investing fully autonomous interface circuit proposed by our group in [45]. This circuit has almost identical operation phases (phases 1, 2, and 3 are the same) as conventional SECE circuit mentioned in the previous section.

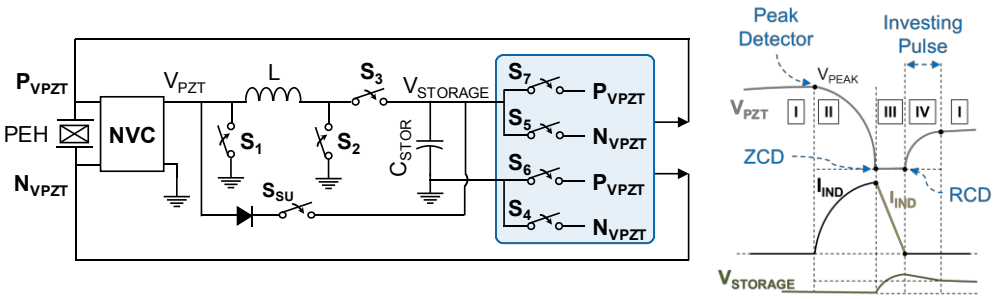

Figure 2.4. Self-investing SECE piezoelectric energy harvesting interface circuit proposed by us with four operation phases and conceptual waveforms.

Dissimilarity comes from the fourth phase shown in Figure 2.4. Operation phases of self-investing SECE circuit can be clarified as follows: With ambient vibrations, electrical charge starts to accumulate on piezoelectric capacitance C_{PZ} and rectified piezoelectric voltage V_{PZT} goes up (phase I). When V_{PZT} peaks, switch S_2 turns ON and energy is transferred from piezoelectric capacitance C_{PZ} to eternal inductor L_{EXT} (phase II). The moment that there exists no charge on C_{PZ} corresponds the time V_{PZT} reaches zero volt. Then, S_2 turns OFF while S_1 and S_3 turn ON to deliver energy to storage capacitance C_{STOR} (phase III). After energy transfer to C_{STOR} (battery charging phase), some amount of energy from battery is invested back to piezoelectric capacitance C_{PZ} to increase electrical damping caused by the interface circuit (phase IV). During investment, switches S_4 & S_7 or S_5 & S_6 are activated depending on polarity of the voltage on C_{PZ}. Since it is a self-powered structure, storage voltage V_{STOR} drops a little during investment. Circuit and system details of self-investing SECE technique are given in [45]. When piezoelectric beam arrives its peak displacement, all accumulated charge on C_{PZ} is transferred to L_{EXT} and then carried to C_{STOR} as explained above. Assuming that there is no loss occurred during synchronous switching, extracted energy from PEH at half period T/2 is [60]:

$$E_{SECE,T/2} = \frac{1}{2} C_{PZ} V_{OC,PP}^2 \tag{2.4}$$

where $E_{SECE,T/2}$ represents maximum energy obtained using SECE technique for half period of PEH excitation. In self-investing SECE, some amount of charge is transferred back to C_{PZ} from C_{STOR} to increase extracted energy by making use of

quadratic relation of piezoelectric open circuit voltage to the calculated energy. Let's assume that voltage V_{INV} is added up on C_{PZ} before PEH beam starts its swing. This time, voltage on C_{PZ} reaches a new peak voltage of $V_{NEW} = V_{OC,PP} + V_{INV}$ after its swing and maximum extractable energy is:

$$E_{NEW} = \frac{1}{2} C_{PZ} V_{NEW}^2 = \frac{1}{2} C_{PZ} (V_{OC,PP} + V_{INV})^2 \quad (2.5)$$

$$E_{NEW} = \frac{1}{2} C_{PZ} V_{OC,PP}^2 + \frac{1}{2} C_{PZ} V_{INV}^2 + C_{PZ} V_{OC,PP} V_{INV} \quad (2.6)$$

where $1/2 C_{PZ} V_{OC;PP}^2 = E_{SECE,T/2}$ is maximum energy obtained using SECE technique for half period of PEH excitation, $1/2 C_{PZ} V_{INV}^2 = E_{INV}$ is invested energy form C_{STOR}, and $C_{PZ} V_{OC;PP} V_{INV} = E_{GAIN}$ is extra energy gained thanks to quadratic relation of piezoelectric open circuit voltage to extracted energy. Form equation (2.6), it is seen that self-investing SECE attains more energy compared to conventional SECE circuits. Unlike standard SECE, an unlimited large current is passing from C_{STOR} to C_{PZ} during investment. This leads to increased power dissipation and eventually low power conversion efficiency.

2.5. Synchronized Switch Harvesting on Inductor (SSHI)

SSHI technique is by far the most investigated scheme due to its superior output power level [33], [48], [61]–[65]. Figure 2.5 depicts SSHI circuit and corresponding waveforms generated during operation. Like SECE and energy investment methods, SSHI employs an external inductor. However, this time, it is used to flip residual voltage left on piezoelectric capacitance C_{PZ} after battery charging is finished. This helps piezoelectric open circuit voltage to reach V_{STOR} voltage level in relatively short time and enlarges charging duration. According to [66], maximum extractable output power using SSHI technique is calculated as:

$$P_{OUT,SSHI} = 4 f_{EX} C_{PZ} V_{STOR} (V_{OC,P} + V_{STOR}[\eta_F - 1]) \quad (2.7)$$

where $V_{OC,P}$ is peak-to-zero piezoelectric open circuit voltage, and n_F is voltage flipping efficiency which is determined by L_{EXT} and constant for different $V_{OC,P}$ values

($0.6< n_F <1$). Derivation details of equation (2.7) will be given in chapter 4. Conventional SSHI method has three operation phases. As PEH swings with ambient vibrations, charge accumulation occurs on C_{PZ} (phase 1). This generated AC voltage is rectified via NVC or FBR and if rectified piezoelectric voltage V_{RECT} exceeds storage voltage V_{STOR}, transistor M_P turns ON and systems goes into phase 2. Here, load circuit (which is battery) is being charged. When $V_{STOR} < V_{RECT}$ as PEH curves into the negative half cycle, M_P is turned OFF by comparator. To reverse charge polarity on C_{PZ} after charging, S_1 switches starts their operation and $C_{PZ} - L_{EXT}$ resonance circuit is constructed. Control circuit inside SSHI turns S_1's OFF at the time there is no charge left on L_{EXT} which corresponds to half cycle of $C_{PZ} - L_{EXT}$ resonance. Afterwards, circuit goes back into phase 1 where charge generation on C_{PZ} takes place, but this time, PEH changes its swinging direction (negative half cycle).

According to [61], SSHI provides highest power extraction improvement with respect to ideal FBR. In this paper, 3.3 mH inductor which occupies 15.2 cm^3 area was used to increase power conversion efficiency. An interesting SSHI circuit employing a split electrode MEMS harvester given in [63] lessens required input excitation level of PEH for appropriate SSHI operation with its start-up design. Figure 2.6 shows theoretical output power comparison of various PEH interface circuits with respect to different piezoelectric open circuit voltages [46]. Even though single-supply pre-biasing (similar to our energy investment method that we have mentioned) extracts more power compared to parallel SSHI, it requires a relatively complex control circuitry and two external inductors for operation.

It seems that SSHI circuit is the perfect candidate for energy extraction from PEHs. Yet, this is not the case. External inductor unavoidably present in SSHI restrain miniaturization in harvesting systems. What's more, control signals in most of SSHI circuits are adjusted externally. This hinders fully autonomous operation which is critical for preserving working conditions of some distantly located WSNs. Therefore, researchers concentrated on diminishing overall volume with a fully autonomous interface circuit.

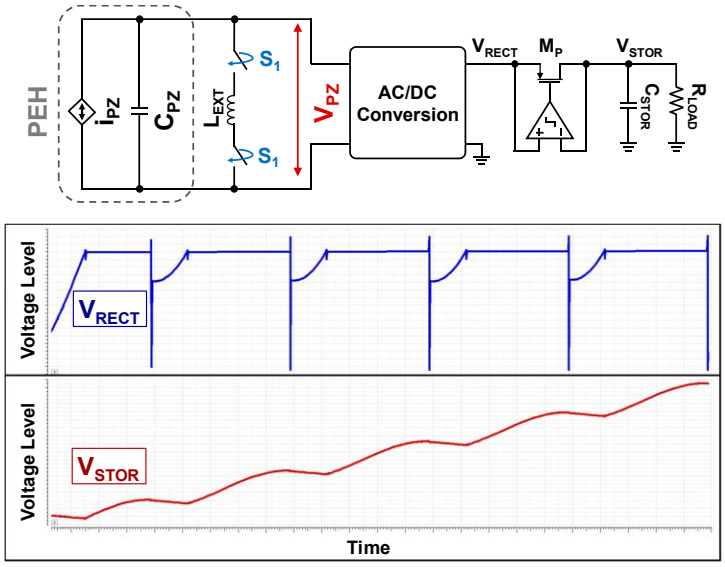

Figure 2.5. Schematic of conventional SSHI circuit with corresponding operation waveforms showing battery charging.

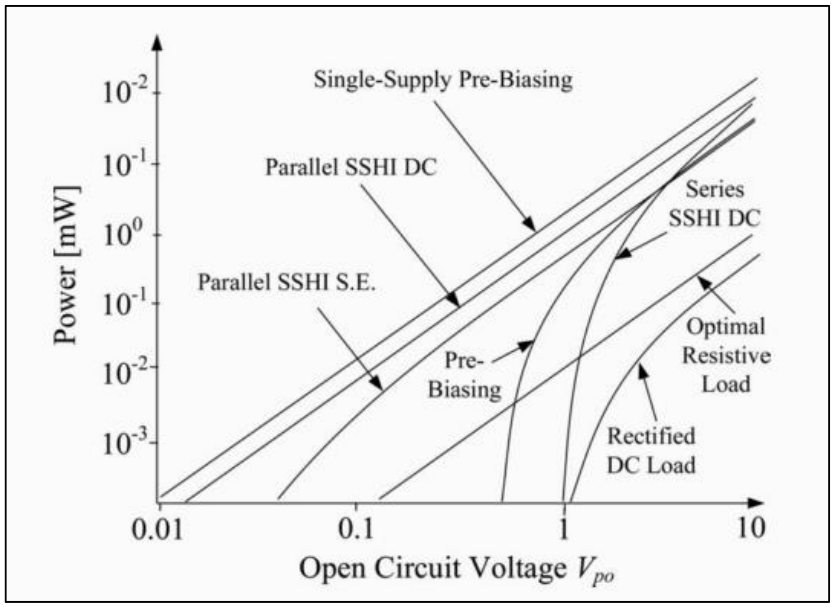

Figure 2.6. Theoretical output power comparison of various PEH interface circuits presented in [46].

2.6. Inductor-Less Designs

In search of eliminating external inductor, researchers came up with idea that switched capacitor (SC) circuits can be used instead of inductors to flip residual voltage on SSHI method [67]. This method has become popular for last three years [68], [69],

[66], [70], [71]. Figure 2.7 depicts inductorless design presented in [67] that achieves voltage flipping described in SSHI by making use of SCs. Cross-coupled 17 switches, which are controlled with synchronously generated 17 pulses, imitate operation of an inductor. This circuit has identical operation phases as SSHI circuit and maximum extractable output power using inductorless technique is the same as equation (2.7).

Electrical charge left on piezoelectric capacitance C_P after energy transfer to the electrical load is flipped by sharing charge with 8 capacitors and obtaining shared charge back to C_P with reserve polarity. Unfortunately in [67], control signals were adjusted externally for different PEHs and AC-DC conversion was attained with FBR limiting output power enhancement. Even though flipping capacitor rectifier (FCR) proposed in [70] has no external component for flipping, it is excited with 110 kHz frequency and it works with small C_P (80 pF) harvesters to realize reasonable flipping efficiencies. Furthermore, inductorless designs offer small power conversion efficiencies because they require quite large number of switching where currents passing through MOSFET switches are not limited.

2.7. Discussion

It is clear that different interface circuits have different advantages and disadvantages over each other. Since we are interested in commonly used low coupled piezoelectric energy harvesters in which only small portion of vibration is converted in to electrical energy, we cannot use any standard rectification circuit.

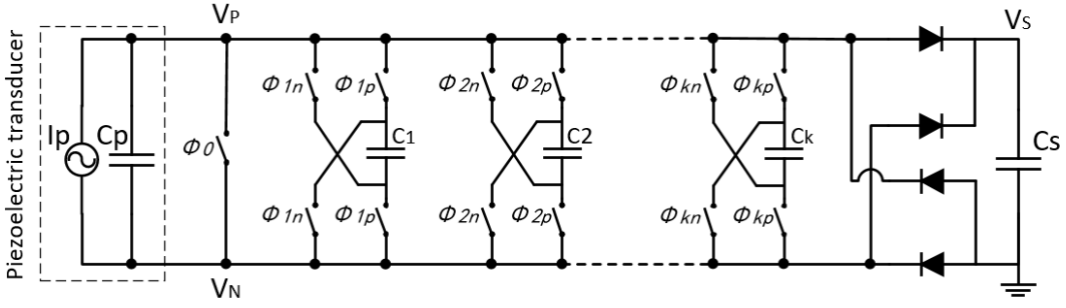

Figure 2.7. Inductorless Synchronized Switch Harvesting on Capacitor (SSHC) circuit proposed in [67] where FBR is used for AC/DC conversion.

Table 2.1. *Performance comparison of state-of-the-art PEH interface circuits.*

Ref.	*Tech.*	*Scheme*	*Freq.*	*Component (Volume)*	*Power Conv. Eff. (%)*	*FOM*[1]	*Chip Size*
[54] 2016	320 nm	SECE	60 Hz	10 mH (NA)	85.3[2]%	351%	0.95 mm^2
[52] 2012	350 nm	SECE	175.6 Hz	10 mH (0.63 cm^3)	85%	210%	1.25 mm^2
[55] 2019	180 nm	MSEE	390 Hz	1 mH (67 mm^3)	84.4%	NA	2 mm^2
[59] 2014	350 nm	Energy Investment	143 Hz	330 µH (126 mm^3)	69.2%	360%	2.34 mm^2
[45] 2018	180 nm	Energy Investment	250 Hz	3.3 mH (NA)	62.4%	300[3]%	0.79 mm^2
[48] 2010	350 nm	SSHI	225 Hz	820-22 µH (NA)	87[4]%	420[5]%	4.25 mm^2
[72] 2016	350 nm	SSHI	225 Hz	3.3 mH (15.2 cm^3)	88[3]%	440%	0.72 mm^2
[65] 2019	130 nm	SSHI	180 Hz	3.3 mH (NA)	78[2]%	417%	1.07 mm^2
[67] 2017	350 nm	SSHC	92 Hz	8 x 45 nF (8 x 2 mm^3)	NA	625[3]%	2.9 mm^2
[71] 2017	180 nm	FCR	110 kHz	NO	NA	483%	1.7 mm^2

(1) FOM = 100 x $P_{OUT}/f_{EX}V_{OC}^2C_{PZ}$
(2) External supply was used.
(3) Calculated from paper.
(4) It is only for DC-DC converter.
(5) Calculated with respect to off-chip FBR.

In biomedical applications, miniaturization in systems plays a key role in interface circuit design. Nevertheless, we cannot ignore the fact that an energy harvesting interface circuit should be able to extract most of the available electrical energy converted from ambient vibration. Table 2.1 provides a complete performance comparison of state-of-the-art energy harvesting interface circuits. Frequencies represent resonance frequency of each harvester utilized in experimental tests of fabricated chips. These frequency values on the table depend on mechanical structure (dimensions, materials used, fabrication method etc.) of each harvester and they are different from one another.

It can be concluded from table that SSHI provides higher figure-of-merit (FOM) and power conversion efficiency than SECE and energy investment techniques. However, they still depend on bulk external inductor that raises system volume. Inductorless designs [67], [71] yield promising results, but switched capacitor architecture causes unlimited current passing on MOSFET switches. It lowers power conversion efficiency and makes it difficult to achieve acceptable power improvement over ideal FBR. One more issue which is not addressed in Table 2.1 is fully autonomous operation which can be dealt with low power analog integrated circuit design techniques. A new type of nonlinear switching method which can benefit from both SSHI and inductorless design strategies is needed.

CHAPTER 3

FULLY AUTONOMOUS SYNCHRONIZED SWITCH HARVESTING ON CAPACITOR-INDUCTOR (SSHCI) DESIGN AND IMPLEMENTATION

3.1. Motivation

Overview of piezoelectric energy harvesting interface circuits in previous chapter showed that a new generation interface circuit possessing both low profile design and high power extraction-conversion efficiencies is needed. Therefore, a new nonlinear energy extraction technique that is able to operate with an inductor in the range of μH's while demonstrating output power and efficiency performances comparable with those of SSHI circuits should be developed.

The aim of this chapter is to present a PEH interface circuit making use of the new low profile nonlinear switching technique called Synchronized Switch Harvesting on Capacitor-Inductor (SSHCI) that is proposed by us in [73]. This novel SSHCI circuit designed and implemented with 180 nm standard CMOS process is a direct solution to aforementioned problems of SSHI and inductorless designs. Fabricated SSHCI chips use inductors in the range of 27-68 μH and carry out proper working phases with maximum power conversion efficiency larger than 80% [73]. Section 3.2 shares design steps that have been taken to reach SSHCI method. Operation phases and generated waveforms are given in section 3.3 with details to describe SSHCI better. Section 3.4 present sub-circuit blocks which make SSHCI operation possible. Fabricated SSHCI chips were tested with MEMS based PEH and measured results are given in section 3.5. Detailed comparison shows that SSHCI performs just as good as SSHI circuit in [72] while volume of the external component is much larger [73]. Lastly, performance comparison of SSHCI performance with state-of-the-art circuits and SSHCI parts that need improvement are discussed in section 3.6.

3.2. Evolution Towards SSHCI Circuit

SSHCI circuits in [33], [48], [61], [65] require large inductors in the range of mH's to obtain acceptable power extraction efficiencies. Table 3.1 below gives dimensions and volumes of surface mount technology (SMD) inductors that are used intensely in SSHI and SECE techniques [48], [55], [65], [72], [74]. Considering Table 3.1 in mind, an 820 μH SMD inductor takes up around 2 times space of conventional QFN 48 package footprint that occupies a space of 36 mm^3. This tells us that external inductors are responsible for most of the volume which piezoelectric energy harvesting electronics occupy. Of course one can find these inductors within smaller SMD packages but, smaller the packages, larger the series resistances these inductors will have. Larger series resistance means larger power dissipation on inductors and small voltage flipping efficiencies due to voltage drop on series resistances. Therefore, PEH interfaces utilizing SSHI circuits use the largest inductance values with the smallest series resistance. As the first step of designing a low profile SSHI, LC resonance circuit between piezoelectric capacitance C_{PZ} and external inductor L_{EXT} was constructed to flip residual voltage on C_{PZ} after battery charging. This circuit is depicted in Figure 3.1(a) where S_1 switches allow current to pass from C_{PZ} to L_{EXT}. Initially, 3.3 mH inductor, included in majority of SSHI circuits in the literature, was employed and waveforms of voltage difference V_{PZ} between C_{PZ} terminals and current i_{FLIP} passing through L_{EXT} were obtained via simulation. During simulations C_{PZ} is selected as 10 nF and waveforms showed in Figure 3.1(b) were observed for L_{EXT} = 3.3 mH. It is clear that large inductor was able to flip most of the residual charge from 3 V to -2.87 V (n_F = 97.83%) with a maximum i_{FLIP} current of 5.1 mA.

Table 3.1. *Specifications of various inductors used in PEH interface circuits [48], [65], [72], [74].*

Inductance Value	Dimensions (SMD Tech.)	Volume	Series Resistance
820 μH	4.8 mm x 4.8 mm x 2.9 mm	67 mm^3	3.8 Ω
1 mH	4.8 mm x 4.8 mm x 2.9 mm	67 mm^3	5.1 Ω
3.3 mH	8 mm x 8 mm x 6.5 mm	416 mm^3	7.3 Ω

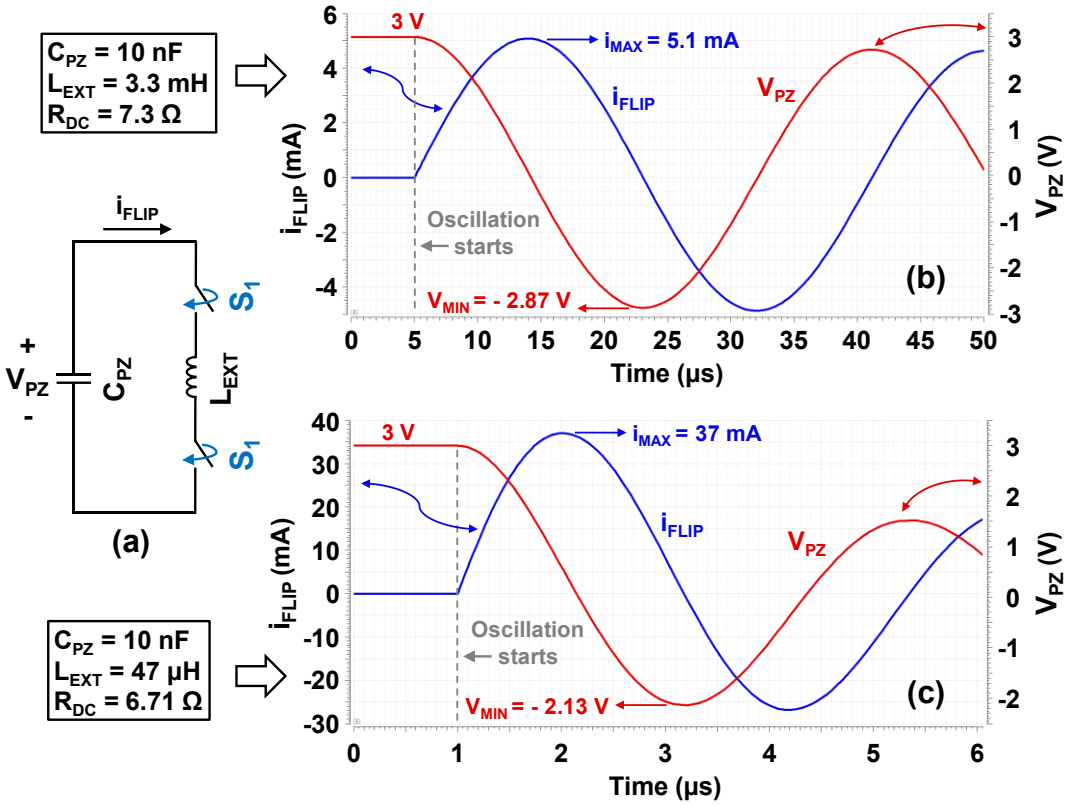

Figure 3.1. (a) LC resonance circuit constructed to flip residual voltage on PEH capacitance C_{PZ} after battery charging phase in SSHI circuit, simulated waveforms of voltage difference V_{PZ} between C_{PZ} terminals and current i_{FLIP} passing through external inductor L_{EXT} observed during voltage flipping phase for (b) L_{EXT} = 3.3 mH, and (c) L_{EXT} = 47 µH.

In the second simulation, L_{EXT} was reduced to 47 µH which occupies a space of 18 mm^3. This is 1/3.72 times smaller than that of 820 µH inductor and it is a huge step towards miniaturization. Figure 3.1(c) depicts simulation waveforms of V_{PZ} and i_{FLIP} for L_{EXT} = 47 µH. This time, 3 V residual voltage on C_{PZ} was flipped to -2.13 V which yielded less flipping efficiency n_F. One may think that using a smaller inductance did not lead to a harsh decrease in flipping efficiency. However, flipping current i_{FLIP} was risen to 37 mA that affects power consumption severely and diminishes power extraction improvement over ideal FBR. Solution to this problem can be addressed as presented in Figure 3.2 by adding an external capacitor C_{EXT} in series with small L_{EXT} in order to limit current i_{FLIP} passing through L_{EXT} and MOSFET switches S_1.

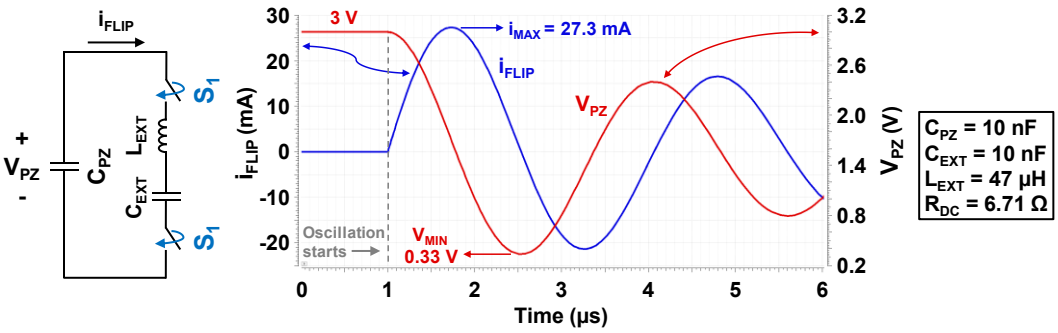

Figure 3.2. Modified LC resonance circuit constructed to flip residual voltage on C_{PZ}. A series external capacitance C_{EXT} is added to limit i_{FLIP} current.

C_{EXT} was selected to be equal to C_{PZ} so that maximum charge is transferred from C_{PZ} to C_{EXT}. From simulation waveforms illustrated in Figure 3.2, it was concluded that i_{FLIP} was reduced by 1 − (27.3 mA) / (37 mA) = 26.2% and this implies less power consumption on parasitic resistances of MOSFET switches and series resistance of L_{EXT}. Still, flipping efficiency was disturbed in this configuration because residual charge was transferred to C_{EXT} and circuit did not deliver this charge back to C_{PZ}. Therefore, cross-coupled switches were introduced into LC voltage flipping mechanism and final design called Synchronized Switch Harvesting on Capacitor-Inductor (SSHCI) was shaped. LC resonance circuit utilized by proposed SSHCI method is depicted in Figure 3.3. After all residual charge is transferred from C_{PZ} to C_{EXT}, switch S_0 turns on for a brief moment to discharge any charge that might exist on C_{PZ}. Then, charge on C_{EXT} is transferred back to C_{PZ} in reverse polarity with the help of S_2 switches to accomplish charge flipping process.

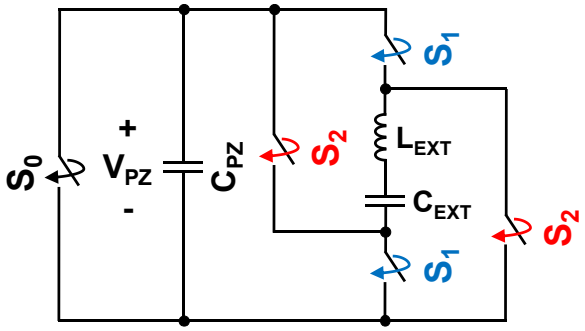

Figure 3.3. LC resonance circuit utilized by proposed SSHCI design to flip residual voltage on C_{PZ} after battery charging.

3.3. SSHCI Operation

Figure 3.4 below depicts our SSHCI circuit [73] which contains eight sub-units: Start-up trigger, negative voltage converter (NVC), reverse current detector (RCD), charge flipping detectors (CFDs), oscillation cancellation (OC), shorting pulse generator (SPG), sign detector (SD), and switch control block. The enable signal generated by the start-up unit indicates that there exists sufficient charge on C_{STOR} to maintain proper operation of the SSHCI circuit. The interface has five operational phases illustrated with the equivalent circuits established in Figure 3.5.

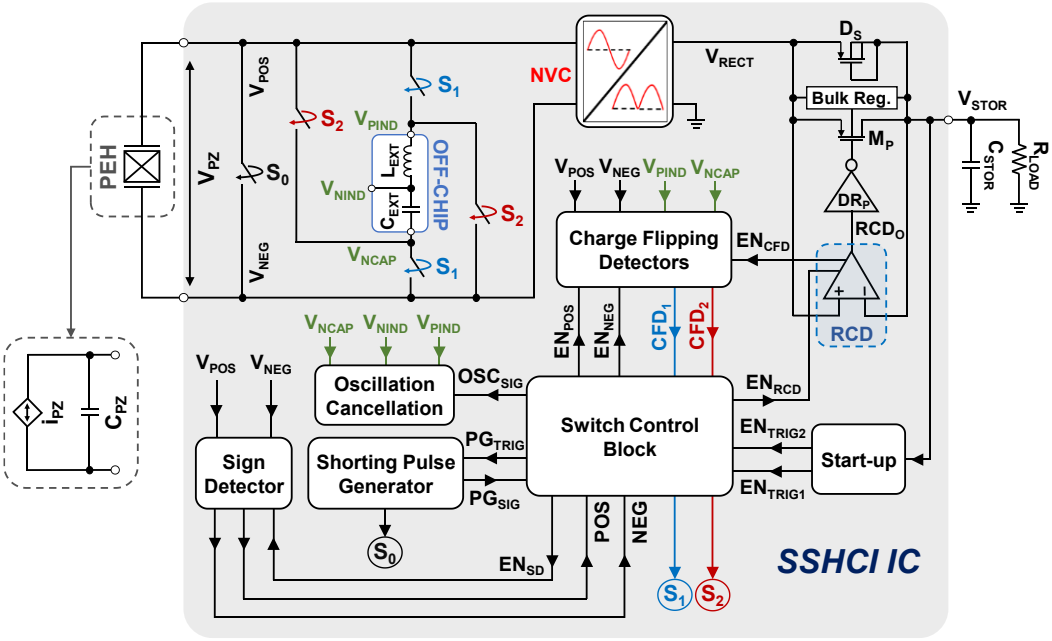

Figure 3.4. Synchronized Switch Harvesting on Capacitor-Inductor (SSHCI) interface circuit that utilizes a low profile inductor and an external capacitor to flip residual voltage on C_{PZ}.

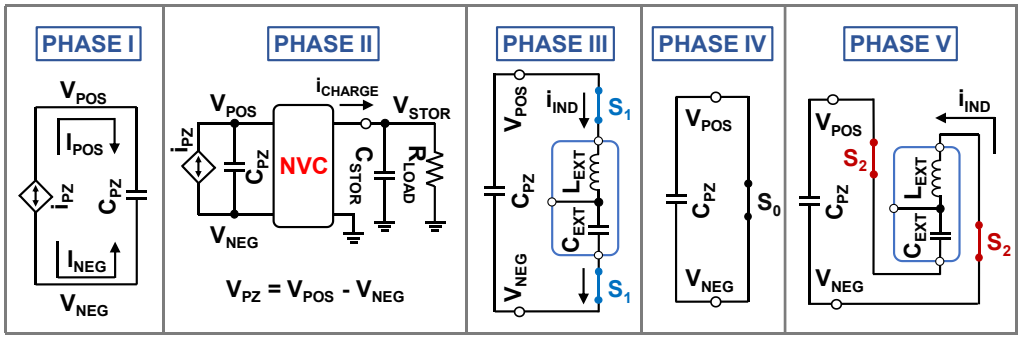

Figure 3.5. Summary of SSHCI operation phases.

As the piezoelectric beam swings with ambient vibration, some amount of electrical charge is accumulated on C_{PZ} due to the stress applied on the piezoelectric material (Phase I). The generated AC voltage is rectified through NVC. When the output of NVC, V_{RECT}, exceeds storage voltage V_{STOR}, RCD allows C_{STOR} to be charged through the swing of PEH beam (Phase II). Charging process continues until $V_{RECT} < V_{STOR}$ and then, RCD stops conduction by turning M_P OFF. In addition, RCD enables CFD and turns S_1 switches ON. During phase III, energy left on C_{PZ} is transferred to the external capacitance C_{EXT} through S_1 switches. C_{EXT} is chosen to be equal to C_{PZ} in order to achieve matched impedance for maximum power transfer. Considering the sign of piezoelectric voltage (V_{PZ}) detected with SD, CFD is activated to find the instant at which maximum amount of energy is transferred from C_{PZ} to C_{EXT}. Following the energy transfer from C_{PZ} to C_{EXT}, C_{PZ} is shorted in phase IV to discard the possible residual charge. The energy on C_{EXT} is transferred back to C_{PZ} in the reverse polarity by means of S_2 switches in phase V to complete the charge flipping process. CFD again monitors the moment that the maximum energy transfer from C_{EXT} to C_{PZ} is attained. Finally, system turns back to phase I in which all switches are OFF, and nodes V_{PIND}, V_{NIND}, and V_{NCAP} are shorted to ground to eliminate any residual charge on C_{EXT} and L_{EXT}, hence preventing oscillation. Simulation waveforms of V_{PZ}, V_{STOR}, i_{IND}, and grounding signal observed during SSHCI operation phases are depicted in Figure 3.6. While external inductor in the range of 27-68 µH is employed here, it is obvious that our novel SSHCI method is able to provide flipping efficiencies comparable with conventional SSHI circuits.

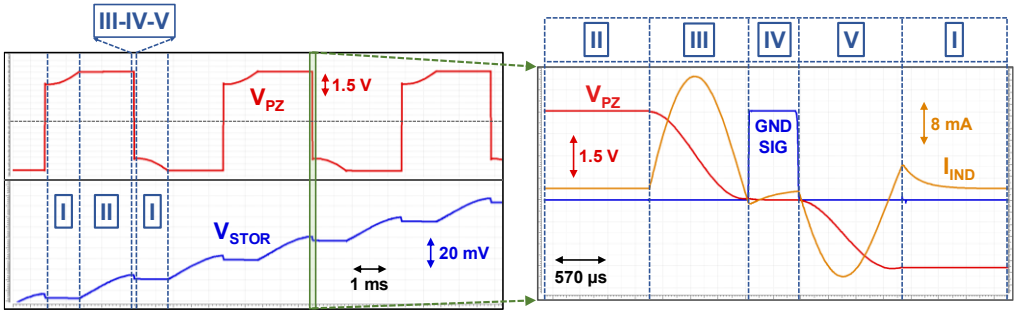

Figure 3.6. Simulation waveforms of piezoelectric voltage V_{PZ}, storage voltage V_{STOR}, and inductor current i_{IND} obtained during SSHCI operation phases.

Maximum extractable output power using SSHCI method is the same as equation (2.7) expressed in previous chapter [66], [75]. Furthermore, details of maximum output power derivation will be presented in chapter 4.

3.4. Implementation Details of SSHCI

SSHCI circuit has a fully autonomous architecture which can adapt its operation to changes in excitation frequency of PEH parameters such as C_{PZ}. In this section, building blocks of SSHCI circuit will be unveiled in detail.

3.4.1. Negative Voltage Converter (NVC)

Rectification of the AC voltage coming from PEH is conducted by NVC presented in Figure 3.7(a). Two NMOS switches M_{N1} and M_{N2} are controlled by two comparators shown in Figure 3.7(b). Comparators have current-follower input stages to monitor PEH terminal voltages V_{POS} and V_{NEG}. They decide which terminal is connected to ground for rectification purposes.

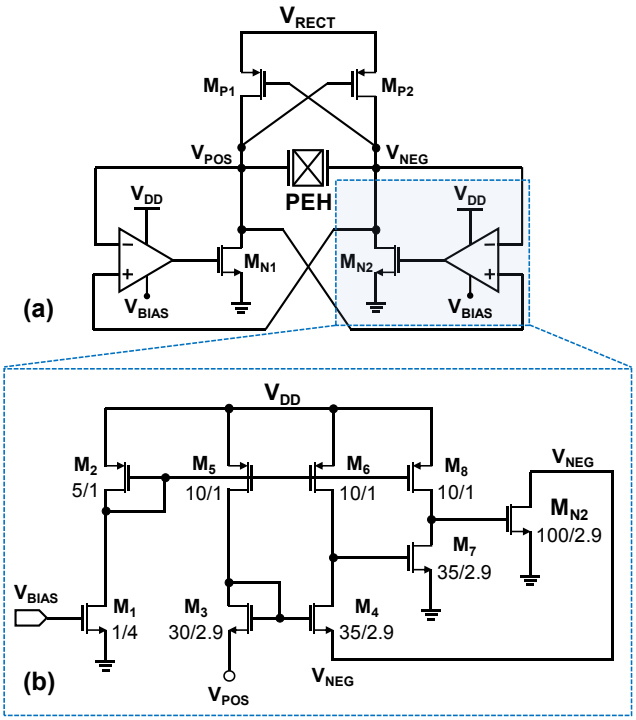

Figure 3.7. (a) Negative voltage converter (NVC) circuit implementation and (b) comparator utilized inside NVC design.

Cross-coupled PMOS switches M_{P1} and M_{P2} driven by PEH terminals help governing the charge flow path to supply a positive voltage. Mismatching created by different aspect ratios of M_3 and M_4 provides a more stable operation by preventing oscillation during transitions. This circuit uses 600 mV as its biasing voltage reference level. W/L ratios of designed comparator are given in Figure 3.7.

3.4.2. Reverse Current Detector (RCD)

RCD circuit basically determines the time duration when storage capacitor C_{STOR} is charged directly from PEH. Furthermore, it generates control signals governing M_P and S_1 switching operations. RCD is made up of a two stage common source amplifier which is used as comparator. It is shown in Figure 3.8 below.

RCD compares rectified piezoelectric voltage V_{RECT} with storage voltage V_{STOR} and if $V_{RECT} > V_{STOR}$, it creates a triggering output signal RCD_O. Input NMOS pair has a slight mismatch which speeds up the reaction time of the circuit. Two inverters at the output help transferring detection signal to the output with a correct shape since they provide amplification. RCD is disabled during phases III, IV, and V not to interrupt SSHCI operation. Simulation result of the proposed RCD circuit including generated detection signal RCD_O and charging current i_{CHARGE} is illustrated in Figure 3.9.

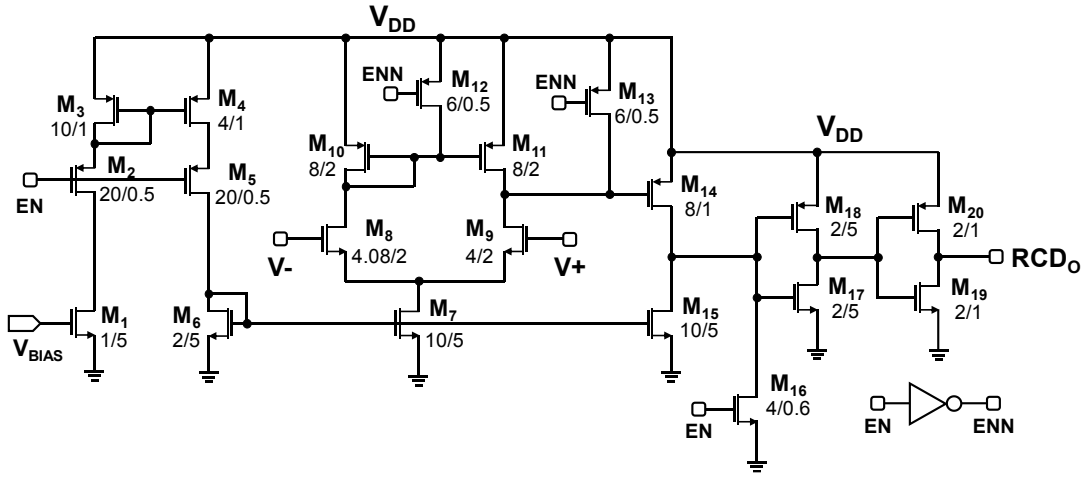

Figure 3.8. Reverse current detector circuit that is used to determine charging intervals of the storage capacitor C_{STOR}.

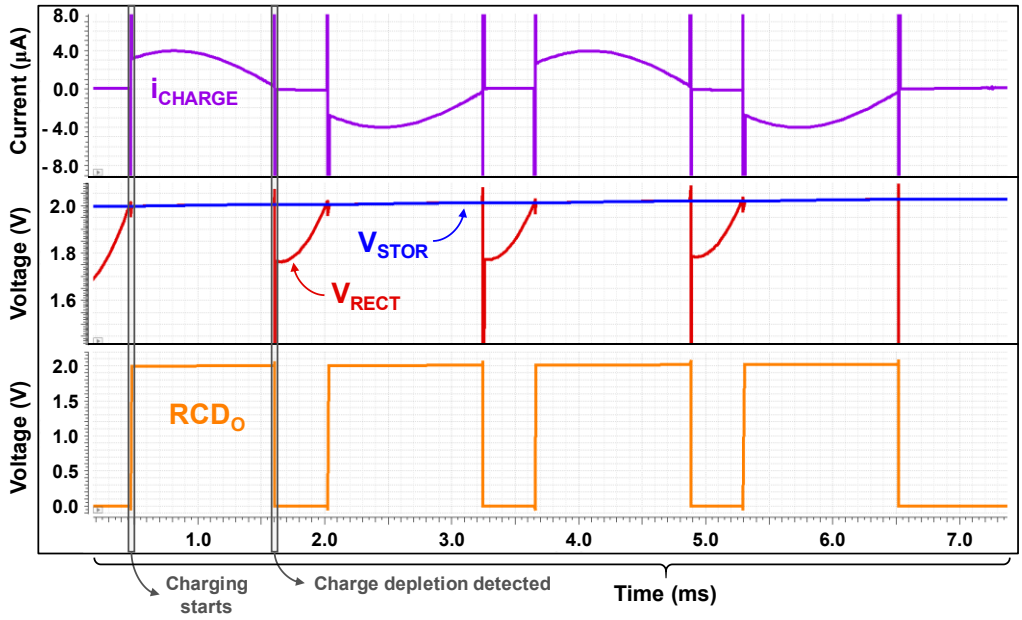

Figure 3.9. Simulation result of proposed RCD circuit that shows generated detection signal RCD_O and charging current i_{CHARGE}.

Magnitude of overall RCD voltage gain $|A_V|$ can be calculated as:

$$|A_V| = [g_{m8,9}(r_{O9} \parallel r_{O11})][g_{m14}(r_{O14} \parallel r_{O15})]|A_{INV1}||A_{INV2}| \quad (3.1)$$

$$|A_{INV1}| = (g_{m17} + g_{m18})(r_{O17} \parallel r_{O18}) \quad (3.2)$$

$$|A_{INV2}| = (g_{m19} + g_{m20})(r_{O19} \parallel r_{O20}) \quad (3.3)$$

where g_m represents transconductance of MOSFET transistors and r_O is the small signal output resistance. Since transistors in RCD operate in subthreshold region (weak inversion), g_m and r_O are expressed as [76]:

$$g_m \approx \frac{I_D}{\xi V_T} \quad \& \quad I_D = I_O exp \frac{V_{GS}}{\xi V_T} \quad (3.4)$$

$$r_O = \frac{1}{\lambda I_D} \quad (3.5)$$

where I_D is drain current, $\xi > 1$ is a nonideality factor, $V_T = kT/q$ is thermal voltage, I_O is proportional to W/L of the transistor under investigation, V_{GS} is gate-source voltage, and λ is channel length modulation parameter depending on process technology.

Since RCD is enabled most of the time, it possesses a low-power design and draws current levels less than 40 nA when is it working. Power consumption of RCD is crucial for overall chip efficiency of SSHCI technique because RCD is responsible for most of energy dissipated during operation.

3.4.3. Charge Flipping Detectors (CFD)

Flipping time monitoring configurations for the autonomous flipping operations conducted by S_1 and S_2 switches are depicted in Figure 3.10. In addition, Figure 3.11 illustrates the details of the charge flipping detector circuits. This configurations were proposed by us for the first time at 2019 CICC [73].

For the detection of maximum energy transfer point from C_{PZ} to C_{EXT} in phase III, PMOS input pairs were used, since compared voltage levels are below half of the supply voltage level (V_{STOR}=V_{DD}), which better fits to common mode range of PMOS input pairs. Similarly, NMOS input pairs were utilized in phase V to find the maximum energy transfer instant from C_{EXT} back to C_{PZ}, as compared voltage levels are above the half of V_{STOR}. MOSFETs M_{11} in CFD_1 and M_{10} in CFD_2 are of low threshold type (V_{TH}≈300 mV). This extends the common mode voltage range, and increases the bandwidth. To avoid waste of power, both circuits are completely disabled during the phases they are not used.

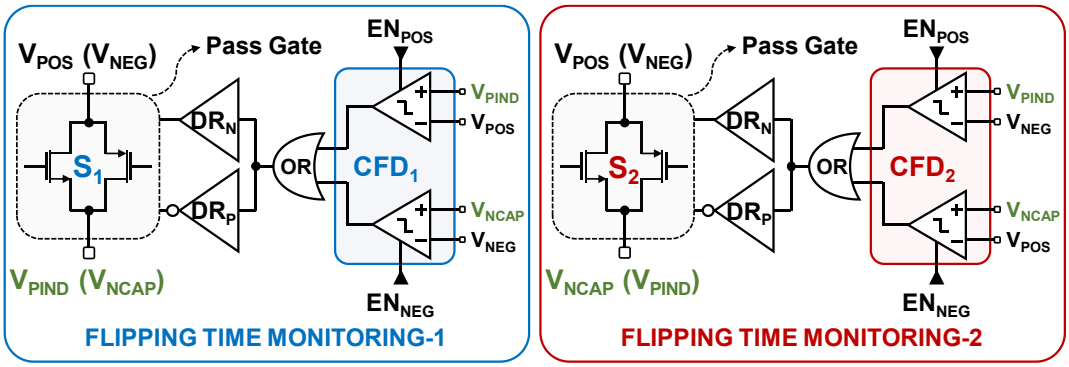

Figure 3.10. Flipping time monitoring architectures established for (a) S_1 and (b) S_2 switching operations.

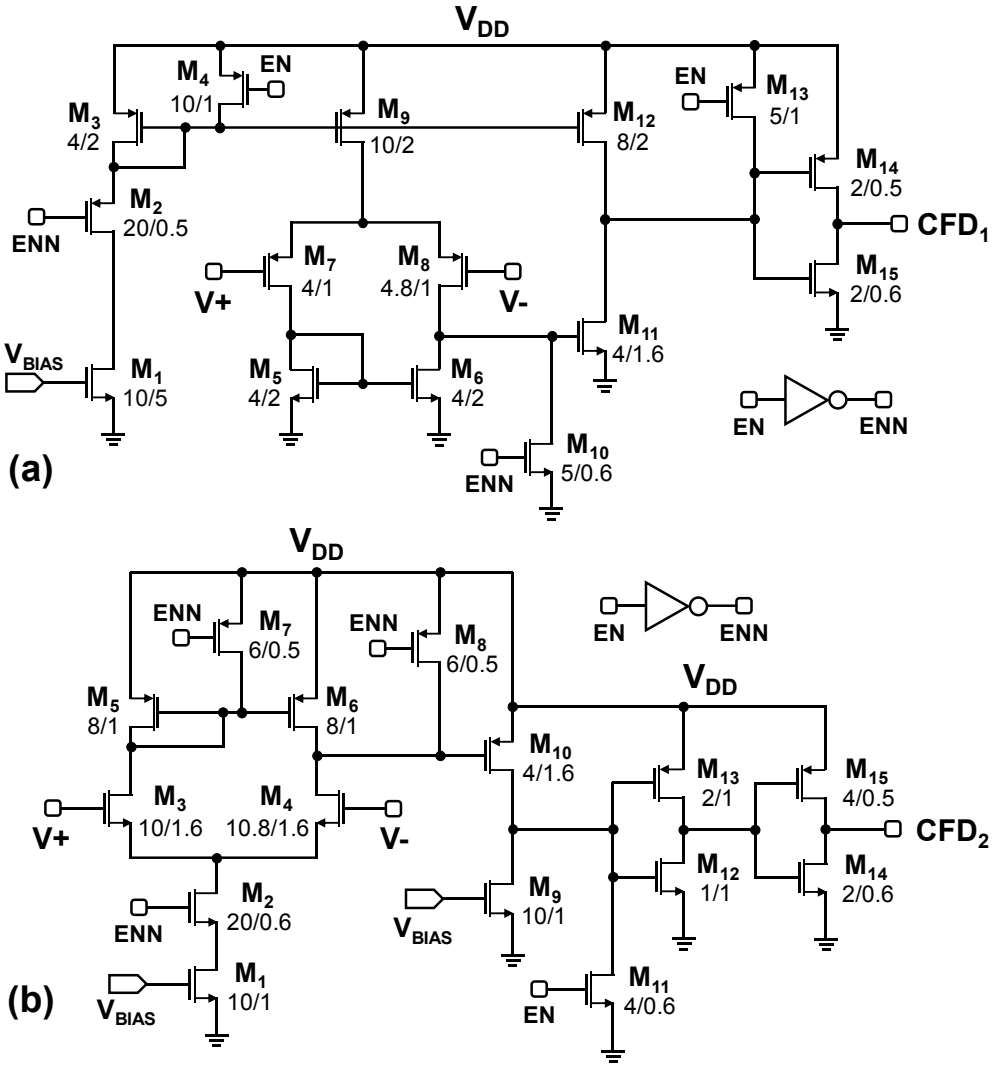

Figure 3.11. Schematic details of comparators used as (a) charge flipping detector-1 (CFD_1) and (b) charge flipping detector-2 (CFD_2).

Figure 3.12 exhibits simulation waveforms obtained for proper charge flipping monitoring operation. When S_1 switches turn ON in phase III, current starts passing from C_{PZ} to C_{EXT} and V_{POS} voltage begins to drop (given that PEH swings in positive half cycle). The moment that V_{POS} and V_{PIND} voltages cross corresponds to the time that all the energy is transferred to C_{EXT}. As it can been seen from Figure 3.12(a), CFD_1 finds this instant correctly with a little delay which does not affect flipping operation much. Likewise, Figure 3.12(b) proves appropriate CFD_2 activity in which energy is relocated back to C_{PZ} from C_{EXT}.

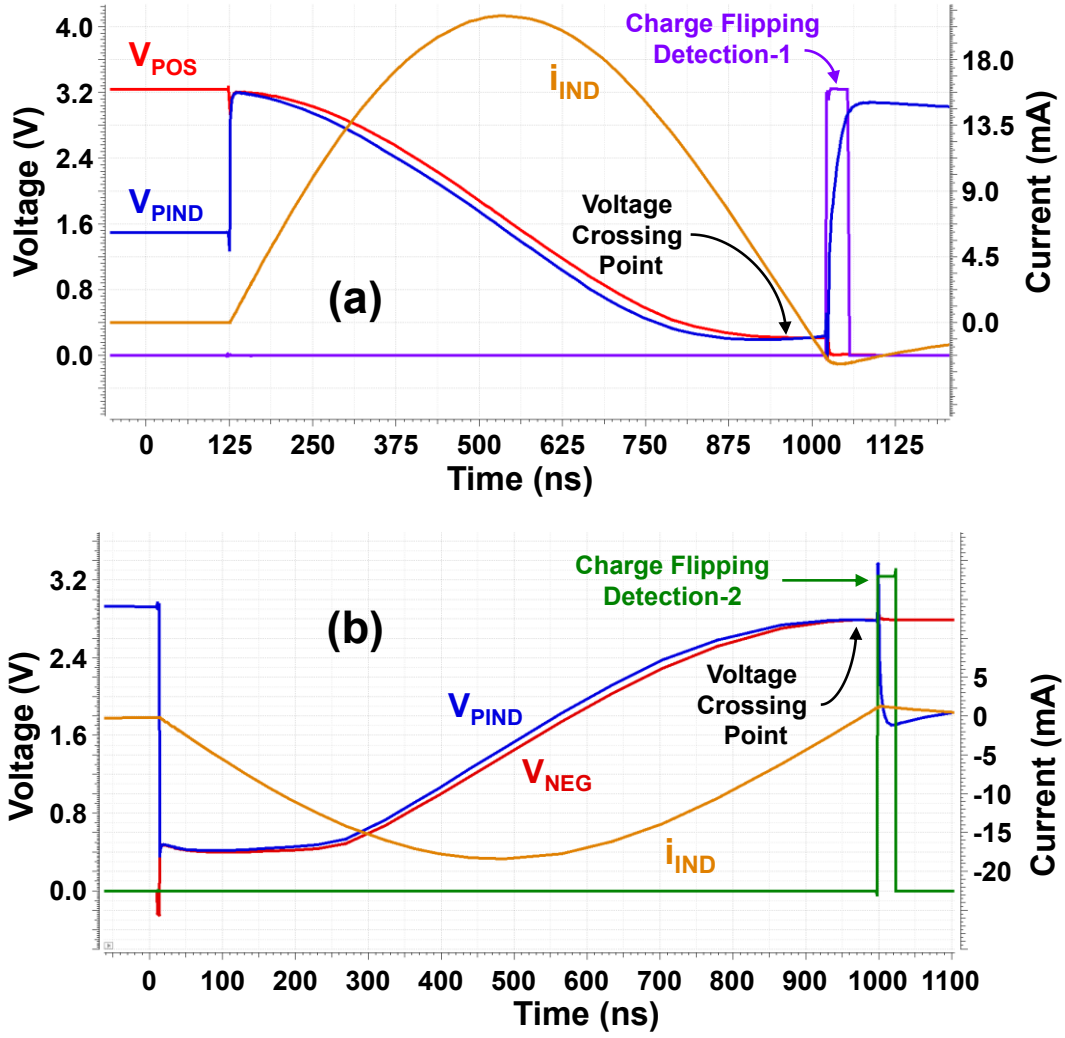

Figure 3.12. Simulation waveforms of fully autonomous charge flipping monitoring for (a) CFD_1 and (b) CFD_2 circuits.

3.4.4. Shorting Pulse Generator (SPG)

Control unit of SSHCI regulating the timing of the charge flipping switches activity is very critical. It is mainly composed of digital logics like AND, OR, NOT gates and SR latches. Adjustable pulse generator proposed by us in [45] is responsible by generation of non-overlapping control input signals of SR latches in SSHCI. However, those control signal pulses have around 30 ns pulse width which is not sufficient to be used in shorting PEH terminals in phase IV. Consequently, shorting pulse generator (SPG) circuit presented in Figure 3.13 was designed to provide

adequate pulse duration in phase IV to eliminate any residual charge on piezoelectric capacitance C_{PZ} after charge transfer to C_{EXT}. This circuit is the modified version of our adjustable pulse generator circuit in [45]. It is a very simple circuit with an additional voltage bias pin V_{PG} for controlling the pulse duration. As input goes from low to high, transistor M_6 senses this input change before M_5 and M_7 making these two transistors work as an inverter. Since off-chip capacitor C_D is fully charged, gates of M_9 and M_{10} become low and an output pulse is observed. Simulation result of SPG that generates different output pulse widths in response to various V_{PG} voltage levels is depicted in Figure 3.14 below.

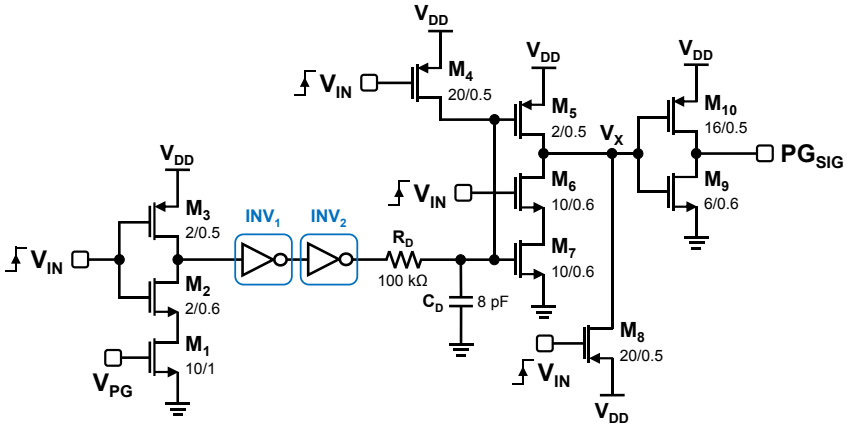

Figure 3.13. Schematic of the shorting pulse generator (SPG) circuit whose output pulse width can be adjusted with its biasing voltage V_{PG} [45].

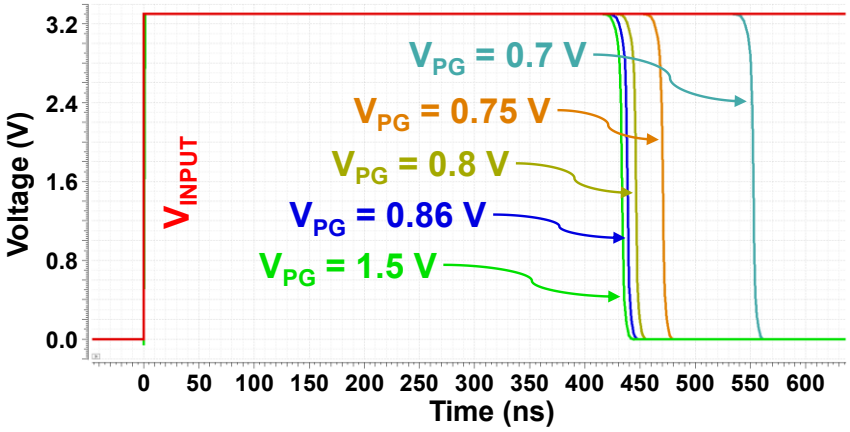

Figure 3.14. Simulation result of SPG generating different output pulse widths (PG_{SIG}) in response to a range of V_{PG} voltage levels.

Gates on M_5 and M_7 realize the input change with a delay generated by inverters and RC circuit as shown in Figure 3.13. This delay can be given as in equation (3.6). However, actual generated pulse is less than t_{delay} because transistor M_7 turns on around 700 mV and therefore C_D does not have to be fully charged to generated output pulse PG_{SIG}.

$$t_{delay} = t_{INV1} + t_{INV2} + 5R_D C_D \tag{3.6}$$

3.4.5. Start-up Trigger Circuit

Cold start-up configuration is embodied into SSHCI circuit so that harvesting system can charge output load from initially depleted condition. Figure 3.15 reveals schematic of start-up triggering circuit. As the battery is being charged from zero voltage with PEH motion, reference voltage V_{BIAS} will be generated. Then, elevated V_{BIAS} voltage will lead to increased biasing current passing through M_6. This will build up voltage on gates of M_6, M_8, and M_9 which are initially at zero voltage. After some point, it will trigger the inverter made up of M_8, and M_9 and overall enable signal EN_{TRIG} will be generated to start system operation. After SSHCI system is fully operational, start-up sub-system is disabled to reduce power consumption. The imperative point in this design is that bias voltage V_{BIAS} can tune the triggering voltage level where output signal EN_{TRIG} is created.

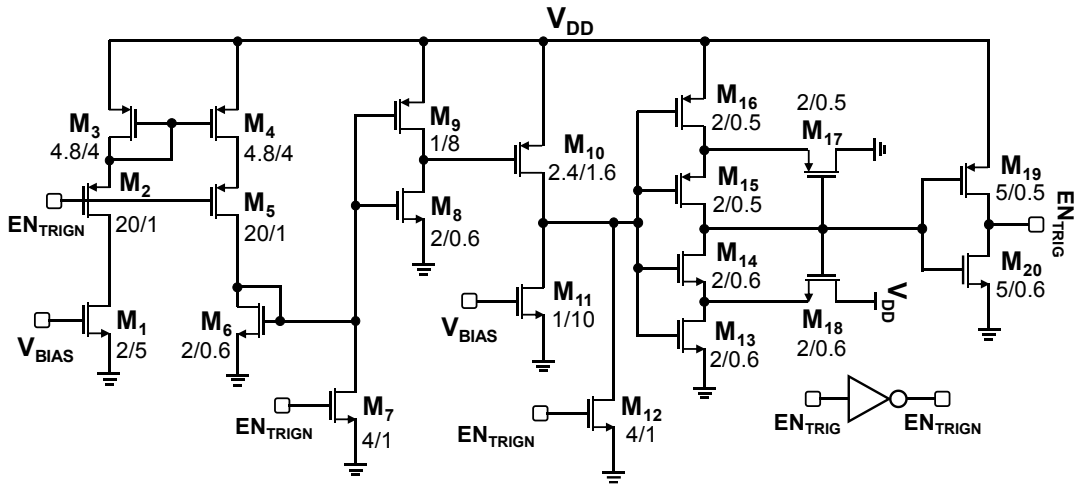

Figure 3.15. Schematic of Start-up trigger circuit.

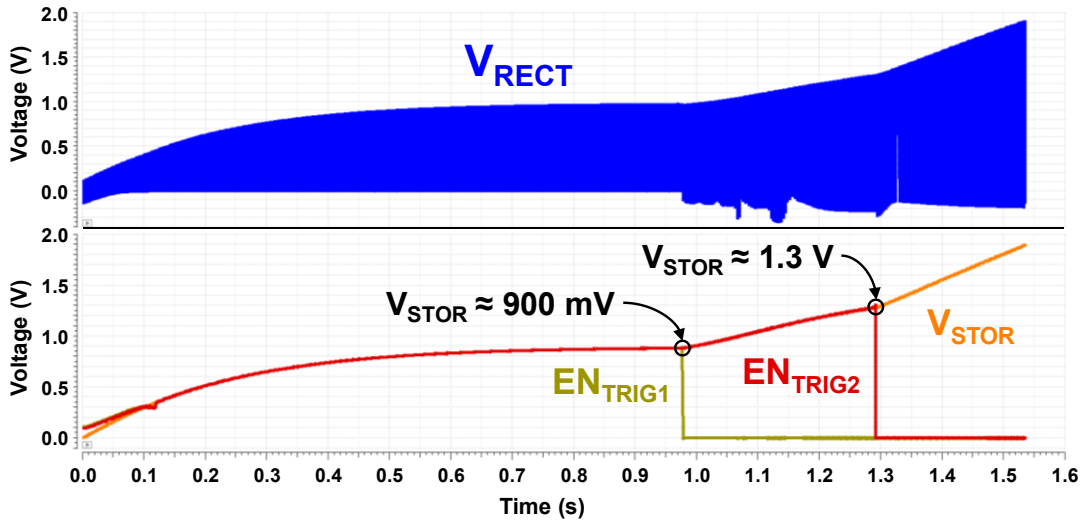

Figure 3.16. 2-stage start-up simulation of SSHCI circuit where RCD operation starts when V_{STOR} reaches 0.9 V and flipping begins after V_{STOR} passes around 1.3 V to ensure proper operation.

In start-up design as a whole sub-system, a two-stage triggering configuration is used where two different triggering output signals are generated depending on different bias voltages. This is because flipping control circuit and detectors are enabled after the second triggering circuit which helps us speed up the cold start operation. Figure 3.16 above illustrates 2-stage start-up simulation result of SSHCI system. Two start-up trigger circuits presented in Figure 3.15 are employed in the start-up sub-block. EN_{TRIG1} signal enables only RCD circuit when V_{STOR} reaches around 900 mV. It is clear from Figure 3.16 that RCD operation significantly accelerates charging between 1 and 1.3 seconds. When V_{STOR} is arrived around 1.3 V, whole SSHCI phases are launched following EN_{TRIG2} signal.

3.4.6. Voltage Reference Circuit

Almost every sub-circuit operation in SSHCI design relies on some reference voltage levels to work as expected. Hence, voltage reference circuits are critical building blocks of a mixed-signal circuit. Reference circuit used in SSHCI design, provided in Figure 3.17, is a modified version of 2T voltage reference published in [77] where all theoretical calculations about reference levels exist. Depletion NMOS transistor (zero threshold transistors) supply required biasing current for transistors M_1, M_3, and M_5.

Generated reference voltages are temperature and supply independent [78]. Simulation result of voltage reference circuit is displayed in Figure 3.17(b).

3.5. Experimental Results

SSHCI circuit was fabricated with 180 nm standard CMOS technology from TSMC Company. Die occupies 2.44 mm x 2.44 mm (5.95 mm^2) total area whereas active area used by SSHCI is 0.85 mm x 1.1 mm (0.94 mm^2). Micrograph of the fabricated die is shown in Figure 3.18.

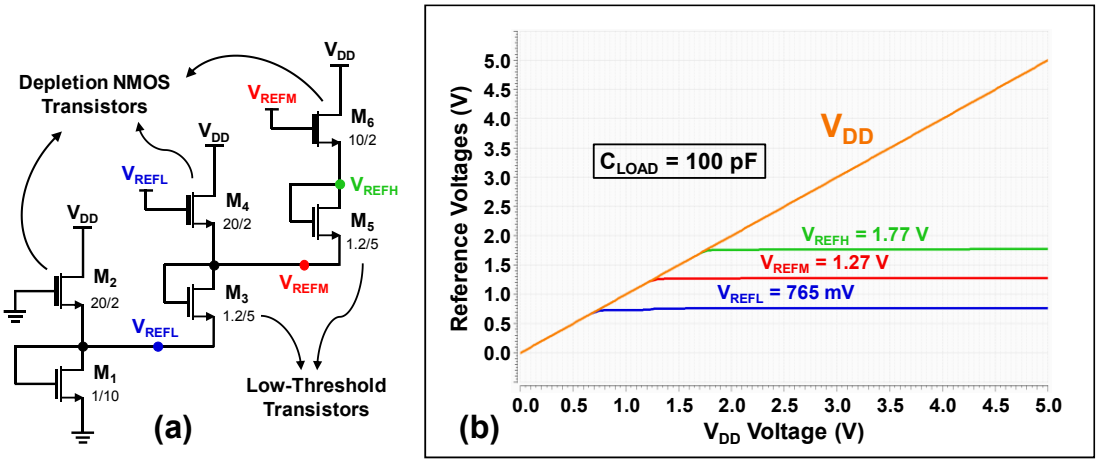

Figure 3.17. (a) Schematic of the modified 2T voltage reference presented in [77] and (b) simulation result indicating produced reference voltage levels.

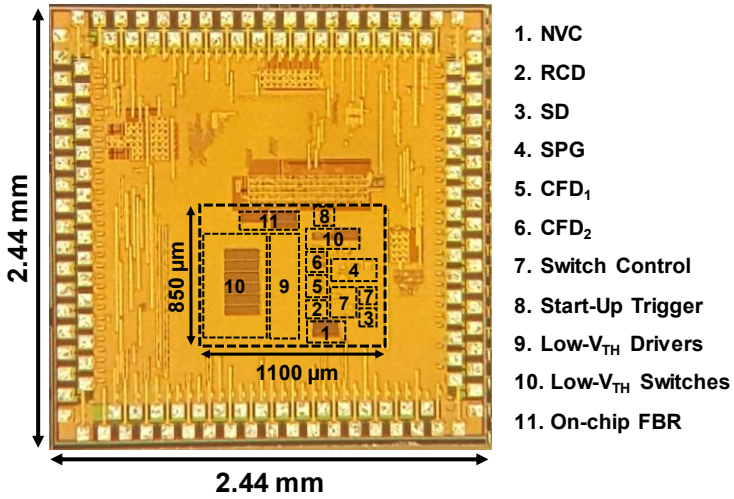

Figure 3.18. Die micrograph of the implemented SSHCI chip.

A custom-made MEMS based PEH with C_{PZ} = 2 nF was utilized to validate the performance of SSHCI interface. Block diagram and picture of test setup established to conduct experiments on fabricated chips are illustrated on Figure 3.19 and 3.20, respectively.

Shaker table vibrates MEMS based PEH with its resonance frequency which is controlled with the help of a software. SSHCI chips employ 1210 (3225 in mm) SMD inductors in the range of 27-68 µH which occupy around 18 mm^3 space. Of course, an external capacitor C_{EXT} = C_{PZ} is needed in SSHCI operation; however, SMD capacitors in the range of nF's can be as small as 1 mm^3. Therefore it does not add too much of space to overall volume. A 453 nF capacitor was utilized as storage capacitor C_{STOR} to see charging effect clearly.

In the following sections, experimental start-up operation details, functional verification of SSHCI phases with observed waveforms of storage (or battery) voltage, PEH terminals and output power and power conversion efficiency measurement will be investigated deeply. Finally, discussion section will present comparison of SSHCI to other state-of-the-art designs existing in the literature.

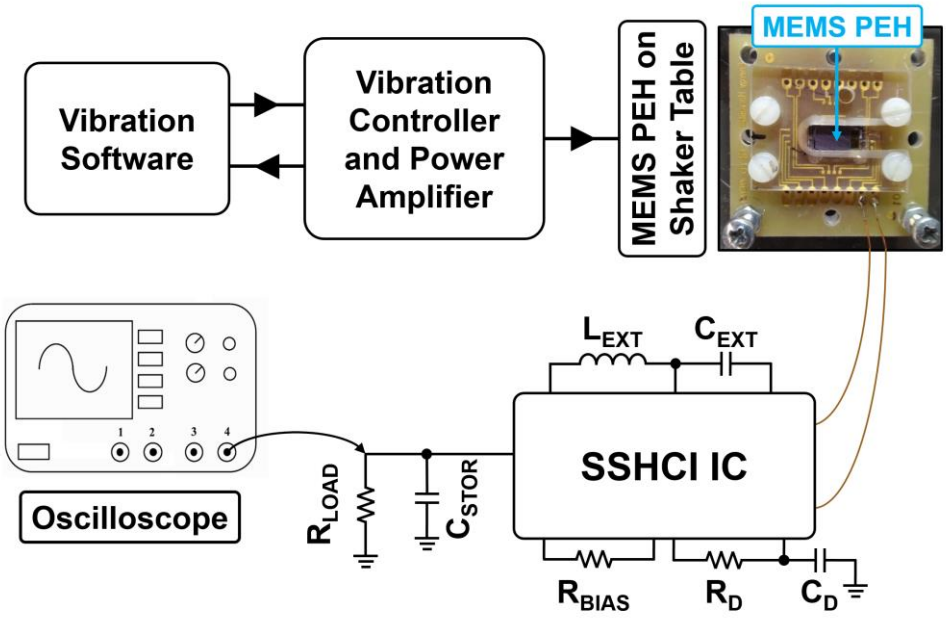

Figure 3.19. Block diagram of SSHCI test setup and devices used.

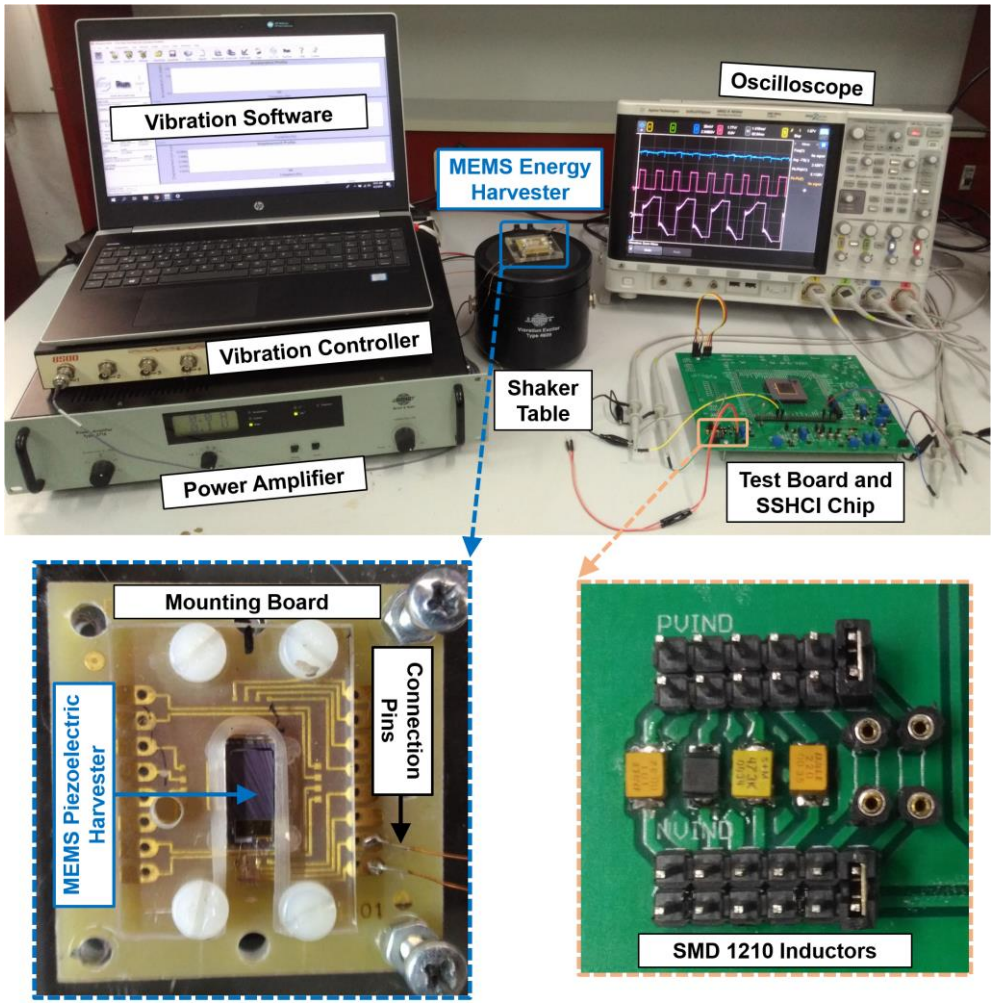

Figure 3.20. Picture of test setup used for performance measurement of SSHCI interface. MEMS PEH was excited with vibration setup composed of software, controller, power amplifier, and shaker table. 68 µH, 47 µH, and 27 µH SMD 1210 inductors were utilized for voltage flipping purposes.

3.5.1. Start-up Operation

Figure 3.21 displays measured waveforms of V_{RECT}, V_{POS}, V_{NEG}, V_{STOR}, and enable signal EN_{TRIG2} for charging from V_{STOR} = 0 V. Entire start-up operation, depicted in Figure 3.21(a), is composed three phases. Firstly, C_{STOR} is charged via NVC and on-chip diode connected transistor D_S as shown in Figure 3.21(b). When V_{STOR} reaches around 850 mV, RCD starts its operation with the first enable signal coming from the first start-up trigger circuit. Figure 3.21(c) presents measured waveforms of RCD output (RCD_O), V_{STOR}, V_{POS}, and V_{NEG} during RCD only phase of start-up.

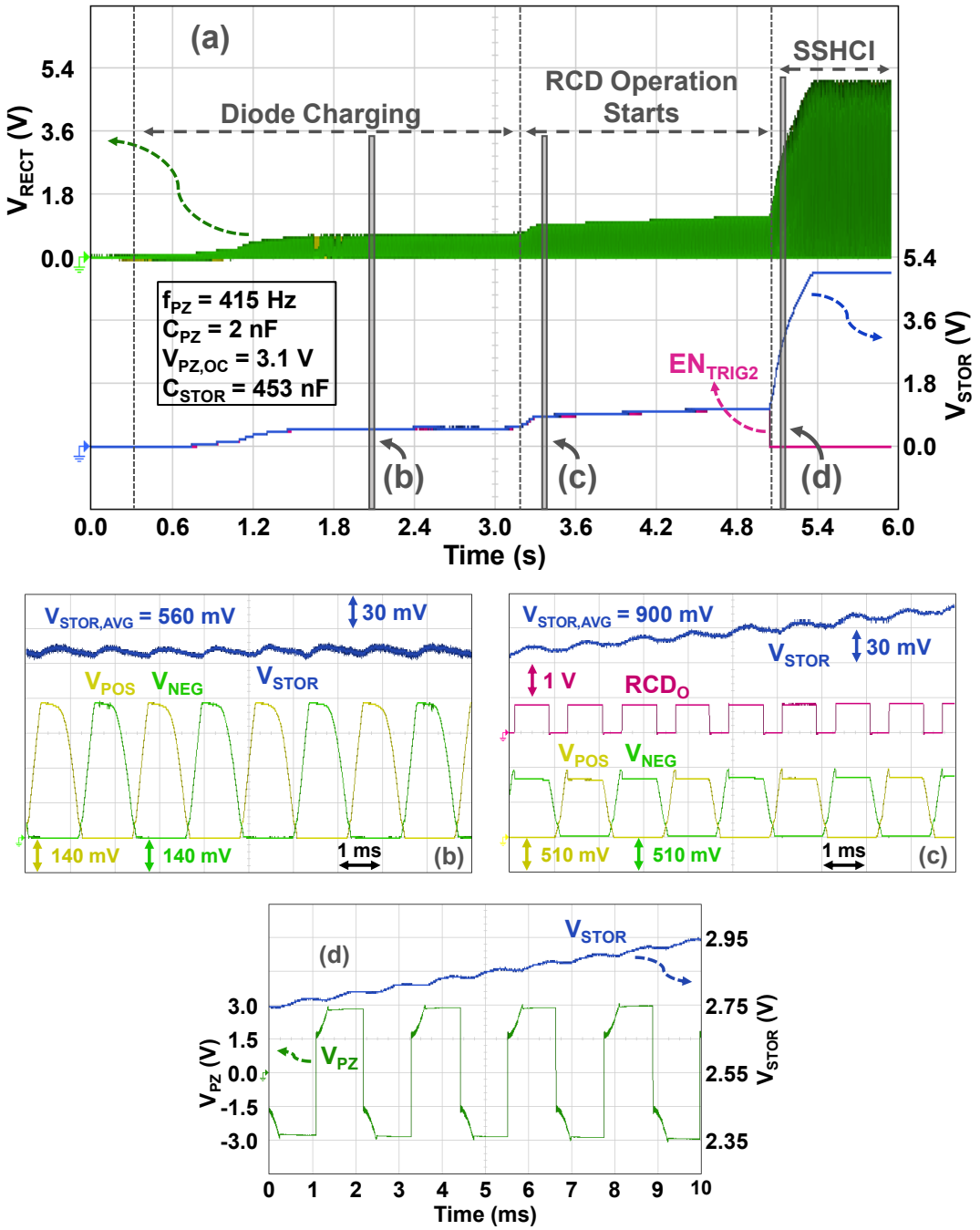

Figure 3.21. Measured waveforms of SSHCI circuit illustrating (a) overall 2-step start-up operation, (b) diode only charging at start-up, (c) RCD only charging at start-up, and (d) SSHCI charging.

Lastly, SSHCI operation begins as V_{STOR} arrives around 1.3 V. Figure 3.21(d) gives us proper SSHCI flipping operation and charging of storage capacitor C_{STOR}. SSHCI circuit can charge C_{STOR} up to 5 V which is determined by process specifications.

3.5.2. Functional Verification of SSHCI

Figure 3.22 depicts measured waveforms of piezoelectric voltage V_{PZ}, reverse current detector output RCD_O, and inductor current i_{IND} during operation phases. SSHCI circuit is able to perform its functionality with success while employing a MEMS based PEH as its input source. Aforementioned five operation phases of SSHCI are observed clearly as shown in the figure below where L_{EXT} = 47 µH inductor was utilized during functional verification. If the inductance value is enlarged, flipping efficiency will increase.

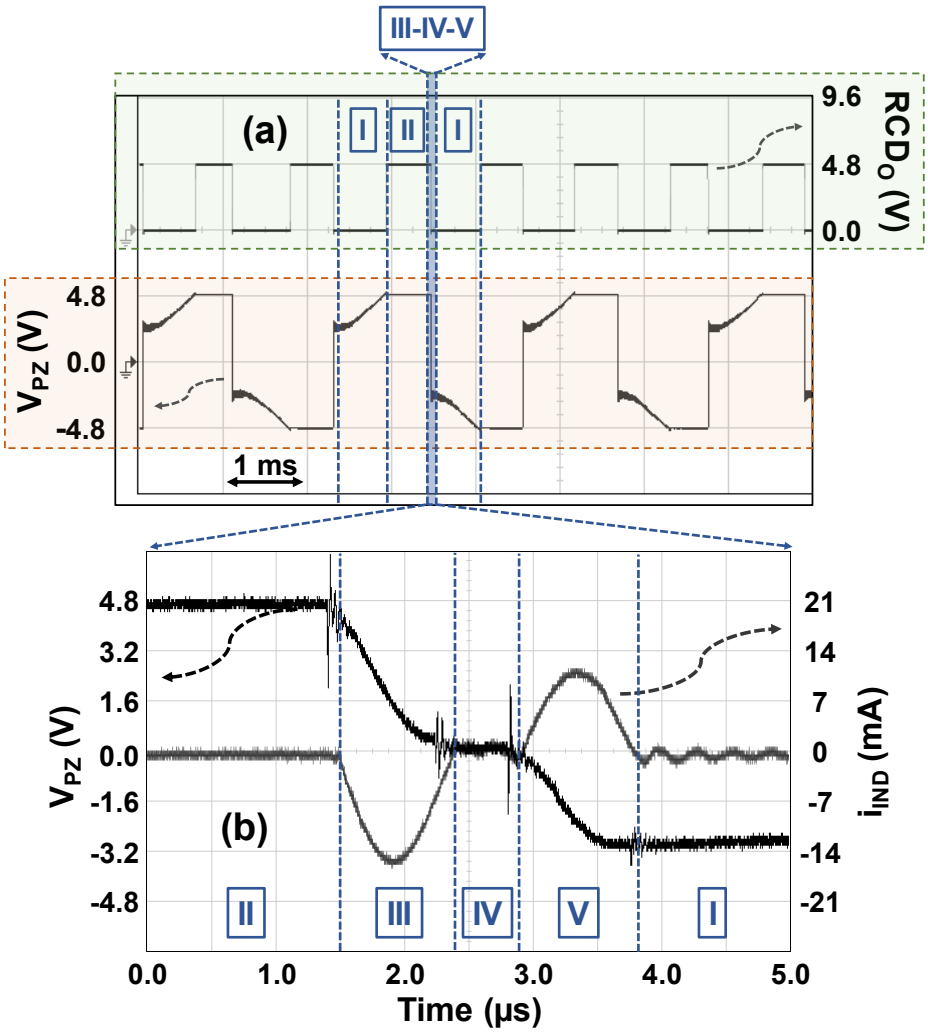

Figure 3.22. Measured waveforms of (a) piezoelectric voltage V_{PZ}, reverse current detector output RCD_O, and (b) inductor current i_{IND} during operation phases.

Figure 3.23 reveals details of measured control signals that make SSHCI method work as expected. It is important to note that SSHCI gives us flexibility to control shorting pulse duration which is strongly related to the PEH used as input source. If more charge than expected is left on C_{PZ} after flipping, we are able to increase shorting pulse duration to eliminate any residual.

Figure 3.23(a) and 3.23(b) exhibit charge flipping detection signals with a little bit of delay. However, one can achieve detection of exact point where two voltages are crossing via adjusting biasing voltages of charge flipping detection comparators. Another point observation signals CFD_1 and CFD_2 is that since they are not larger than 30 ns, they are hard to observe and noise can easily couple these observation signals.

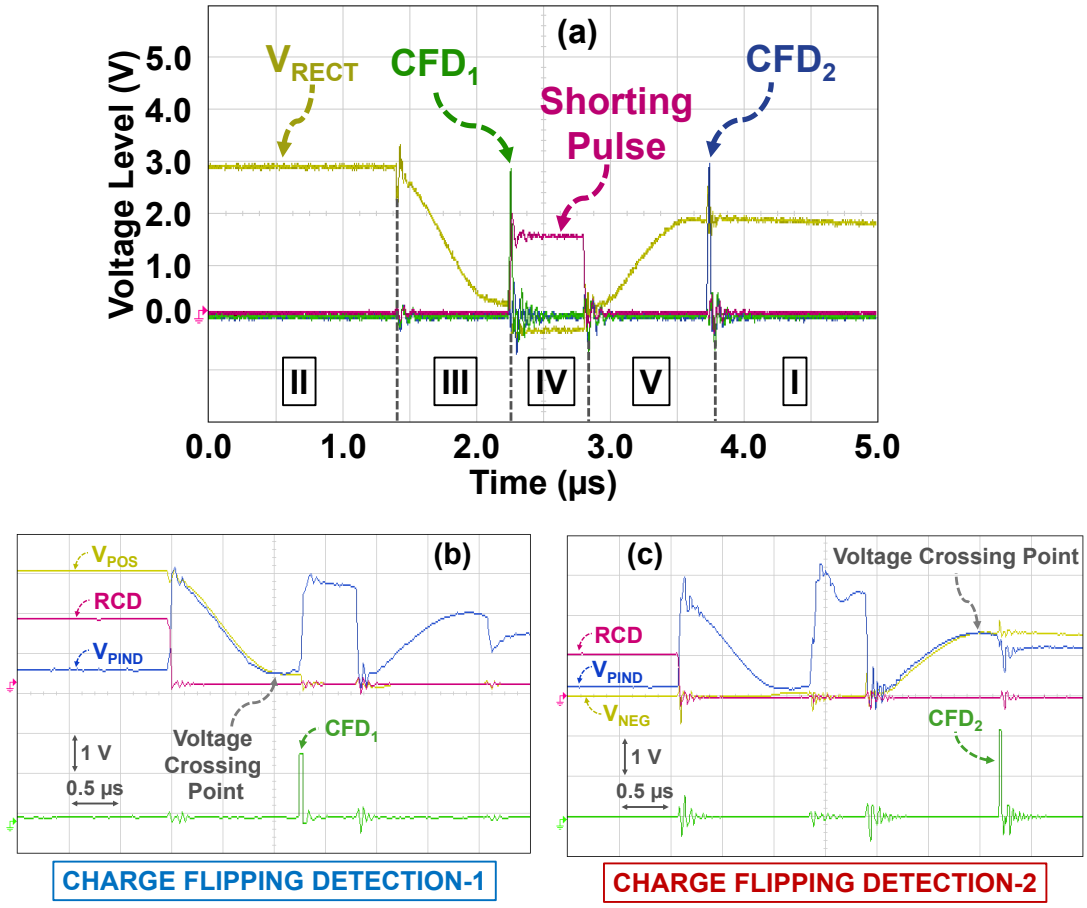

Figure 3.23. (a) Control signals generated during voltage flip operations and measured charge flipping detection signals for (b) CFD_1 and (c) CFD_2.

3.5.3. Output Power Improvement and Power Conversion Efficiency

Figure 3.24 shows measured output power of SSHCI circuit for different piezoelectric open circuit voltage ($V_{PZ,OC}$) amplitudes. During these measurements, shaker table was excited with 415 Hz which is the resonant frequency of the MEMS PEH. SSHCI is able to provide 6.14x relative performance improvement over maximum output power of an ideal FBR for $V_{PZ,OC}$ = 0.95 V (Figure 3.24(a)). For larger $V_{PZ,OC}$ levels (Figure 3.24(b)), relative performance improvement reduces due to larger damping and larger displacements of the transducer. Still, it is possible to boost SSHCI performance for large damping by making use of larger inductance values.

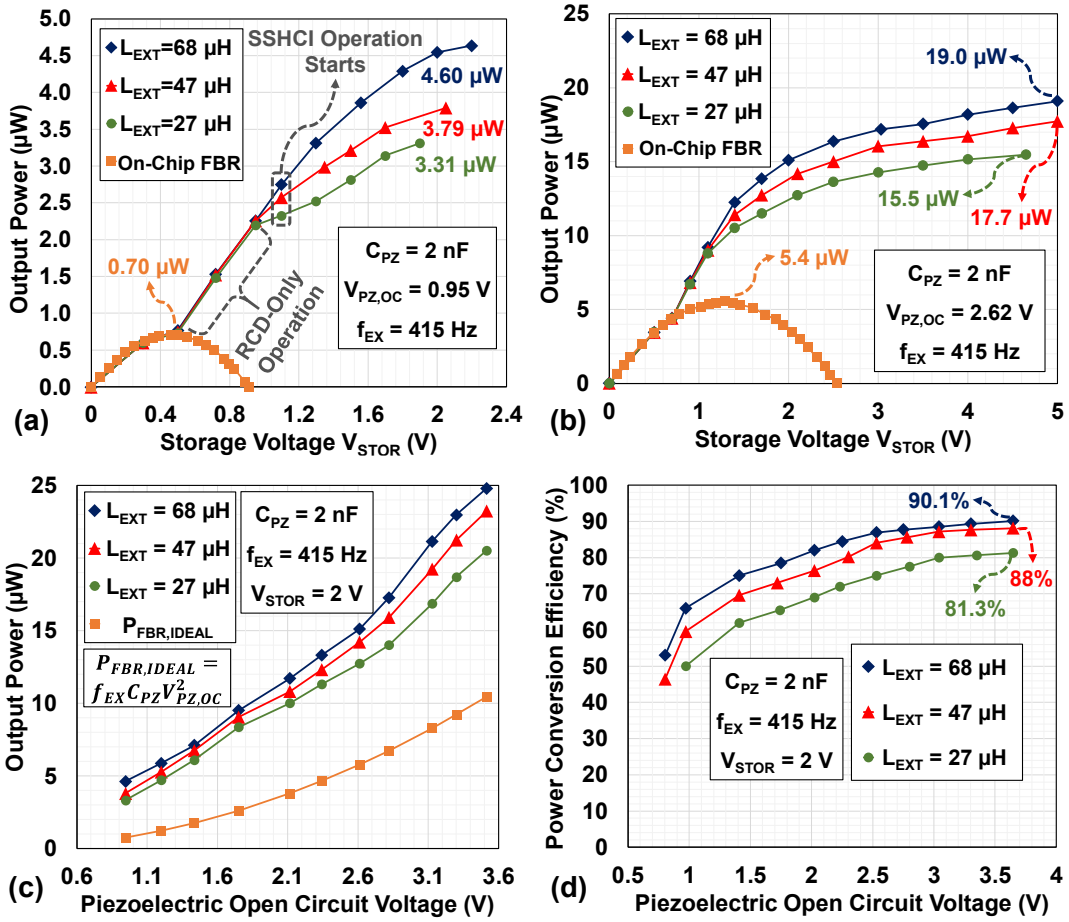

Figure 3.24. (a, b) Measured output power provided by self-powered SSHCI circuit compared to on-chip full-bridge rectifier (FBR) with different piezoelectric open circuit voltage levels $V_{PZ,OC}$, and (c) ideal FBR, and (d) power conversion efficiency of the operation.

Measured power conversion efficiency ($\eta=P_{OUT}/P_{IN}$) for different L_{EXT} values given in Figure 3.24(d) reveals that SSHCI circuit achieves around 90.1% conversion efficiency (P_{IN} = 27.55 µW) for L_{EXT} = 68 µH, which is higher than the efficiency reported by previous designs with large inductors [48], [52], [54], [55], [59], [72].

3.6. Discussion

Table 3.2 below provides comparison of the SSHCI test chip performance against the state of the art piezoelectric energy harvesting interface circuits.

Table 3.2. *Comparison of the implemented SSHCI IC with state-of-the-art interface circuits.*

Reference	[48]	[79]	[54]	[72]	[70]	This Work [73]
Technology	350 nm	350 nm	320 nm	350 nm	180 nm	180 nm
Scheme Type	SSHI	Energy Investment	SECE	SSHI	FCR	SSHCI
C_{PZ}	12 nF	15 nF	52 nF	26 nF	80 pF	2 nF
Excitation Frequency	225 Hz	143 Hz	60 Hz	225 Hz	110 kHz	415 Hz
Inductor (Volume)	22-820 µH (NA)	330 µH (126 mm^3)	10 mH (NA)	3.3 mH (15.2 cm^3)	NO	27-68 µH (18 mm^3)
Flipping Time Detection	External Adj.	NA	NA	External Adj.	External Adj.	**Autonomous Adj**.
Cold Start-up	NO	NO	YES	YES	YES	YES
Peak Conversion Efficiency	87[2]%	69.2%	85.3[3]%	88[4]%	NA	**90.1% (68 µH)** 88% (47 µH) 81.3% (27 µH)
Power Extraction Improvement (FOM[1]x100)	420[5]%	360%	351%	440%	483[6]%	**614% (68 µH)** **506% (47 µH)** 441% (27 µH)
Chip Size	4.25 mm^2	2.34 mm^2	0.95 mm^2	0.72 mm^2	1.70 mm^2	0.94 mm^2

(1) FOM = $P_{OUT}/f_{EX}V_{PZ,OC}^2C_{PZ}$
(2) It is only for DC-DC converter.
(3) External supply was used.
(4) Calculated from paper.
(5) Calculated with respect to off-chip FBR
(6) Calculated with respect to on-chip FBR.

Although flipping capacitor rectifier (FCR) in [70] offers an inductorless design, its figure of merit (FOM), which is defined as FOM = $P_{OUT}/f_{EX}V_{PZ,OC}^2C_{PZ}$, and power conversion efficiency are inferior to SSHCI. Besides, compared to the literature, SSHCI circuit, which has a fully autonomous charge flipping time detection, can achieve higher efficiency and FOM by utilizing low-profile inductors. This is clearly a huge step towards miniaturization in electronic circuits used for piezoelectric energy harvesting. Thanks to low power design techniques, SSHCI can reach power conversion efficiencies even for low-level input excitations or vibrations. Inherent capacitance value C_{PZ} of PEH plays an important role in SSHCI operation. SSHCI performs better with small C_{PZ} values (such as 2 nF) as amount of charge that needs to be flipped is modest. If C_{PZ} is increased, the circuit may need larger L_{EXT} component to achieve high voltage flipping efficiency. Moreover, SSHCI circuit changes bending of PEH beam during its swing with ambient vibrations but this does not disturb SSHCI operation phases.

Still, SSHCI method needs improvements in some ways. First of all, current RCD design is strongly biasing voltage dependent, that is, RCD circuit requires different biasing voltages for different V_{DD} levels to perform well. External flipping capacitor C_{EXT} should be equal to C_{PZ} to transfer maximum energy during flipping and sometimes, it is hard to find C_{EXT} values exactly same as C_{PZ}. Deviations of C_{EXT} values form C_{PZ} affects charge flipping efficiency in a bad way. Another problem is that output power generated by SSHCI alters with different battery voltage levels (or storage voltage levels). A special mixed-signal circuit is needed to extract maximum energy from PEH no matter what the battery voltage is. A low power maximum power point tracking (MPPT) circuit may be a solution to that issue.

CHAPTER 4

LOW PROFILE PIEZOELECTRIC ENERGY HARVESTING INTERFACE CIRCUIT WITH INTEGRATED NOVEL MAXIMUM POWER POINT TRACKING

4.1. Motivation

Most of the wireless sensor networks (WSNs) demand fixed supply voltage and stable power levels for proper operation. One of the problems that SSHCI circuit presented in the previous chapter possesses is load dependency, that is, output power level alters with different V_{STOR}. It can be solved by employing a maximum power point tracking (MPPT) system. There are various MPPT architectures implemented in energy harvesting literature [61], [65], [80]. Both [61] and [65] integrates MPPT structure inside SSHI technique where optimum battery voltage is adjusted externally through resistive division in [61]. On the contrary, MPPT systems in [65] and [80] optimum voltage autonomously with circuit operations for input powers larger than 100 μWs. Unfortunately, they are all not suitable for low level output powers especially below 50 μW. Therefore, we need to come up with a new MPPT structure that can work seamlessly with low coupled (low output generation) PEHs. The goal of this chapter is to introduce a novel MPPT system which simultaneously operates along with modified SSHCI circuit. Section 4.2 presents optimal storage voltage calculation where maximum output power is extracted from low coupled PEH. Top level operation principle and working phases of second generation SSHCI circuit with integrated MPPT (SSHCI-MPPT) is given in section 4.3. Following section 4.4 demonstrates implementation details of SSHCI-MPPT sub-blocks. Experimental performance results are reported in section 4.5. Finally, discussion section provides a detailed performance comparison of SSHCI-MPPT circuit with recent piezoelectric energy harvesting interface circuits in the literature.

4.2. Optimal Storage Voltage Calculation

Since our MEMS PEH that is used to verify functionality and performance of harvesting interface circuits has low piezoelectric coefficient and weak electromechanical coupling, PEH can be modelled with intrinsic piezoelectric capacitance C_{PZ} parallel with dependent current source i_{PZ} as shown in Figure 4.1 [66]. In half period of i_{PZ} oscillation with external vibrations, total produced charge by PEH can be calculated as follows:

$$Q_{TOTAL} = 2V_{OC,P}C_{PZ} \tag{4.1}$$

where $V_{OC,P}$ is the amplitude of the produced piezoelectric open circuit voltage. Although SSHI operation flips most of residual charge after energy transfer to output load, there exists flipping loss and some amount of generated charge on PEH is needed to make up for this loss. Therefore, net electric charge transferred to storage capacitance C_{STOR} when we connect PEH to SSHI circuit is:

$$Q_{NET} = 2V_{OC,P}C_{PZ} - (V_{STOR} - V_F)C_{PZ} \tag{4.2}$$

The extracted output power in half period of i_{PZ} oscillation can be calculated as:

$$P_{NET} = \frac{V_{STOR}Q_{NET}}{T/2} = 2f_{EX}C_{PZ}V_{STOR}(2V_{OC,P} - V_{STOR} + V_F) \tag{4.3}$$

where f_{EX} is the external excitation frequency of PEH and V_F is the flipped voltage level thanks to SSHI operation. V_F voltage is related with V_{STOR} as given in the following:

$$\eta_F = \frac{V_F + V_{STOR}}{2V_{STOR}} \leftrightarrow V_F = V_{STOR}(2\eta_F - 1) \tag{4.4}$$

where n_F is the flipping efficiency. Combining equations (4.3) and (4.4), we reach at:

$$P_{NET} = 4f_{EX}C_{PZ}V_{STOR}(V_{OC,P} + V_{STOR}[\eta_F - 1]) \tag{4.5}$$

To find optimum storage voltage for maximum output power, we will take derivative of P_{NET} with respect to V_{STOR} and make it equal to zero (equations (4.6) and (4.7)).

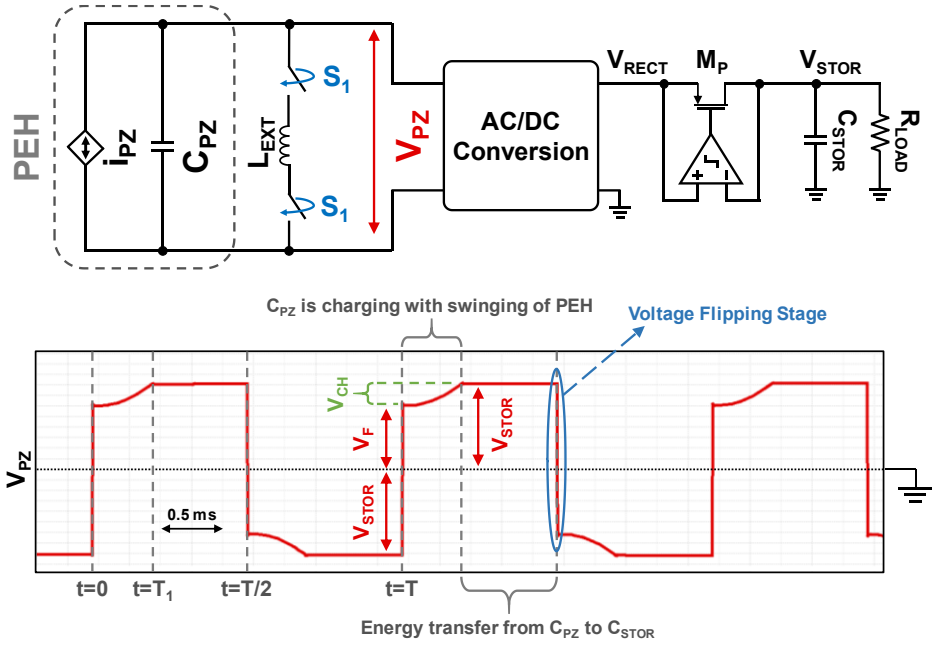

Figure 4.1. Schematic of conventional SSHI circuit and associated simulation waveform.

$$\frac{dP_{NET}}{dV_{STOR}} = 0 = 4f_{EX}C_{PZ}V_{OC,P} + 8f_{EX}C_{PZ}V_{STOR,OPT}(\eta_F - 1) \tag{4.6}$$

$$V_{STOR,OPT} = \frac{V_{OC,P}}{2(1-\eta_F)} \tag{4.7}$$

Equation (4.7) is calculated under the assumption that there is no voltage drop on AC/DC conversion stage and transistor M_P which constitutes an active diode together with comparator in Figure 4.1. If there exists voltage drop somewhere in the charging path, optimum storage voltage $V_{STOR,OPT}$ will be less than expression given in (4.7). If we put $V_{STOR,OPT}$ into equation (4.5), we get:

$$P_{NET,MAX} = \frac{f_{EX}C_{PZ}V_{OC,P}^2}{1-\eta_F} \tag{4.8}$$

Both equations (4.7) and (4.8) are consistent with ideal full bridge rectifier equations presented in chapter 2 where there is no voltage flipping and $n_F = 0$. All of calculations in this section are not only for SSHI systems. As long as synchronized switch harvesting (SSH) is the core method, it does not matter whether inductor (e.g. SSHI) or capacitor (e.g. SSHC) or both (e.g. SSHCI) are used for flipping purposes [66].

4.3. Second Generation SSHCI Circuit with Integrated MPPT

Figure 4.2 depicts the proposed energy harvesting system with required external components. It is composed of SSHCI circuit, a new MPPT system, and low-dropout (LDO) regulator. C_{PZ}, L_{EXT}, and C_{EXT} create LC resonance circuit to acquire two-step voltage flipping in which residual charge on PEH capacitance is inverted [73]. A cold start-up is also included in SSHCI enabling system to charge its load from 0 V. R_D and C_D are delay components that control shorting pulse duration of PEH capacitance in one of the operation phases. MPPT circuit uses the same external inductor as SSHCI thanks to inductor sharing. Capacitors C_{SENSE1} and C_{SENSE2} store piezoelectric open circuit voltage amplitude $V_{OC,P}$ in order to determine optimal storage voltage. C_{REFR} governs piezoelectric open circuit voltage sampling frequency to compensate for any leakage occur on C_{SENSE1} and C_{SENSE2}. R_{EXT1} and R_{EXT2} provides a fraction of storage voltage V_{STOR} that is needed to evaluate whether or not V_{STOR} is at optimum level. SSHCI circuit illustrated in Figure 4.3(a) contains ten sub-units. Main SSHCI (or SSHCI-Only) operation has five phases that are shown in Figure 4.3(b). If MPPT circuit is enabled, an extra phase occurs occasionally between phase IV and V to sense piezoelectric open circuit voltage. Operational details of core SSHCI circuit has been presented broadly throughout previous chapter (Chapter 3). Therefore, it will not be repeated here again. Figure 4.4(a) depicts MPPT circuit which tries to keep V_{STOR} voltage at its optimum value. To do so, it samples piezoelectric open circuit voltage amplitude $V_{OC,P}$ value every once in a while and compares it with a fraction of storage voltage V_{STOR} which is obtained with the help of resistors R_{EXT1} and R_{EXT2}.

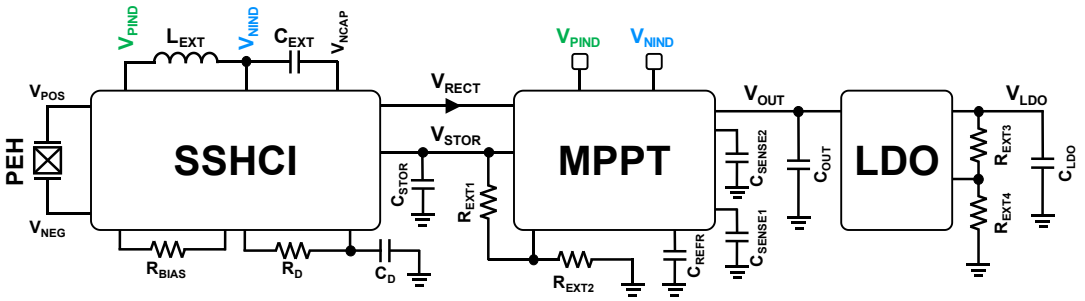

Figure 4.2. Proposed low-profile energy harvesting system.

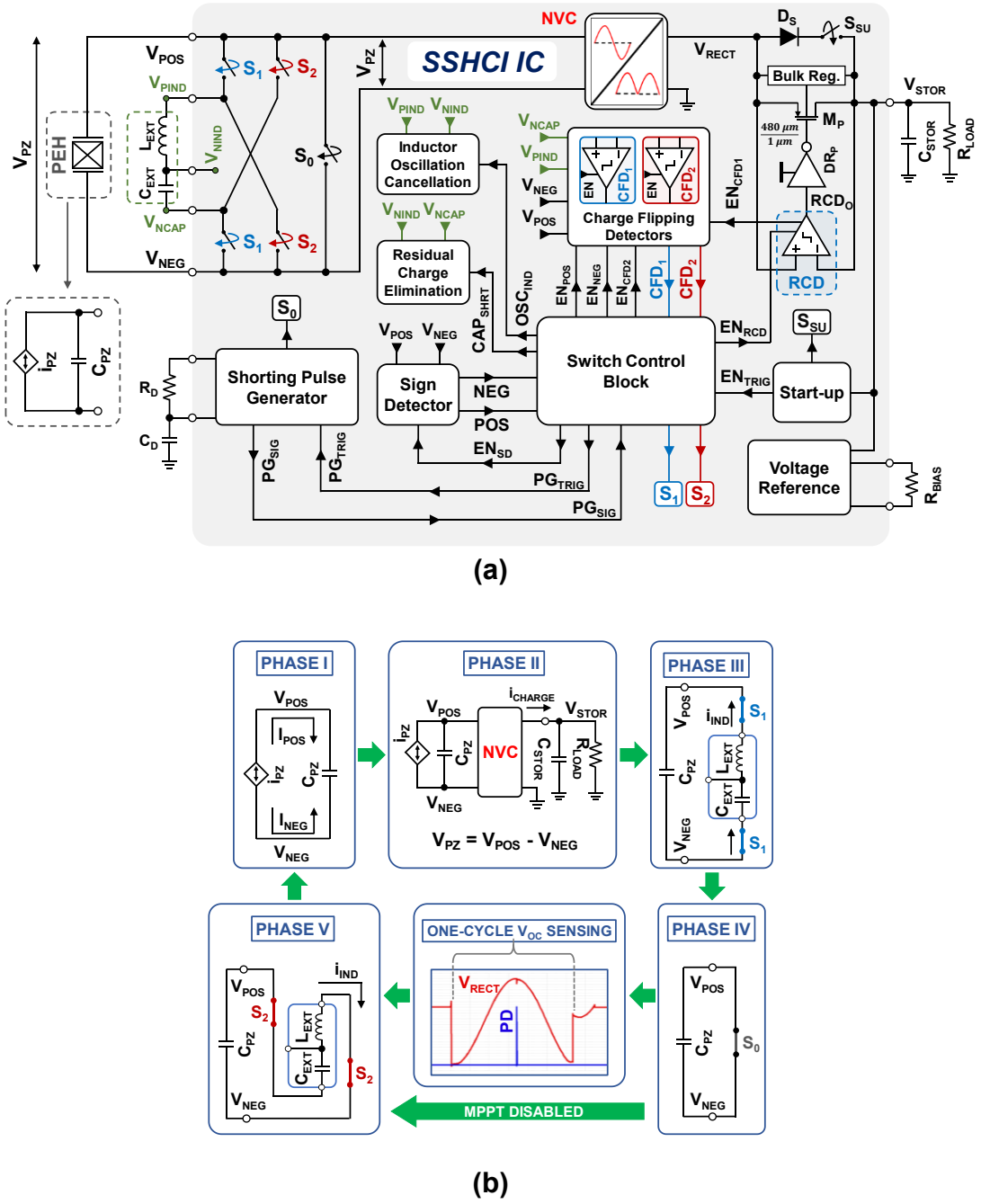

Figure 4.3. (a) Architecture of synchronized switch harvesting on capacitor-inductor (SSHCI) circuit and (b) summary of operation phases.

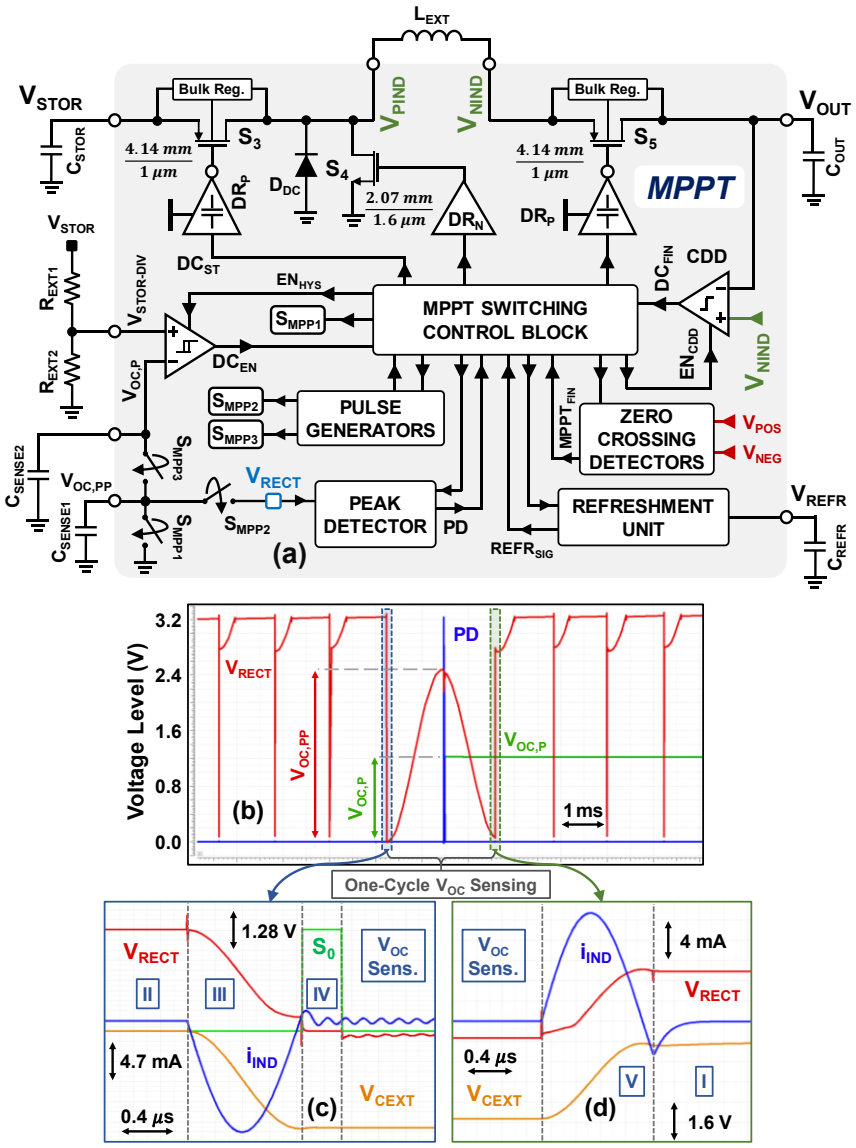

Figure 4.4. (a) Schematic of one-cycle $V_{OC,P}$ sensing MPPT circuit. Simulation waveforms of (b) one-cycle $V_{OC,P}$ sensing and SSHCI operation phases when sensing (c) starts and (d) ends. V_{RECT} is the rectified piezoelectric voltage, PD is the output of peak detector, $V_{OC,PP}$ is the peak-to-peak piezoelectric open circuit voltage, i_{ND} is the current passing through L_{EXT}, and V_{CEXT} is the voltage stored on external flipping capacitor C_{EXT}.

Simulation waveforms obtained during one-cycle $V_{OC,P}$ sensing are provided in Figure 4.4(b-d). One-cycle sensing starts when MPPT circuit is enabled via refreshment unit or external enable signal. However, one-cycle $V_{OC,P}$ does not start immediately in order not to disturb SSHCI phases and cause misleading $V_{OC,P}$ storage. Once phase

IV of SSHCI, in which C_{PZ} shorted after energy transfer to eliminate any residuals, finishes as shown in Figure 4.4(c), system lets PEH to accumulate charge on C_{PZ} with swinging of cantilever beam. The point that generated AC voltage on C_{PZ} reaches its maximum is caught by peak detector (PD). This maximum also corresponds to peak-to-peak piezoelectric open circuit voltage $V_{OC,PP}$. Thanks to switches S_{MPP1}, S_{MPP2}, and S_{MPP3} controlled by pulse generators, piezoelectric open circuit voltage amplitude $V_{OC,P}$ is stored on C_{SENSE2}. These three switches work in harmony as follows: At the end of SSHCI phase IV, both S_{MPP1} and S_{MPP3} turn ON to dispose of charges on sensing capacitors C_{SENSE1} and C_{SENSE2}. This process prepares C_{SENSE1} and C_{SENSE2} for the upcoming $V_{OC,P}$ storage. When peak detection signal comes, S_{MPP1} and S_{MPP3} turn OFF and S_{MPP2} turns ON to sample $V_{OC,PP}$ value onto C_{SENSE1}. After a short time, S_{MPP2} turns OFF while S_{MPP3} turns ON to share charges between C_{SENSE1} and C_{SENSE2}. Since $C_{SENSE1} = C_{SENSE2} = 33$ pF, charge is shared equally and $V_{OC,P}$ is stored on both of them. One-cycle $V_{OC,P}$ sensing process is finalized when V_{RECT} reaches zero. Zero crossing detector (ZCD) which generates $MPPT_{FIN}$ signal spots this moment and SSHCI operation continues from where it is left as given in Figure 4.4(d).

Following one-cycle $V_{OC,P}$ sensing, hysteresis comparator in Figure 4.4(a) is enabled which checks whether $V_{STOR,OPT}$ is reached. It lets V_{STOR} voltage to increase up to $V_{STOR,OPT}$ and if $V_{STOR} > V_{STOR,OPT}$, it triggers a DC/DC conversion through power switches S_3, S_4, and S_5. During that time, amount of charge which is transferred from C_{STOR} to C_{OUT} is determined by adjustable pulse generator similar to one proposed in [60]. This pulse generator inside MPPT switching control block directly governs how much time S_3 stays ON. Energy is delivered to C_{OUT} over L_{EXT}, S_3, and S_5. When pulse ends, S_3 turns OFF and S_4 starts operating which enable the system to extract residual energy on L_{EXT}. Charge depletion detector (CDD), which is a high-speed comparator, monitors terminals of switch S_5 and creates a signal to break charging path if V_{OUT} becomes larger than V_{NIND}. This finalizes one DC/DC conversion cycle and hysteresis comparator is enabled to observe V_{STOR} level. Figure 4.5 presents a simulation result summarizing output load charging and refreshment operations that

take place in MPPT. Refreshment unit provides signals to conduct one-cycle $V_{OC,P}$ storage occasionally. It facilitates proper MPPT operation via keeping $V_{OC,P}$ value on C_{SENSE2} fresh. Stored voltage might be degraded over time due to leakage, but refreshment unit prevents that. Moreover, it helps MPPT system to adapt if there exists any change on $V_{OC,P}$ level. Frequency of refreshment is contingent upon capacitance value of C_{REFR}.

4.4. Implementation of SSHCI-MPPT

SSHCI-MPPT system is a combination of well-designed sub-blocks which were presented in Figure 4.3(a) and 4.4(a). In this section, details of some critical circuit block designs will be revealed.

4.4.1. Second Generation Reverse Current Detector

For autonomous SSHCI operation, switch timing is controlled with a reverse current detector (RCD) and set of charge flipping detectors (CFDs). Hybrid 2-stage comparator topology in Figure 4.6 is utilized to sustain high performance operation across the output voltage range for detecting charging intervals. Common gate configuration which is made possible by transistors M_{11} and M_{12} increases detection sensitivity of the moment when V_+ starts to become less than V_-.

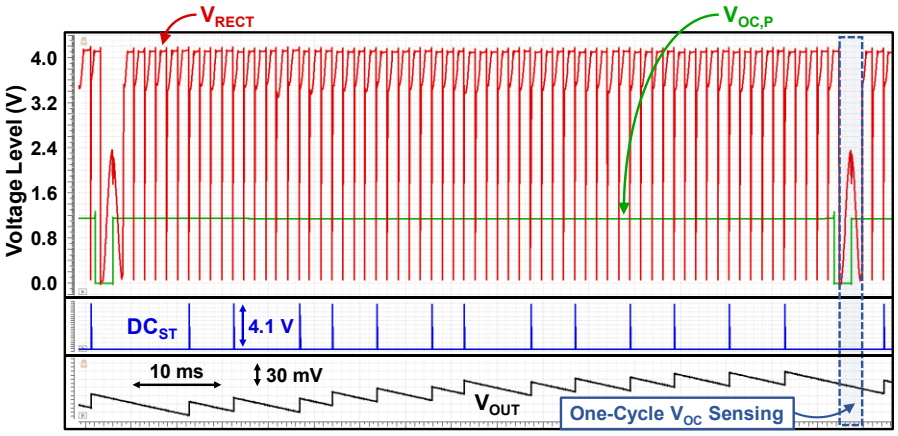

Figure 4.5. Simulation result of output load charging and refreshment operations that occur in MPPT. V_{RECT} is the rectified piezoelectric voltage, V_{OUT} the is output load voltage, $V_{OC,P}$ is the stored piezoelectric open circuit amplitude and DC_{ST} is the control signal of switch S_3.

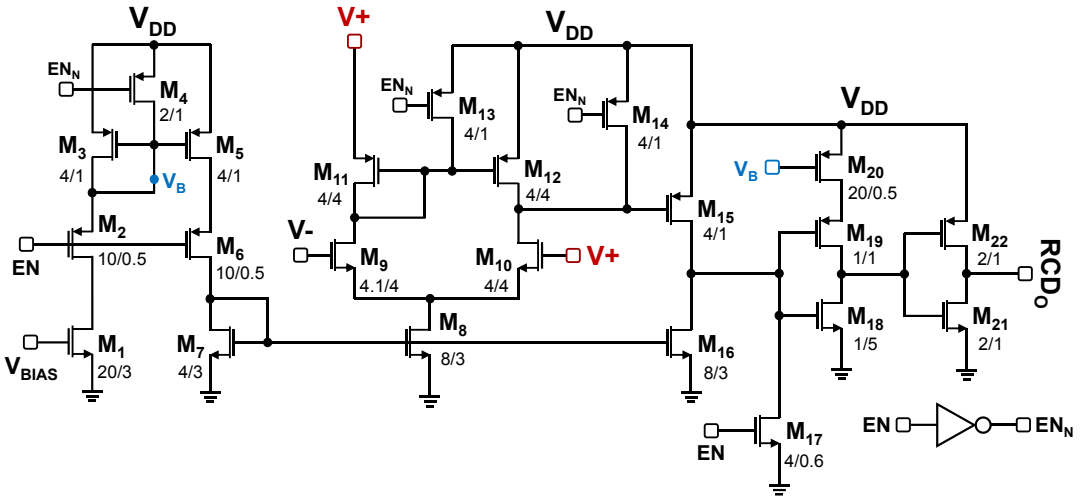

Figure 4.6. Implementation of second generation reverse current detector (RCD).

Since RCD is enabled during both phases I and II, its power dissipation has an utmost impact on system efficiency. Current limiting transistor M_{20} is included in the design to diminish current drawn from supply voltage while RCD is changing its output signal (i.e. detection moments).

4.4.2. Refreshment Unit

Due to leakages of transistors which are connected to $V_{OC,P}$ storing external capacitor C_{SENSE2}, saved $V_{OC,P}$ voltage level drops slowly. This leads to deviation regarding optimum storage voltage calculation in the circuit. To solve this issue, one-cycle $V_{OC,P}$ sensing refreshment unit depicted in Figure 4.7(a) is designed. After one-cycle $V_{OC,P}$ sensing, refreshment unit is enabled and mirrored biasing current which is around 15 nA begins to fill external capacitor C_{REFR}. When accumulated voltage V_{CREFR} arrives at around 700 mV, transistor M_7 starts turning ON and triggers detection signal generation. M_7, M_8, M_{10}, and M_{11} constitute two-stage common source amplifier to expedite detection and provide high edge rate. Figure 4.7(b) illustrates peak detection and one-cycle $V_{OC,P}$ sensing occur in MPPT with corresponding detection signals. Like RCD circuit, refreshment unit is nearly always ON which puts this unit to an important position in terms of system's power consumption.

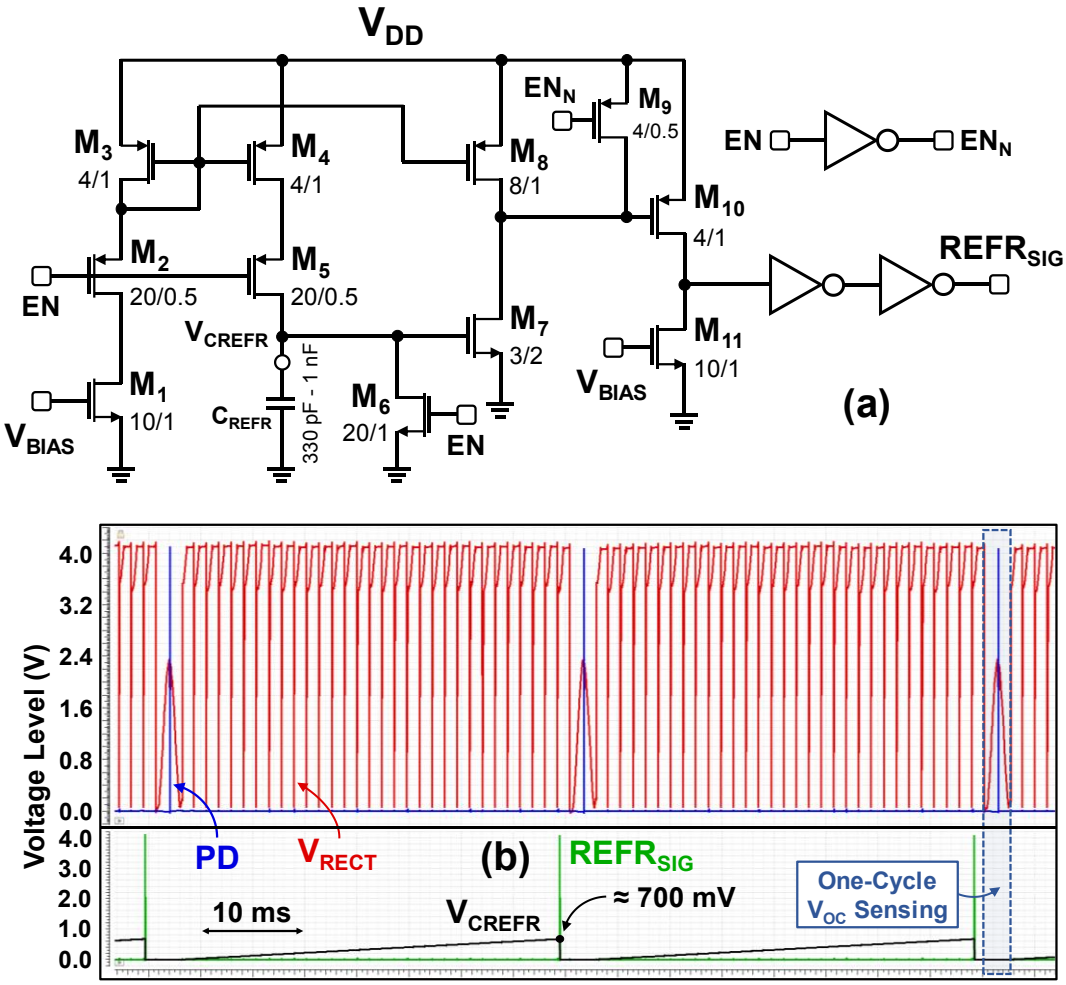

Figure 4.7. (a) Schematic of one-cycle $V_{OC,P}$ storage refreshment unit and (b) simulation waveforms of peak detector output (PD), refreshment triggering signal ($REFR_{SIG}$), voltage accumulated on external capacitance C_{REFR} (V_{CREFR}), and rectified piezoelectric voltage V_{RECT}.

4.4.3. Inductor Sharing Control Unit

Both SSHCI and MPPT circuits adopt the same external inductor L_{EXT} to accomplish proper operations and wipe out the need of another bulky inductor. Figure 4.8 presents control unit configuration which makes inductor sharing possible. Signals generated in both SSHCI and MPPT operations employed not to hamper any switching where usage of inductor is unavoidable. Control of external flipping capacitor C_{EXT} shorting signal which drives M_{CAP} is relatively easier than inductor sharing. Since C_{EXT} is included in flipping operation phases III and V only, it can be managed by RCD enable

signal. When RCD is working (EN_{RCD} is low), switch M_{CAP} shorts C_{EXT} terminals to get rid of any residual charge. During phases III, IV, and V, RCD is disabled and M_{CAP} is turned OFF which allows C_{EXT} to be charged and discharged and facilitate low-profile voltage flipping. C_{EXT} is shorted when it is not used.

In SSHCI-Only operation where MPPT is disabled (EN_{MPPT} is high), inductor oscillation cancellation signal OSC_{IND} is governed by RCD output RCD_O and adjustable C_{PZ} shorting pulse GND_{SIG} generated in phase IV. Charge flipping detection signals CFD_1 and CFD_2 established at the end of phases III and V turn M_{IND} ON in order to remove residual charges and prevent oscillation throughout phases I, II, and IV. In cases where MPPT is enabled either with an external signal EN_{EXT} or refreshment signal $REFR_{SIG}$, $CONT_P$ signal holds SSHCI circuit to enter phase V until one-cycle $V_{OC,P}$ sensing is finished. Other than that, DC/DC conversion in MPPT provided by switches S_3, S_4, and S_5 requests usage of inductor L_{EXT} when DC_{ST} signal is created as shown in Figure 4.5. DC/DC conversion is finished with DC_{FIN} signal which is produced by charge depletion detector (CDD). M_{IND} shorts L_{EXT} any other times not to encounter any oscillations.

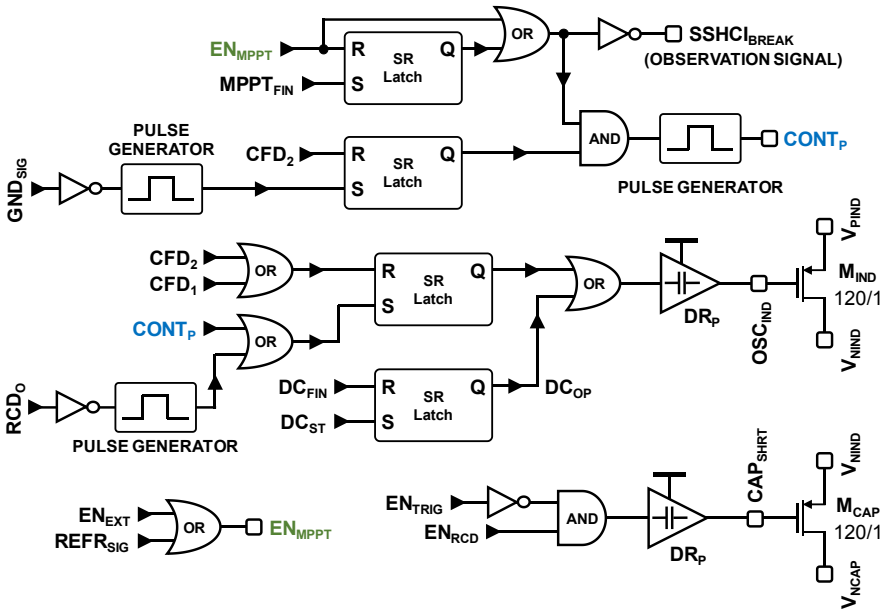

Figure 4.8. Control unit configuration of inductor sharing and external flipping capacitor shorting signal.

4.4.4. Peak Detector

The circuit used as peak detector in MPPT is originally proposed in [55] where details of the circuit are presented with relevant simulations. Figure 4.9 demonstrates the peak detector schematic. This circuit is able to detect wide-frequency voltage peaks. Since detector works in current mode, rectified piezoelectric voltage is transformed into current thanks to on-chip capacitor C_S. While V_{RECT} rises, node voltage V_A increases up to threshold voltage of M_3 due to negative feedback constructed by M_2 and M_3. Sensing current i_S becomes zero as V_{RECT} reaches its peak value. Then, transistor M_3 turns OFF due to decreased voltage on node V_A. This process disables negative feedback loop and a voltage starts to develop at node V_B owing to mirrored bias current. Common source amplifier constructed by transistors M_{10} and M_{11} along with inverters help generating the peak detection pulse.

4.4.5. Hysteresis Comparator

Hysteresis comparator presented in Figure 4.10(a) decides when charging of MPPT output load C_{OUT} starts. W/L ratios of transistors M_{13} (M_{15}) and M_{12} (M_{16}) controls hysteresis window width. Transistor M_{21} works as a current limiter which shrinks current drawn from supply voltage when circuit changes its state. Figure 4.10(b) illustrates simulation waveforms obtained during SSHCI-MPPT operation. Hysteresis comparator monitors the sample portion of storage voltage V_{STOR} and compares it $V_{OC,P}$ to check whether $V_{STOR,OPT}$ is reached.

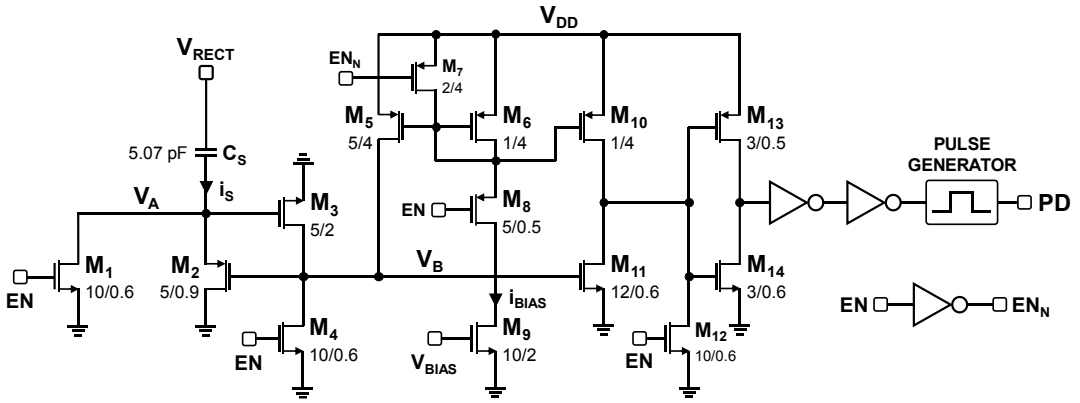

Figure 4.9. Peak detector schematic.

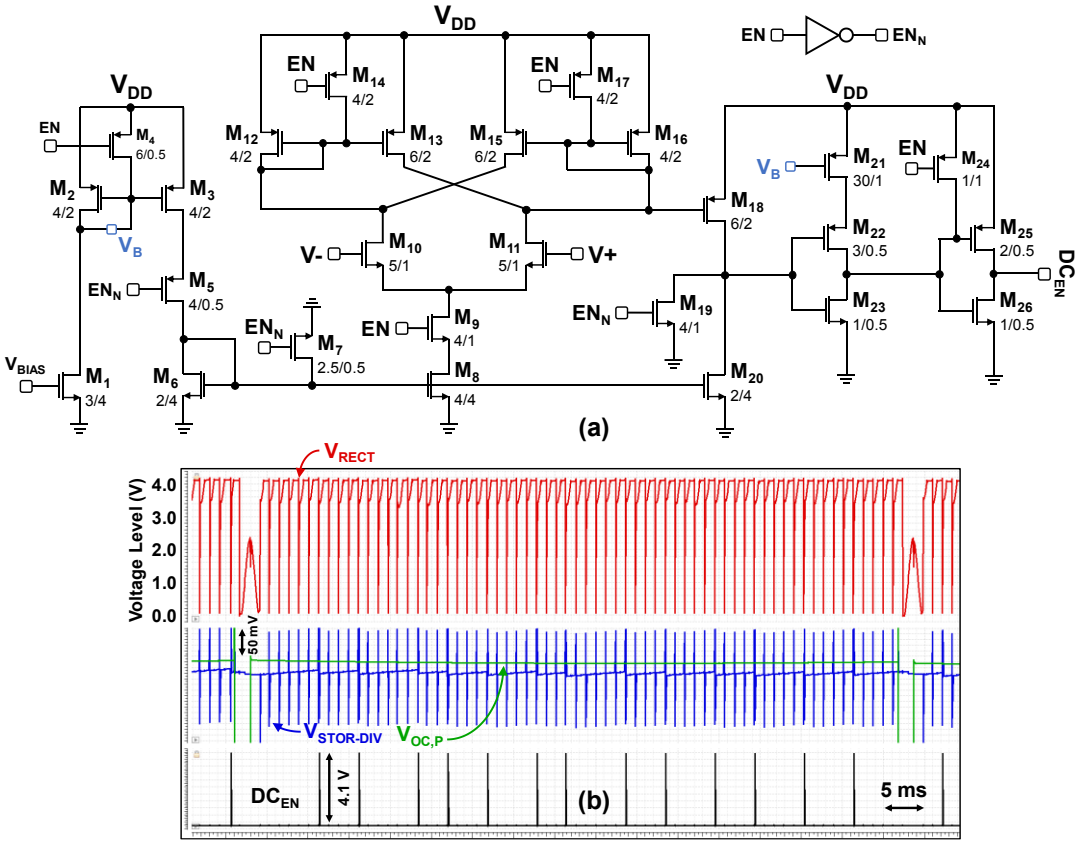

Figure 4.10. (a) Schematic of hysteresis comparator and (b) corresponding simulation result showing hysteresis comparator activity in SSHCI-MPPT. V_{RECT} is the rectified piezoelectric voltage, $V_{STOR\text{-}DIV}$ is the sample portion of storage voltage V_{STOR}, $V_{OC,P}$ is piezoelectric open circuit voltage amplitude, and DC_{EN} is the output of hysteresis comparator.

If optimum storage voltage $V_{STOR,OPT}$ is passed, it produces a signal called DC_{EN} to start DC/DC conversion operation inside MPPT. This comparator consumes as low as 60 nA current when it is enabled since it stays active throughout most of MPPT operation (it is disabled only during DC/DC conversion and one-cycle $V_{OC,P}$ sensing).

4.4.6. Zero Crossing Detection

One-cycle $V_{OC,P}$ sensing is finalized when a full cycle of PEH swing is finished. At that moment, one of PEH terminals V_{NEG} or V_{POS} reaches near zero voltage. To detect that moment, zero crossing detection (ZCD) configuration which consists of P-input comparators given in Figure 4.11 is used.

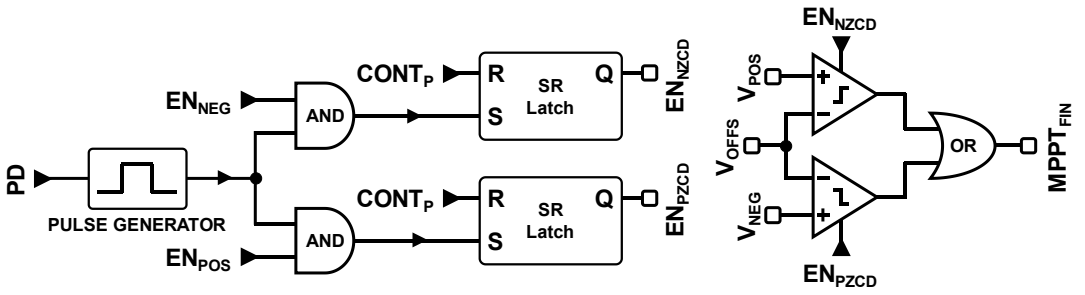

Figure 4.11. Zero crossing detection configuration for ending one-cycle $V_{OC,P}$ sensing phase.

After zero crossing detection, SSHCI operation continues with phase V as shown in Figure 4.4(d). One of the two P-input comparators is enabled depending on which cycle (positive or negative) PEH operates during one-cycle $V_{OC,P}$ sensing. Selected comparator that is enabled after peak detection monitors V_{NEG} (or V_{POS}) and offset voltage (V_{OFFS}). If V_{NEG} (or V_{POS}) gets closer to V_{OFFS} which is normally at ground level, $MPPT_{FIN}$ signal is created.

4.4.7. Adjustable Voltage Reference

Figure 4.12 depicts proposed voltage reference circuit which is a modified version of PTAT bias-current generator presented in [59]. Voltage on resistor R_{BIAS} is created due to gate-source voltage difference between M_1 and M_2. NMOS transistors M_3 and M_4 make sure that currents passing through M_1 and M_2 are equal at some biasing current level around 15 nA. This supply independent current is mirrored through M_5 and M_8 and then converted into reference voltage levels thanks to NMOS saturated load transistors M_6, M_7, and M_9. Transistors M_{S1}-M_{S5} and C_S serve as start-up configuration. Generated reference levels V_{REFH} and V_{REFL} can be tuned via R_{BIAS}.

4.4.8. Low-dropout Regulator

Figure 4.13 illustrates standard low-dropout voltage regulator which is used to provide stable and regulated output voltage. It is composed of a hysteresis comparator, driver, PMOS switch, voltage reference generator, and external resistors. The same comparator in section 4.4.5 and voltage reference in section 4.4.7 are employed. External resistors R_{EXT3} and R_{EXT4} govern V_{LDO} output voltage level.

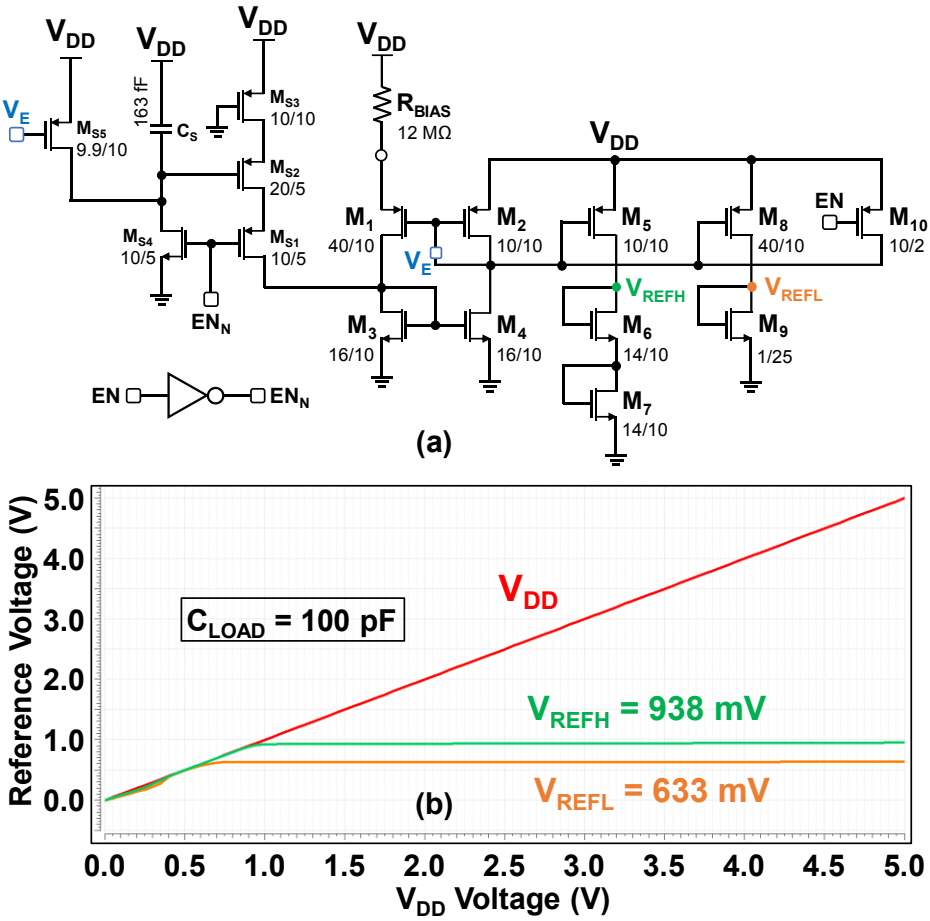

Figure 4.12. (a) Schematic of on-chip voltage reference circuit and (b) its corresponding simulation waveforms.

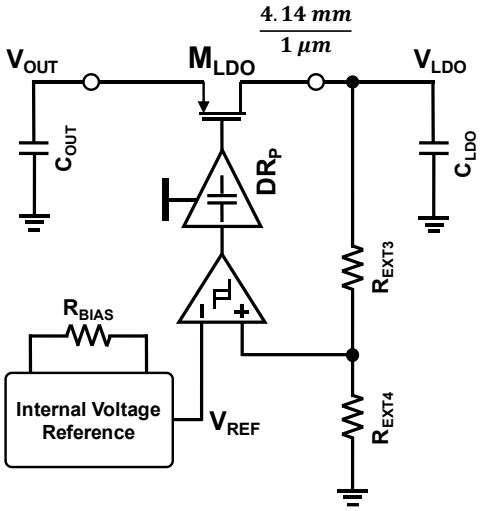

Figure 4.13. Schematic of low-dropout voltage regulator.

4.5. Experimental Results

SSHCI-MPPT circuit is fabricated with 180 nm CMOS technology. Die micrograph of the fabricated chip is depicted in Figure 4.14. It occupies 1400 µm x 880 µm active area without on-chip voltage reference and low-dropout regulator. Experimental setup used to evaluate performance of fabricated SSHCI-MPPT chip is İllustrated in Figure 4.15. Block diagram of the experimental setup was the same as Figure 3.19 where SSHCI-MPPT chip was under investigation instead of SSHCI IC. A custom MEMS PEH with a footprint of 36 mm^2 has been placed onto a shaker table to power up a 453 nF storage capacitor C_{STOR} through interface circuit operation. It has inherent capacitance C_{PZ} of 2 nF and 415 Hz resonance frequency. Vibration setup including shaker table, amplifier, controller, and vibration software excited PEH at its resonance frequency. 68 and 100 µH SMD inductors were utilized as L_{EXT} along with $C_{EXT} = C_{PZ}$ = 2 nF to implement voltage flipping and DC/DC conversion operations in SSHCI-MPPT circuit. Compared to the first generation SSHCI circuit, slightly large valued external inductor (68-100 µH) were employed in order to boost voltage flipping efficiency and compensate enlarged power dissipation of new RCD circuit and energy loss caused by increased number of switching mechanism.

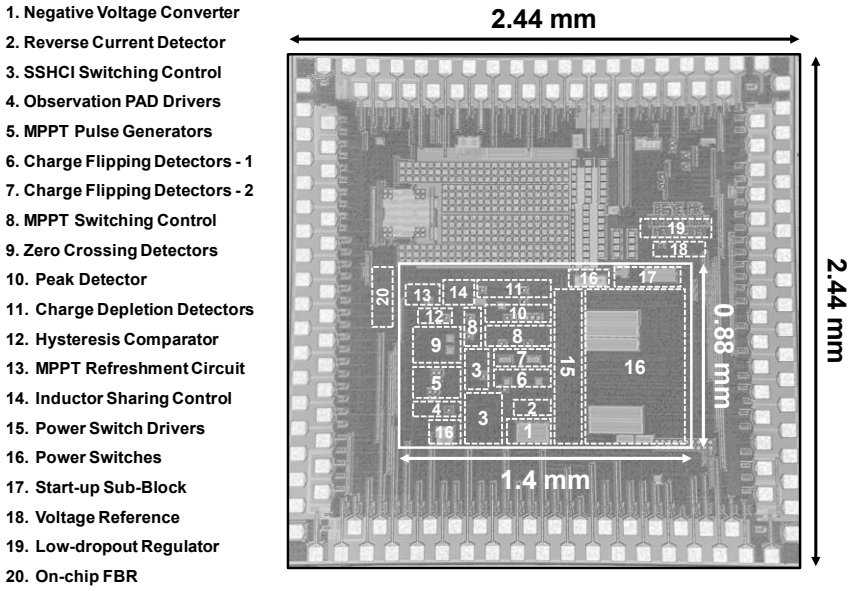

Figure 4.14. Die micrograph of SSHCI-MPPT chip fabricated with 180 nm CMOS technology.

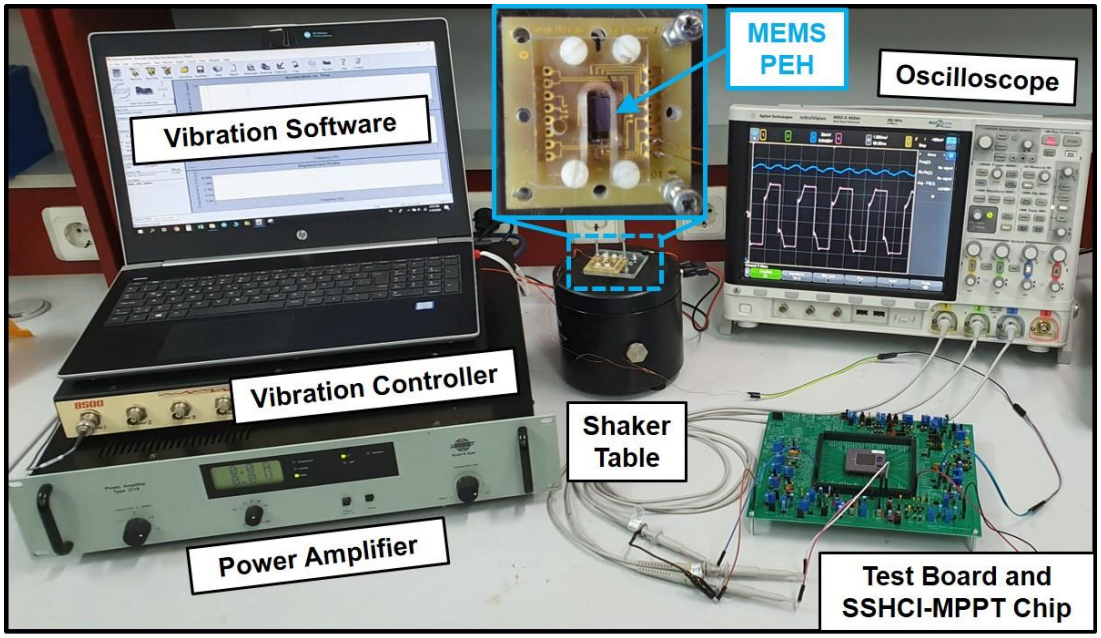

Figure 4.15. Experimental setup for SSHCI-MPPT design validation.

Figure 16(a) shows measured start-up operation which is made possible by NVC, on-chip diode D_S and switch S_{SU}. V_{STOR} level which is sufficient to activate SSHCI operation is determined by start-up trigger circuit. Required V_{STOR} can be as low as 1.1 V; however, start-up trigger circuit was adjusted to generate signal around 1.4 V to let SSHCI work safely. Figure 16(b) presents measured SSHCI charging operation whereas Figure 16(c) depicts details of voltage flipping phases. SSHCI circuit does not require any external adjustment to accomplish storage capacitor charging and optimal charge flipping. It is able to operate with low-profile external inductors and still, it manages to provide flipping efficiencies comparable with conventional SSHI circuits [33], [48], [72]. Figure 4.17 illustrates measured waveforms of rectified piezoelectric voltage V_{RECT}, storage voltage V_{STOR} at the output of SSHCI stage, and load voltage V_{OUT} which is the output of MPPT circuit. As it can be seen from the figure, MPPT operation is working seamlessly with SSHCI and keep V_{STOR} around 2.26 V for piezoelectric open circuit amplitude $V_{OC,P}$ = 0.81 V. Furthermore, two consecutive $V_{OC,P}$ sensing operation and charging of output capacitance C_{OUT} = 1 µF have taken place in the same figure.

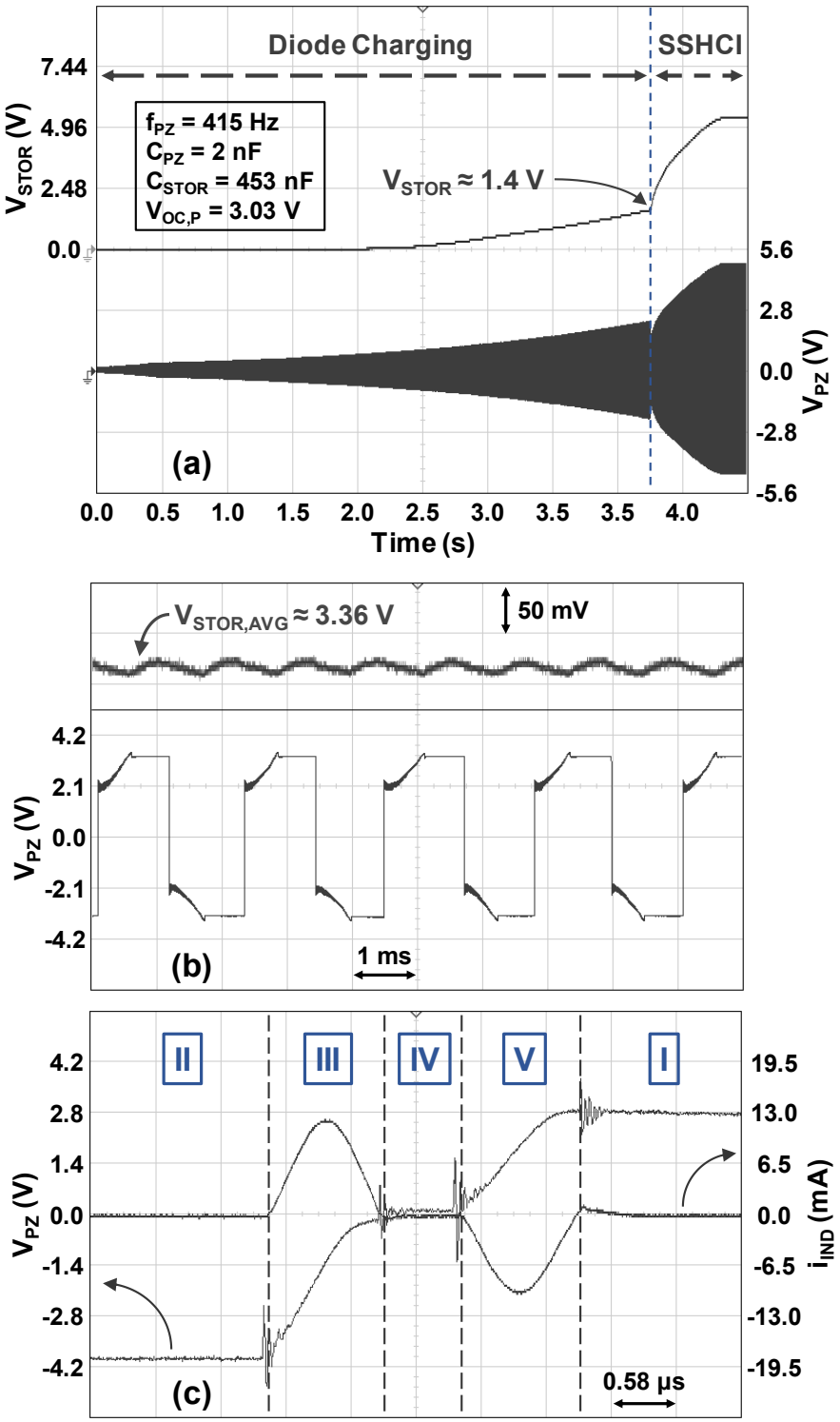

Figure 4.16. Measured waveforms of piezoelectric voltage V_{PZ}, storage voltage V_{STOR}, and inductor current i_{PZ} demonstrating (a) start-up, (b) C_{STOR} charging, and (c) two-stage voltage flipping operation in SSHCI circuit.

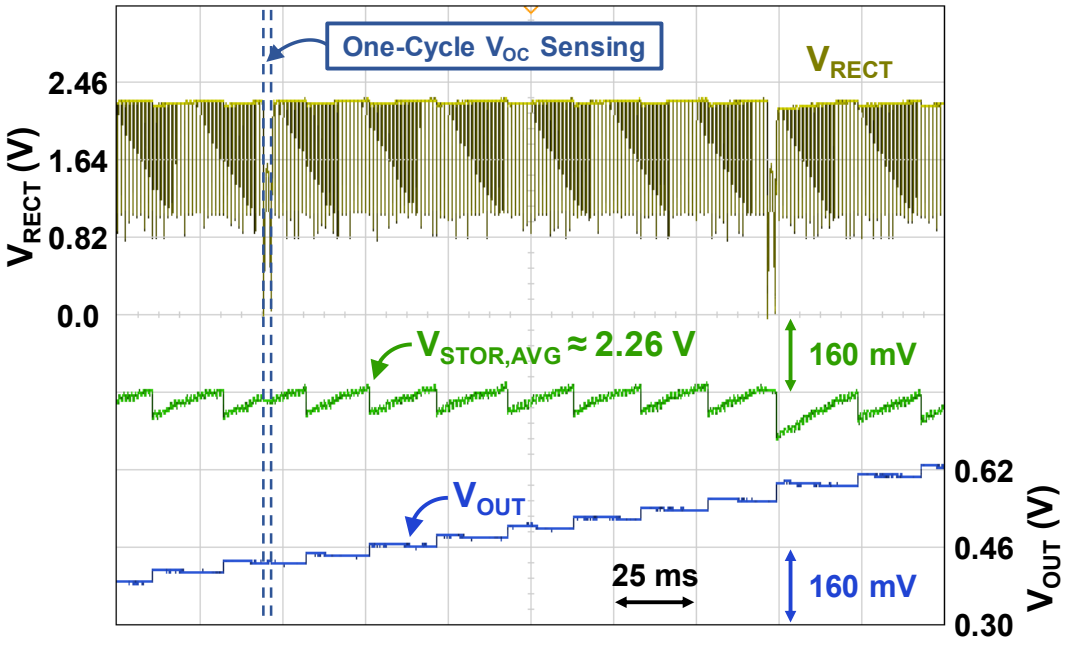

Figure 4.17. Measured waveforms of V_{RECT}, V_{STOR}, and V_{OUT} during MPPT charging operation.

Figure 4.18(a) presents multiple $V_{OC,P}$ sensing refreshments which were realized by shrinking capacitor C_{REFR} to achieve multiple $REFR_{SIG}$ control signal depicted in Figure 4.7(b). When $REFR_{SIG}$ is developed during system activity, it causes SSHCI operation to suspend after phase IV to let one-cycle $V_{OC,P}$ sensing occur. $SSHCI_{BREAK}$ in Figure 4.18(a) represents SSHCI suspension signal triggered by $REFR_{SIG}$. After one-cycle $V_{OC,P}$ sensing is finished, it goes to low and SSHCI continues its operation with second flipping in phase V. Figure 4.18(b) depicts inductor sharing. SSHCI-MPPT system is capable of utilizing same external inductor L_{EXT} to attain both voltage flipping and DC/DC conversion. Adjustable pulse generators inside MPPT switching control block in Figure 4.4 governs how long switch S_3 is ON and determines how much current is passing through inductor at DC/DC conversion. Figure 4.19(a, b) depicts measured output power of SSHCI operation under different excitation levels. At $V_{OC,P} = 1.02$ V excitation, SSHCI was able to attain 5.44 times relative performance improvement over harvested power of an ideal full bridge rectifier (FBR). As excitation level was enlarged, relative performance enhancement decreased owing to larger damping of PEH and increased conduction and switching losses.

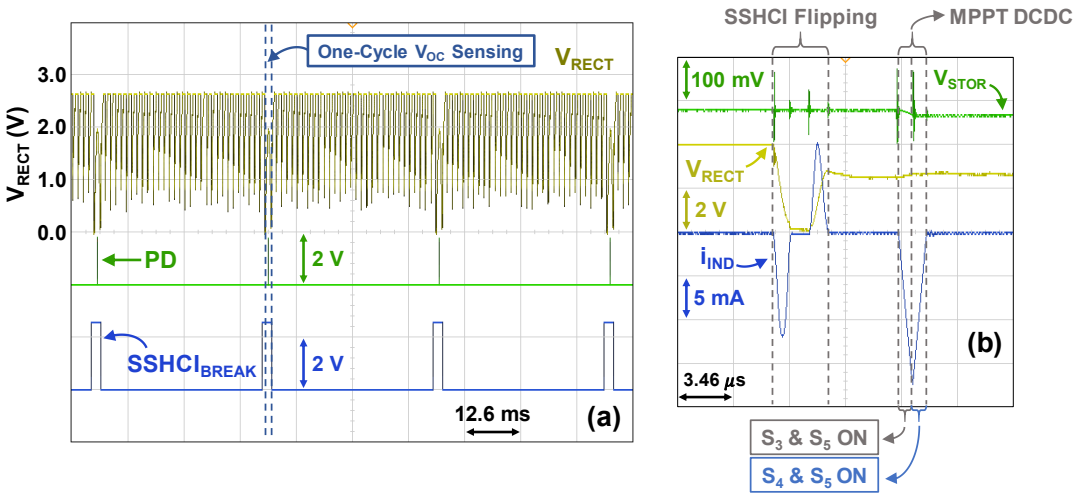

Figure 4.18. Measured waveforms of V_{RECT}, V_{STOR}, V_{OUT}, i_{IND}, and control signals PD and $SSHCI_{BREAK}$ during (a) multiple one-cycle $V_{OC,P}$ sensing refreshment and (b) inductor sharing.

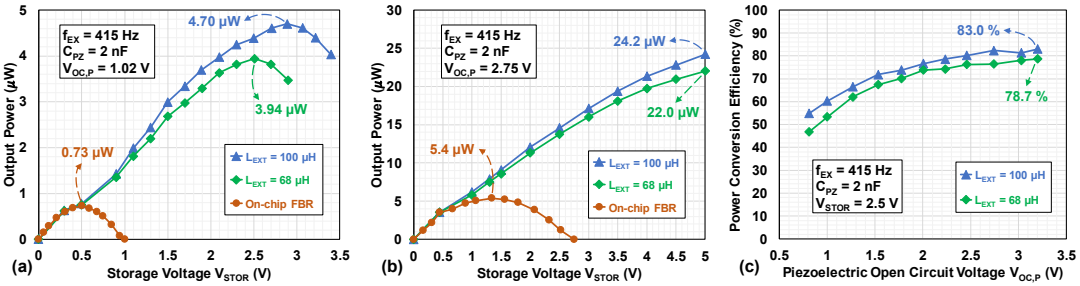

Figure 4.19. Measured output power of SSHCI circuit for piezoelectric open circuit voltage amplitudes (a) $V_{OC,P}$ = 1.02 V, (b) $V_{OC,P}$ = 2.75 V, and (c) power conversion efficiency of SSHCI operation.

As given in Figure 4.19(c), maximum power conversion efficiency ($\eta = P_{SSHCI}/P_{IN}$) of 83% (P_{IN} = 27.37 µW) was recorded which makes SSHCI technique superior among other low-profile circuits [67], [66], [70]. Most of energy consumption is caused by RCD circuit which continues to operate during phases I and II.

Figure 4.20 illustrates measured harvested power levels at optimum storage voltages $V_{STOR,OPT}$ and corresponding Figure-of-Merit (FOM) values of both core SSHCI and SSHCI-MPPT operations for different PEH excitation levels (L_{EXT} = 100 µH).

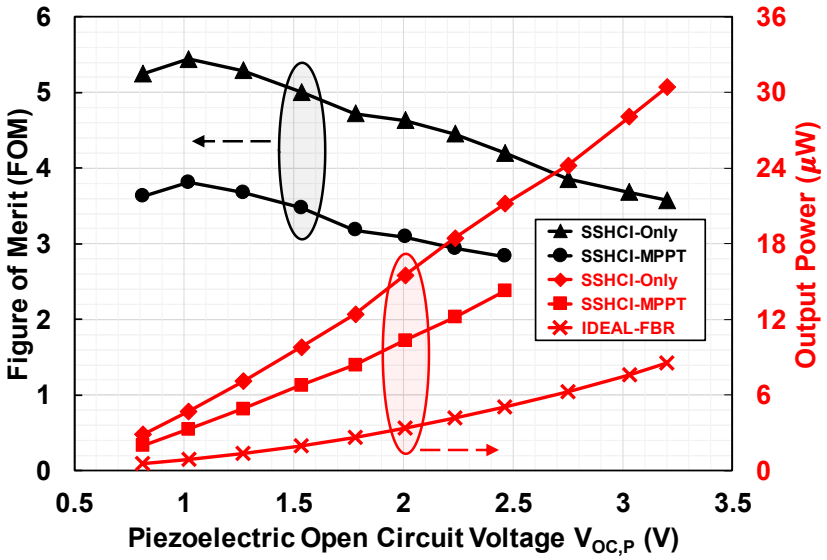

Figure 4.20. Measured harvested power of SSHCI and MPPT circuits compared to ideal FBR at different piezoelectric open circuit voltage amplitudes ($V_{OC,P}$).

FOM describes how much improvement is obtained over ideal FBR:

$$FOM = \frac{P_{OUT}}{P_{IDEAL-FBR}} = \frac{P_{OUT}}{f_{EX} C_{PZ} V_{OC,P}^2} \tag{4.9}$$

SSHCI operation provides 5.44 maximum FOM while utilizing 100 µH external inductor which occupies 18 mm^3. This FOM is the result of weak electromechanical coupling of MEMS PEH which affects performance of FBR harshly. When MPPT is enabled, maximum FOM drops to 3.81 due to elevated power consumption coming from MPPT sub-circuits. This power consumption mainly corresponds to switching losses in DC/DC conversion, energy dissipations of pulse generators inside MPPT switching control unit and switch drivers. Both SSHCI-Only and SSHCI-MPPT modes performed better at low excitation levels where nonlinear switching technique handles damping force well [74].

4.6. Discussion

Table 4.1 introduces a performance comparison of fabricated chips against state-of-the-art PEH interface circuits. In terms of autonomy, SSHCI circuit distinguishes from others which require some kind of external adjustment.

Table 4.1. *Comparison of implemented SSHCI-MPPT with state-of-the-art.*

Ref.	[59]	[54]	[72]	[65]	[70]	[66]	[80]	**This Work**
Tech.	350 nm	320 nm	350 nm	130 nm	180 nm	180 nm	350 nm	**180 nm**
Chip Size	2.34 mm^2	0.95 mm^2	1.17 mm^2	1.07 mm^2	1.70 mm^2	3.90 mm^2	5.52 mm^2	**1.23 mm^2**
C_{PZ}	15 nF	52 nF	9 nF	20 nF 100 nF	80 pF	1.94 nF	11 nF	**2 nF**
Excitation Frequency	143 Hz	60 Hz	229 Hz	100 Hz 180 Hz	110 kHz	219 Hz	NA	**415 Hz**
Inductor (Volume)	330 µH (126 mm^3)	10 mH (NA)	3.3 mH (15.2 mm^3)	3.3 mH (NA)	NO	NO	10 mH (NA)	**68-100 µH (18 mm^2)**
Flipping Time Detection	NA	NA	External Adj.	External Adj.	External Adj.	External Adj.	NA	**Autonomous Adj.**
Cold Start-up	NO	YES	YES	YES	YES	NO	YES	**YES**
MPPT	NO	NO	YES	YES	NO	NO	YES	**YES**
Peak Conversion Efficiency	69.2%	85.3(2)%	NA	78(3)%	NA	NA	80(3)%	**83% (100 µH) 78.7% (68 µH)**
Power Extraction Gain	360%	351%	440%	417%	483(4)%	606(5)%	97%	**544% (100 µH) 456% (68 µH)**
FOM(1)x100								

(1) FOM = $P_{OUT}/f_{EX}V_{OC,P}^2C_{PZ}$
(2) External supply was used.
(3) It is only for DC/DC converter.
(4) Calculated with respect to on-chip FBR.
(5) Calculated from paper.

Conventional methods may create inconvenience in some biomedical applications demanding fully integrated and autonomous system operation. SECE circuits in [54], [59] suffer from relatively small FOM values. Sanchez [72] employed a large external inductor to realize a conventional SSHI interface that can extract energy from both periodic and shock excitations. Although this circuit acquired decent output powers and externally controlled MPPT, aim of miniaturized harvesting system is far beyond to reach. Recently, Li [65] proposed perturb and observe (P & O) method integrated with SSHI circuit which senses output power continually to find optimum level.

External inductor is shared between SSHI and MPPT blocks as in our system; however, SSHCI provides larger FOM and efficiency while utilizing low-profile components. Inductorless designs in [66], [70] uses on-chip capacitors for flipping which is a huge step towards miniaturization. They present FOM values better than traditional SSHI circuit. Nonetheless, synchronized switch harvesting (SSH) technique is the nature of both inductorless architectures that makes them strongly load dependent. Like SSHCI-MPPT, Shim [80] benefits from half open circuit voltage sensing to detect optimum battery voltage. Yet, active rectifier (AR) is the AC/DC mechanism that harvesting circuit relies on and this leads to small FOM. SSHCI circuit provides a basis to realize low-profile and autonomous energy harvesting systems thanks to its novel two-step voltage flipping mechanism and optimum charge transfer detection. Compared to our previous work in [73], power extraction improvement and power conversion efficiency values go worse due to increased power dissipation of second generation RCD design and energy loss coming from increased number of switching mechanisms. However, new MPPT architecture eliminates load dependency and increase robustness in exchange for reduction in FOM. Small inductance utilized in this system does not prevent SSHCI circuit to obtain power extraction improvement and efficiency superior to conventional SECE and SSHI methods.

CHAPTER 5

CONCLUSION AND FUTURE WORK

In the scope of this thesis, a fully autonomous self-powered piezoelectric energy harvesting interface circuit composed of low-profile external components and integrated maximum power point tracking (MPPT) system have been developed and implemented. Designs presented in this study paves the way for miniaturization in energy harvesting systems and broadens application area of energy scavenging concept. Cochlear implants (CIs) are one of the biomedical devices that can benefit from low-profile energy harvesting systems to eliminate bulk batteries they need for operation. It is conceptually possible to supply some amount of or whole energy that CIs demand through energy harvesting provided that MEMS PEH is capable of scavenging 100s of μWs. Explanation of the proposed novel nonlinear switching technique SSHCI, detailed circuit designs, and theoretical optimum battery voltage calculations were established in previous chapters. Fabricated ICs have been tested with MEMS based piezoelectric energy harvesters to validate their functionality. Performance values of implemented ICs have been compared with state-of-the-art interface circuits to see their places in piezoelectric energy harvesting literature. This chapter presents major accomplishments obtained during this research and future works that can be done to improve current low-profile design.

5.1. Major Accomplishments

The first generation SSHCI circuit is implemented to improve extracted energy from PEH and power conversion efficiency while utilizing low-profile (small-volume) external components. Major accomplishments earned with this design can be described as follows:

- The novel two-step voltage flipping proposed with SSHCI helps reducing external component sizes while showing performances comparable to the ones

using bulky inductors. This offers a huge step towards miniaturized harvesting system since inductors account for most of the space that system occupies.

- SSHCI is able to detect optimal charge flipping detection times thanks to its built-in detectors. This eliminates the need for external adjustment that nearly every other interface circuit requires and autonomy in SSHCI operation is secured with charge flipping detectors and reverse current monitoring.
- Cold start-up structure inside SSHCI facilitates storage capacitor changing even if it is completely depleted. Sub-threshold design of RCD allows it to begin its operation early which accelerates start-up process.
- Fabricated ICs achieve a maximum of 90.1% power conversion efficiency as a result of low-power design techniques that were applied.
- Compared to conventional SECE and SSHI techniques and recent inductorless designs, SSHCI provides higher output power improvement at low excitation levels.

The second generation piezoelectric energy harvesting interface circuit is designed and implemented to get rid of load dependency that SSHCI circuit inherently has. Below, major achievements that are attained with SSHCI-MPPT IC are listed:

- Theoretical optimum storage (or battery) voltage has been calculated which created a foundation towards MPPT design. This optimum voltage is also valid for SSHI and SSHC techniques that utilize low coupled PEHs to power up their systems.
- MPPT circuit that works seamlessly with SSHCI provides load independency.
- Inductor sharing reduces number of external components that SSHCI-MPPT circuit need for proper operation. Same low-profile external inductor is employed for both charge flipping operation in SSHCI and for DC/DC conversion in MPPT.
- Refreshment unit assures that optimum output power is preserved and therefore, it makes MPPT system invulnerable to input excitation level changes.

- SSHCI-MPPT presents 5.44x output power improvement over ideal FBR. MPPT operation curtails this improvement in exchange for enhanced system robustness. SSHCI-MPPT is one of a kind PEH interfacing architecture in the literature which has both minimum number of external components with low-cost sizes and dedicated MPPT circuit.

5.2. Future Work

Even if novel SSHCI and SSHCI-MPPT circuits contribute to the PEH interface circuit literature in terms of output power enhancement and miniaturization, there exist some improvements that can be done to boost their specifications:

- SSHCI based circuits require an external capacitance value equals to PEH intrinsic capacitor. This increases system volume. It can be excluded if an enhanced SSHI (E-SSHI) based circuit with low-cost inductor is developed. Optimal charge flipping detection introduced in this thesis might be the starting point of the new E-SSHI method. Moreover, reducing number external components may ease system integration in space limited biomedical devices such as cochlear implants (CIs).
- Power consumptions inside MPPT circuits can be optimized. SSHCI-MPPT output power is affected by relatively high energy consumptions of pulse generators and switch drivers inside MPPT. Furthermore, number of switches that makes DC/DC conversion and one-cycle $V_{OC,P}$ sensing possible may be decreased. This may also help easing MPPT complexity.
- Instead of using only one energy source (or harvester) as an input, multiple sources (both vibration based and others) might be utilized to extract more energy and deliver more output power. It can be possible with a hybrid energy harvesting system that can harvest energy from a wide frequency range and various sources available in environment. This will enhance system reliability. With hybrid energy harvesting from various environmental energy sources, it is possible to provide almost complete amount of energy that CIs dissipate.

REFERENCES

[1] C. Azcona, B. Calvo, N. Medrano, and S. Celma, "1.2 V-0.18-µm CMOS Temperature Sensors with Quasi-Digital Output for Portable Systems," *IEEE Trans. Instrum. Meas.*, vol. 64, no. 9, pp. 2565–2573, 2015.

[2] Z. Tan, R. Daamen, A. Humbert, Y. V. Ponomarev, Y. Chae, and M. A. P. Pertijs, "A 1.2-V 8.3-nJ CMOS humidity sensor for RFID applications," *IEEE J. Solid-State Circuits*, vol. 48, no. 10, pp. 2469–2477, 2013.

[3] K. Ueno, T. Asai, and Y. Amemiya, "Low-power temperature-to-frequency converter consisting of subthreshold CMOS circuits for integrated smart temperature sensors," *Sensors Actuators, A Phys.*, vol. 165, no. 1, pp. 132–137, 2011.

[4] S. Oh, W. Jung, K. Yang, D. Blaauw, and D. Sylvester, "15.4b incremental sigma-delta capacitance-to-digital converter with zoom-in 9b asynchronous SAR," *IEEE Symp. VLSI Circuits, Dig. Tech. Pap.*, pp. 2013–2014, 2014.

[5] C. Brandon, D. Elliott, and K. Moez, "An Ultra Low-Voltage Low-Power Capacitance-to-Digital Converter for Wirelessly Powered Intraocular Pressure Sensor," *IEEE J. Radio Freq. Identif.*, vol. 1, no. 3, pp. 208–218, 2018.

[6] S. Oh *et al.*, "A dual-slope capacitance-to-digital converter integrated in an implantable pressure-sensing system," *IEEE J. Solid-State Circuits*, vol. 50, no. 7, pp. 1581–1591, 2015.

[7] M. Sasaki, M. Ikeda, and K. Asada, "A Temperature Sensor With an Inaccuracy of -1/+0.8°C Using 90-nm 1-V CMOS for Online Thermal Monitoring of VLSI Circuits," *IEEE Trans. Semicond. Manuf.*, vol. 21, no. 2, pp. 201–208, 2008.

[8] P. D. Mitcheson, E. M. Yeatman, G. K. Rao, A. S. Holmes, and T. C. Green, "Energy Harvesting From Human and Machine Motion for Wireless Electronic Devices," *Proc. IEEE*, vol. 96, no. 9, pp. 1457–1486, 2008.

[9] R. J. M. Vullers, R. Schaijk, H. Visser, J. Penders, and C. Hoof, "Energy Harvesting for Autonomous Wireless Sensor Networks," *IEEE Solid-State Circuits Mag.*, vol. 2, no. 2, pp. 29–38, 2010.

[10] T. Galchev, J. McCullagh, R. L. Peterson, K. Najafi, and A. Mortazawi, "Energy harvesting of radio frequency and vibration energy to enable wireless

sensor monitoring of civil infrastructure," *Proc. SPIE*, 2011.

[11] R. F. Yazicloglu, P. Merken, R. Puers, and C. Van Hoof, "A 60μW 60 nV/√Hz readout front-end for portable biopotential acquisition systems," *Dig. Tech. Pap. - IEEE Int. Solid-State Circuits Conf.*, pp. 109–118, 2006.

[12] A. Koyuncuoğlu *et al.*, "Bulk PZT Cantilever Based MEMS Acoustic Transducer for Cochlear Implant Applications," in *Proceedings of Eurosensors 2017*, 2017, vol. 1, no. 10, p. 584.

[13] F. G. Zeng, S. Rebscher, W. Harrison, X. Sun, and H. Feng, "Cochlear Implants: System Design, Integration, and Evaluation," *IEEE Rev. Biomed. Eng.*, vol. 1, no. dc, pp. 115–142, 2008.

[14] M. Yip, R. Jin, H. H. Nakajima, K. M. Stankovic, and A. P. Chandrakasan, "A fully-implantable cochlear implant SoC with piezoelectric middle-ear sensor and arbitrary waveform neural stimulation," *IEEE J. Solid-State Circuits*, vol. 50, no. 1, pp. 214–229, 2015.

[15] H. Ulusan, A. Muhtaroglu, and H. Kulah, "A Sub-500 μ W Interface Electronics for Bionic Ears," *IEEE Access*, vol. 7, pp. 132140–132152, 2019.

[16] F. G. Dell'Anna *et al.*, "State-of-the-Art Power Management Circuits for Piezoelectric Energy Harvesters," *IEEE Circuits Syst. Mag.*, vol. 18, no. 3, pp. 27–48, 2018.

[17] X. H. Dong and X. D. Huang, "A Non-Resonant Type Electromagnetic Energy Harvester for Scavenging Vibration Energy," *Proc. IEEE Sensors*, vol. 2018–Octob, pp. 1–3, 2018.

[18] G. Verma and V. Sharma, "A Novel Thermoelectric Energy Harvester for Wireless Sensor Network Application," *IEEE Trans. Ind. Electron.*, vol. 66, no. 5, pp. 3530–3538, 2019.

[19] V. Leonov *et al.*, "Wearable self-powered wireless devices with thermoelectric energy scavengers," *Smart Syst. Integr. 2008 - 2nd Eur. Conf. Exhib. Integr. Issues Miniaturized Syst. MEMS, MOEMS, ICs Electron. Components*, 2008.

[20] T. Torfs, V. Leonov, and R. J. M. Vullers, "Pulse Oximeter Fully Powered by Human Body Heat," *Senosors Transducers J.*, vol. 80, no. 6, pp. 1230–1238, 2007.

[21] T. Hehn and Y. Manoli, *CMOS Circuits for Piezoelectric Energy Harvesters -*

Efficient Power Extraction, Interface Modeling and Loss Analysis, vol. 38. 2015.

[22] I. Mathews, P. J. King, F. Stafford, and R. Frizzell, "Performance of III-V solar cells as indoor light energy harvesters," *IEEE J. Photovoltaics*, vol. 6, no. 1, pp. 230–235, 2016.

[23] A. Othman and D. Maga, "Indoor Photovoltaic Energy Harvester with Rechargeable Battery for Wireless Sensor Node," *Proc. 2018 18th Int. Conf. Mechatronics - Mechatronika*, pp. 1–6, 2019.

[24] T. Ungan and L. M. Reindl, "Harvesting Low Ambient RF-Sources for Autonomous Measurement Systems," in *IEEE International Instrumentation and Measurement Technology Conference*, 2008.

[25] S. Scorcioni, L. Larcher, A. Bertacchini, L. Vincetti, and M. Maini, "An integrated RF energy harvester for UHF wireless powering applications," in *2013 IEEE Wireless Power Transfer (WPT)*, 2013, pp. 92–95.

[26] D. Hoffmann, B. Folkmer, and Y. Manoli, "Fabrication, characterization and modelling of electrostatic micro-generators," *J. Micromechanics Microengineering*, vol. 19, no. 9, 2009.

[27] Y. Zhang, A. Luo, Y. Xu, T. Wang, and F. Wang, "Wideband MEMS electrostatic energy harvester with dual resonant structure," *Proc. IEEE Sensors*, pp. 1–3, 2017.

[28] S. P. Beeby *et al.*, "A micro electromagnetic generator for vibration energy harvesting," *J. Micromechanics Microengineering*, vol. 17, no. 7, pp. 1257–1265, 2007.

[29] S. Roundy *et al.*, "Improving power output for vibration-based energy scavengers," *IEEE Pervasive Comput.*, vol. 4, no. 1, pp. 28–36, 2005.

[30] B. Jaffe, C. W., and J. H., *Piezoeletric ceramics*, vol. 3. 1971.

[31] P. D. Mitcheson, T. C. Green, E. M. Yeatman, and A. S. Holmes, "Architectures for vibration-driven micropower generators," *J. Microelectromechanical Syst.*, vol. 13, no. 3, pp. 429–440, 2004.

[32] S. Roundy, "On the effectiveness of vibration-based energy harvesting," *J. Intell. Mater. Syst. Struct.*, vol. 16, no. 10, pp. 809–823, 2005.

[33] E. E. Aktakka and K. Najafi, "A Micro Inertial Energy Harvesting Platform

With Self-Supplied Power Management Circuit for Autonomous Wireless Sensor Nodes," *IEEE J. Solid-State Circuits*, vol. 49, no. 9, pp. 2017–2029, 2014.

[34] S. Priya *et al.*, "A Review on Piezoelectric Energy Harvesting: Materials, Methods, and Circuits," *Energy Harvest. Syst.*, vol. 4, no. 1, pp. 3–39, 2017.

[35] K. Morimoto, I. Kanno, K. Wasa, and H. Kotera, "High-efficiency piezoelectric energy harvesters of c-axis-oriented epitaxial PZT films transferred onto stainless steel cantilevers," *Sensors Actuators, A Phys.*, vol. 163, no. 1, pp. 428–432, 2010.

[36] A. Hajati and S. G. Kim, "Ultra-wide bandwidth piezoelectric energy harvesting," *Appl. Phys. Lett.*, vol. 99, no. 8, pp. 2009–2012, 2011.

[37] H. Durou, G. A. Ardila-Rodriguez, A. Ramond, X. Dollat, C. Rossi, and D. Esteve, "Micromachined bulk PZT piezoelectric vibration harvester to improve effectiveness over low amplitude and low frequency frequency vibrations," *Proc. PowerMEMS*, pp. 27–30, 2010.

[38] R. Elfrink *et al.*, "Vacuum-packaged piezoelectric vibration energy harvesters: Damping contributions and autonomy for a wireless sensor system," *J. Micromechanics Microengineering*, vol. 20, no. 10, 2010.

[39] A. Lei *et al.*, "MEMS-based thick film PZT vibrational energy harvester," *Proc. IEEE Int. Conf. Micro Electro Mech. Syst.*, no. February, pp. 125–128, 2011.

[40] Y. C. Shu and I. C. Lien, "Analysis of power output for piezoelectric energy harvesting systems," *Smart Mater. Struct.*, vol. 15, no. 6, pp. 1499–1512, 2006.

[41] T. J. Kazmierski and S. Beeby, *Energy Harvesting Systems Principles,Modeling and Applications*. 2011.

[42] S. Chamanian, "DESIGN AND IMPLEMENTATION OF AN INTERFACE CIRCUIT FOR PIEZOELECTRIC ENERGY HARVESTERS," Middle East Technical University, 2018.

[43] H. A. Yigit *et al.*, "A Pulse-Width Modulated Cochlear Implant Interface Electronics with 513 μW Power Consumption," in *2019 IEEE/ACM International Symposium on Low Power Electronics and Design (ISLPED)*, 2019, pp. 1–5.

[44] S. Chamanian, H. Ulusan, Ö. Zorlu, A. Muhtaroğlu, and H. Külah, "An

Adaptable Interface Circuit for Low Power MEMS Piezoelectric Energy Harvesters with Multi- Stage Energy Extraction," *Biomed. Circuits Syst. (BIOCAS), IEEE*, pp. 4–7, 2017.

[45] B. Ciftci, S. Chamanian, H. Ulusan, and H. Kulah, "An Autonomous Interface Circuit Based on Self-Investing Synchronous Energy Extraction for Low Power Piezoelectric Energy Harvesters," in *18th International Conference on Micro and Nanotechnology for Power Generation and Energy Conversion Applications (PowerMEMS 2018)*, 2018.

[46] J. Dicken, P. D. Mitcheson, I. Stoianov, and E. M. Yeatman, "Power-Extraction Circuits for Piezoelectric Energy Harvesters in Miniature and Low-Power Applications," *IEEE Trans. Power Electron.*, vol. 27, no. 11, pp. 4514–4529, 2012.

[47] E. Lefeuvre, A. Badel, C. Richard, L. Petit, and D. Guyomar, "A comparison between several vibration-powered piezoelectric generators for standalone systems," *Sensors Actuators, A Phys.*, vol. 126, no. 2, pp. 405–416, 2006.

[48] Y. K. Ramadass and A. P. Chandrakasan, "An Efficient Piezoelectric Energy Harvesting Interface Circuit Using a Bias-Flip Rectifier and Shared Inductor," *IEEE J. Solid-State Circuits*, vol. 45, no. 1, pp. 189–204, 2010.

[49] T. T. Le, J. Han, A. Von Jouanne, K. Mayaram, and T. S. Fiez, "Piezoelectric micro-power generation interface circuits," *IEEE J. Solid-State Circuits*, vol. 41, no. 6, pp. 1411–1419, 2006.

[50] Y. Kushino and H. Koizumi, "Piezoelectric energy harvesting circuit using full-wave voltage doubler rectifier and switched inductor," *2014 IEEE Energy Convers. Congr. Expo.*, pp. 2310–2315, 2014.

[51] Y. H. Lam, W. H. Ki, and C. Y. Tsui, "Integrated Low-Loss CMOS Active Rectifier for Wireless Powered Devices," *IEEE Trans. Circuits Syst. II Express Briefs*, vol. 53, no. 12, pp. 1378–1382, 2006.

[52] T. Hehn *et al.*, "A Fully Autonomous Integrated Interface Circuit for Piezoelectric Harvesters," *IEEE J. Solid-State Circuits*, vol. 47, no. 9, pp. 2185–2198, 2012.

[53] S. J. Yun, S. S. Kwak, J. Lee, Y. C. Im, S.-G. Lee, and Y. S. Kim, "Asymmetric SECE Piezoelectric Energy Harvester Under Weak Excitation," *IEEE Access*, vol. 8, pp. 99132–99140, 2020.

[54] M. Dini, A. Romani, M. Filippi, and M. Tartagni, “A Nanopower Synchronous Charge Extractor IC for Low-Voltage Piezoelectric Energy Harvesting with Residual Charge Inversion,” *IEEE Trans. Power Electron.*, vol. 31, no. 2, pp. 1263–1274, 2016.

[55] S. Chamanian, H. Ulusan, A. Koyuncuoğlu, A. Muhtaroğlu, and H. Külah, “An Adaptable Interface Circuit with Multi-Stage Energy Extraction for Low Power Piezoelectric Energy Harvesting MEMS,” *IEEE Trans. Power Electron.*, vol. 34, no. 3, pp. 2739–2747, 2019.

[56] P. Gasnier *et al.*, “An autonomous piezoelectric energy harvesting IC based on a synchronous multi-shot technique,” *IEEE J. Solid-State Circuits*, vol. 49, no. 7, pp. 1561–1570, 2014.

[57] A. Morel *et al.*, “A Shock-Optimized SECE Integrated Circuit,” *IEEE J. Solid-State Circuits*, vol. 53, no. 12, pp. 3420–3433, 2018.

[58] J. Dicken, P. Mitcheson, I. Stoianov, and E. Yeatman, “Increased Power Output From Piezoelectric Energy Harvesters By Pre-Biasing,” *PowerMEMS*, pp. 75–78, 2009.

[59] D. Kwon and G. Rincón-Mora, “A Single-Inductor 0.35 µm CMOS Energy-Investing Piezoelectric Harvester,” *IEEE J. Solid-State Circuits*, vol. 49, no. 10, pp. 2277–2291, 2014.

[60] S. Chamanian, B. Ciftci, H. Ulusan, A. Muhtaroglu, and H. Kulah, “Power-Efficient Hybrid Energy Harvesting System for Harnessing Ambient Vibrations,” *IEEE Trans. Circuits Syst. I Regul. Pap.*, vol. 66, no. 7, pp. 2784–2793, 2019.

[61] D. A. Sanchez, J. Leicht, F. Hagedorn, E. Jodka, E. Fazel, and Y. Manoli, “A Parallel-SSHI Rectifier for Piezoelectric Energy Harvesting of Periodic and Shock Excitations,” *IEEE J. Solid-State Circuits*, vol. 51, no. 12, pp. 2867–2879, 2016.

[62] S. Du, Y. Jia, C. D. Do, and A. A. Seshia, “An Efficient SSHI Interface with Increased Input Range for Piezoelectric Energy Harvesting under Variable Conditions,” *IEEE J. Solid-State Circuits*, vol. 51, no. 11, pp. 2729–2742, 2016.

[63] S. Du, G. A. J. Amaratunga, and A. A. Seshia, “A Cold-Startup SSHI Rectifier for Piezoelectric Energy Harvesters with Increased Open-circuit Voltage,” *IEEE Trans. Power Electron.*, vol. 34, no. 1, pp. 263–274, 2019.

[64] S. Du, Y. Jia, C. Zhao, G. Amaratunga, and A. Seshia, “A Passive Design Scheme to Increase Rectified Power of Piezoelectric Energy Harvesters,” *IEEE Trans. Ind. Electron.*, vol. 46, no. c, 2018.

[65] S. Li, A. Roy, and B. H. Calhoun, “A Piezoelectric Energy-Harvesting System with Parallel-SSHI Rectifier and Integrated MPPT Achieving 417% Energy-Extraction Improvement and 97% Tracking Efficiency,” *2019 Symp. VLSI Circuits*, pp. 324–325, 2019.

[66] S. Du, Y. Jia, C. Zhao, G. A. J. Amaratunga, and A. A. Seshia, “A Fully Integrated Split-Electrode SSHC Rectifier for Piezoelectric Energy Harvesting,” *IEEE J. Solid-State Circuits*, vol. 54, no. 6, pp. 1733–1743, 2019.

[67] S. Du and A. A. Seshia, “An Inductorless Bias-Flip Rectifier for Piezoelectric Energy Harvesting,” *IEEE J. Solid-State Circuits*, vol. 52, no. 10, pp. 2746–2757, 2017.

[68] S. Du, Y. Jia, and A. A. Seshia, “An Efficient Inductorless Dynamically Configured Interface Circuit for Piezoelectric Vibration Energy Harvesting,” *IEEE Trans. Power Electron.*, vol. 32, no. 5, pp. 3595–3609, 2017.

[69] S. Du and A. A. Seshia, “A Fully Integrated Split-Electrode Synchronized-Switch-Harvesting-on-Capacitors (SE-SSHC) Rectifier for Piezoelectric Energy Harvesting with Between 358% and 821% Power-Extraction Enhancement,” *IEEE Int. Solid-State Circuits Conf.*, pp. 152–154, 2018.

[70] Z. Chen, M.-K. Law, P.-I. Mak, W.-H. Ki, and R. P. Martins, “A 1.7mm2 Inductorless Fully Integrated Flipping- Capacitor Rectifier (FCR) for Piezoelectric Energy Harvesting with 483% Power-Extraction Enhancement,” in *IEEE International Solid-State Circuits Conference*, 2017, pp. 372–374.

[71] Z. Chen, M.-K. Law, P.-I. Mak, W.-H. Ki, and R. P. Martins, “Fully Integrated Inductor-Less Flipping-Capacitor Rectifier for Piezoelectric Energy Harvesting,” *IEEE J. Solid-State Circuits*, pp. 1–13, 2017.

[72] D. A. Sanchez, J. Leicht, E. Jodka, E. Fazel, and Y. Manoli, “A 4μW-to-1mW Parallel-SSHI Rectifier for Piezoelectric Energy Harvesting of Periodic and Shock Excitations with Inductor Sharing, Cold Start-up and up to 681% Power Extraction Improvement,” *IEEE Int. Solid-State Circuits Conf.*, vol. 59, pp. 366–367, 2016.

[73] B. Ciftci *et al.*, “Low-Cost Fully Autonomous Piezoelectric Energy Harvesting

Interface Circuit with up to 6.14x Power Capacity Gain," in *2019 IEEE Custom Integrated Circuits Conference (CICC)*, 2019.

[74] S. Chamanian, A. Muhtaroglu, and H. Kulah, "A self-adapting synchronized-switch interface circuit for piezoelectric energy harvesters," *IEEE Trans. Power Electron.*, vol. 35, no. 1, pp. 901–912, 2020.

[75] S. Du, Y. Jia, C. Zhao, G. A. J. Amaratunga, and A. A. Seshia, "A Nail-Size Piezoelectric Energy Harvesting System Integrating a MEMS Transducer and a CMOS SSHI Circuit," *IEEE Sens. J.*, vol. 20, no. 1, pp. 277–285, 2020.

[76] B. Razavi, *Design of Analog CMOS Integrated Circuits*, 2nd ed. New York: McGraw-Hill Education, 2016.

[77] M. Seok, G. Kim, D. Blaauw, and D. Sylvester, "A portable 2-transistor picowatt temperature-compensated voltage reference operating at 0.5 v," *IEEE J. Solid-State Circuits*, vol. 47, no. 10, pp. 2534–2545, 2012.

[78] H. Uluşan, Ö. Zorlu, A. Muhtaroğlu, and H. Külah, "Highly Integrated 3 V Supply Electronics for Electromagnetic Energy Harvesters with Minimum 0.4 Vpeak Input," *IEEE Trans. Ind. Electron.*, vol. 64, no. 7, pp. 5460–5467, 2017.

[79] D. Kwon and G. A. Rincon-Mora, "A Single-Inductor 0.35 μm CMOS Energy-Investing Piezoelectric Harvester," *IEEE Int. Solid-State Circuits Conf.*, pp. 78–80, 2013.

[80] M. Shim and J. Kim, "Self-Powered 30 μW to 10 mW Piezoelectric Energy Harvesting System With 9 . 09 ms / V Maximum Power Point Tracking Time," *IEEE J. Solid-State Circuits*, vol. 50, no. 10, pp. 2367–2379, 2015.